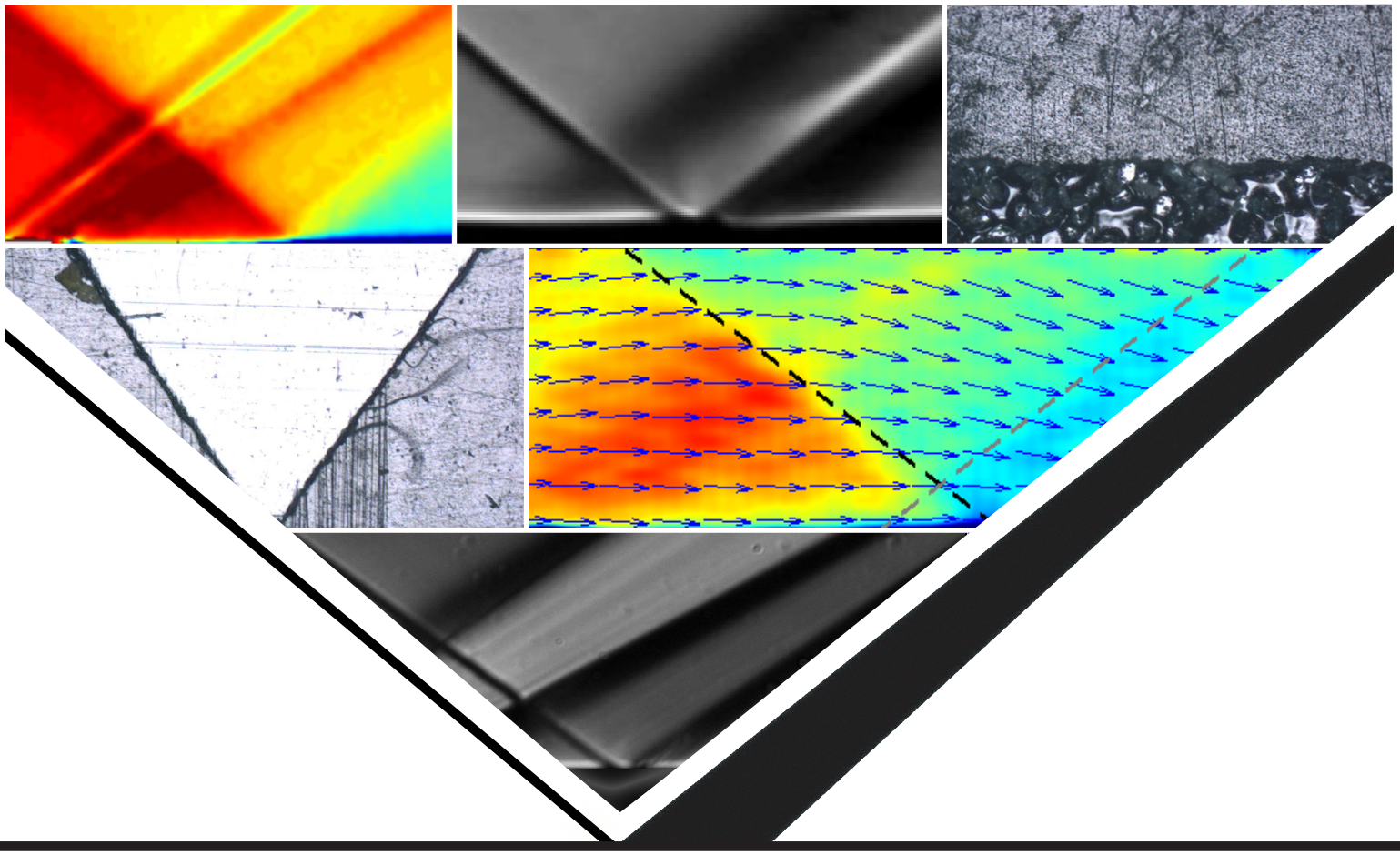

The effect of tripping devices on a shock wave - boundary layer interaction

Renee Louman

January 15, 2015

Aerodynamics

Faculty of Aerospace Engineering

TU Delft

Delft University of Technology

The effect of tripping devices on a shock wave - boundary layer interaction

Master of Science Thesis

For obtaining the degree of Master of Science in Aerospace Engineering
at Delft University of Technology

Renee Louman

January 15, 2015

Faculty of Aerospace Engineering · Delft University of Technology

Delft University of Technology

DELFT UNIVERSITY OF TECHNOLOGY
DEPARTMENT OF AERODYNAMICS

The undersigned hereby certify that they have read and recommend to the Faculty of Aerospace Engineering for acceptance the thesis entitled **"The effect of tripping devices on a shock wave - boundary layer interaction"** by **Renee Louman** in fulfillment of the requirements for the degree of **Master of Science**.

Dated: January 15, 2015

Supervisors:

Dr. ir. B.W. van Oudheusden

Dr. ir. F.F.J. Schrijer

R.H.M. Giepman, MSc

Dr. ir. G.E. Elsinga

Preface

After many months of hard work, I proudly present to you my thesis. There are many people that helped me during my thesis work, that all deserve a big 'thank you'. First of all, I would like to thank my supervisors Bas and Ferry for their guidance and valuable advice during my thesis work. Besides Bas and Ferry, I would like to thank Rogier, for always being willing to help (even at 7 p.m. on Fridays).
Furthermore I would like to thank for their technical assistance Henk-Jan, Nico, Eric and last but certainly not least Frits and Peter, who would help at the tunnel or with the set-up at any time. Also much appreciated were the lunches and conversations with all the basement-residents. Thank you for making graduating much more fun!

I would like to thank my parents for all their support during my studies, and for always being proud of me. Another thank you goes out to Lien and Rich and Chris and Denis, for helping me get through many, many winters. Finally, I would like to thank Jonathan, for still loving me and supporting me, even after I spend the last weeks mainly in a onesie behind my laptop, asking for loads of chocolate and crisps.

Summary

Shock Wave Boundary Layer Interactions (SWBLIs) occur frequently in supersonic and hypersonic flows and, depending on the strength of the shock wave and the state of the boundary layer, may lead to boundary layer separation. This can result in a multitude of problems, such as an increase in drag, a drop in air intake efficiency and high fatigue loads due to the inherent unsteadiness of the flow phenomenon. Since a turbulent boundary layer has a better capability to withstand the adverse pressure gradient that is inherent to the incident shock wave when compared to a laminar boundary layer, it is beneficial to have a turbulent boundary layer at the interaction. By forcing boundary layer transition only a short distance upstream of the interaction, the capability of the boundary layer to remain attached is increased while retaining the low skin friction coefficient of a laminar boundary layer for as long as possible.

In the current research, a SWBLI that consists out of an oblique shock wave impinging on a flat plate has been considered. The possibility to prevent separation, as a result of such a SWBLI, by forcing transition by tripping devices has been investigated experimentally. The main flow measurement technique was particle image velocimetry. Schlieren and oil flow visualisations supported the observations made during the PIV measurements and provided extra insight into the flow field.
The research was focussed on three boundary layer tripping devices: a 2D step, 3D distributed roughness and a zig zag strip. The experiments were conducted at Mach 1.7 and a unit Reynolds number of $35 \cdot 10^6$. The trips were placed 40 mm from the leading edge, which was approximately 30 mm upstream of the natural transition location. All three trips had a height of approximately k = 0.10 mm ($\approx 0.5 \cdot \delta$), corresponding to $Re_k = 3.6 \cdot 10^3$. The flow deflection angle was 3°, the shock impingement location of the main test case was 51 mm. Previous experiments showed that if there is no forced transition, these conditions will lead to a large separation bubble.

All three trips were effective in eliminating separation under these conditions. The zig zag strip required the shortest distance behind the trip before the boundary layer was fully turbulent. This trip also showed the lowest incompressible shape factor in the interaction region, the shortest interaction length and the fastest recovery of the boundary layer after the interaction. An additional case was investigated, in which the shock impingement location was shifted 5 mm upstream to $x_{sh} = 46$ mm, thereby bringing the shock impingement location closer to the trips. For this case, only the step and the distributed roughness were considered. It was found that under these conditions the step was no longer able to completely remove the separation bubble, whereas the distributed roughness case showed no signs of separation.

Table of Contents

Nomenclature

Latin Symbols

C_d	Drag coefficient
c_f	Skin friction coefficient
C_p	Pressure coefficient
d	Diameter
H	Shape factor
k	Roughness height
L	Interaction length
l_r	Recovery length
Ma	Mach number
p	Pressure
q	Dynamic pressure
r	Recovery factor
Re	Unit Reynolds number
Re_k	Roughness-based Reynolds number
Re_x	Local Reynolds number
T	Temperature
t	Time
U	Velocity
u, v	Cartesian velocity components
u_{eq}	Effective velocity
$v*$	Wall friction velocity
x, y	Cartesian coordinates
y^+	Dimensionless wall distance

Greek Symbols

α	Flow deflection angle
δ	Boundary layer thickness
δ^*	Displacement thickness

Δt	Separation time
γ	Specific heat ratio, $\gamma = 1.4$
θ	Momentum thickness
κ	Kármán constant, $\kappa \approx 0.41$
ν	Kinematic viscosity
ξ	Vorticity
ρ	Density
τ	Shear stress
τ_p	Particle relaxation time
χ_p	Particle relaxation length

Subscripts

∞	Far field
aw	Adiabatic wall
e	Local freestream
f	Of the flow
i	Incompressible
nd	Non-dimensional
p	Of the particle
sh	At the shock impingement location
th	Threshold
tr	At transition

Chapter 1

Introduction

Shock Wave Boundary Layer Interactions (SWBLIs) occur frequently in supersonic and hypersonic flows. Depending on the strength of the shock wave and the state of the boundary layer, the interaction may lead to boundary layer separation. This can cause a multitude of problems, such as an increase in drag, a loss of control surface effectiveness, a drop in air intake efficiency and it may even lead to an unstart of the engine and buffeting [2]. To illustrate the severity, the latter two consequences of a SWBLI are elaborated upon hereafter.

At the inlet of the engine a shock wave is formed that increases the pressure and decreases the Mach number of the flow (see Figure 1.1). If this shock wave interacts with a boundary layer that is not capable to withstand the pressure rise accompanying the shock wave, the boundary layer will separate upstream of the incident shock wave. This in turn will result in a highly unsteady system with a moving shock and a decrease in the mass flow rate. If the shock wave moves upstream and ultimately out of the engine inlet, the engine will even unstart [13] (Figure 1.2).

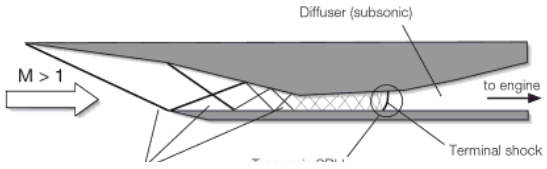

Figure 1.1: SWBLI in engine intake [4]

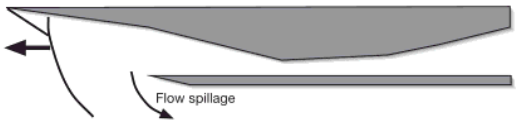

Figure 1.2: Unstart of the engine [4]

A second example of a potentially dangerous consequence of a SWBLI that leads to separation is shock buffeting on a transonic airfoil (see Figure 1.4). The increase in the boundary layer thickness and the separation bubble will force the shock wave to move upstream, thereby becoming increasingly weaker. At a certain upstream location the shock wave becomes too weak to lead to separation. The boundary layer will reattach again, after which the whole process is repeated again. This results not only in a less comfortable flight, but also in life cycle

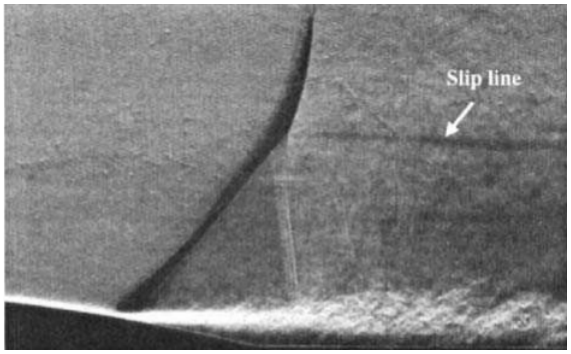

Figure 1.3: Schlieren visualisation of a transonic SWBLI [4]

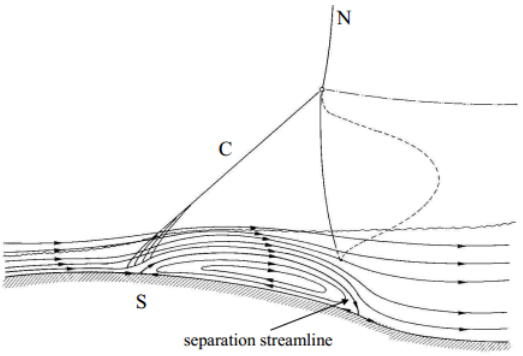

Figure 1.4: Graphical representation of a transonic SWBLI [10]

limitations as a consequence of structural fatigue [12]. In Figure 1.3 a Schlieren visualisation of a separated transonic SWBLI is presented, while in Figure 1.4 a graphical representation is shown.

It is obvious that in both of the previously discussed examples, the detrimental effects will be diminished if the boundary layer is capable to withstand the adverse pressure gradient that is inherent to the shock wave. It is therefore beneficial to have a turbulent boundary layer, which is considerably better in coping with adverse pressure gradients than a laminar boundary layer. The extent to which a turbulent boundary layer is beneficial can be illustrated by the increase in the pressure jump that a turbulent boundary layer can withstand without separating when compared to a laminar boundary layer. Under the conditions of this research project, a local Reynolds number of approximately $1.8 \cdot 10^6$, which corresponds to x = 51 mm, a turbulent boundary layer can withstand a shock that leads to a ratio of the pressure upstream to the pressure downstream of the shock system of 1.78. for a laminar boundary layer, this maximum ratio decreases to 1.11 (see Section 3.2 for a more elaborate discussion on the allowable pressure ratio).

Conflicting requirements concerning the boundary layer state

However, the capability of a boundary layer to withstand the adverse pressure gradient caused by a shock wave is only one out of many aspects of the flight that should be considered when designing a vehicle. For example, in the last decades it has become evident that the fuel consumption of transport in general should be reduced. One way to reach this goal is to reduce the drag and other losses, for example by ensuring that a boundary layer remains laminar. The reasoning behind this is that the friction drag of a laminar boundary layer is substantially lower than the friction drag of a turbulent boundary layer. For example, if a local Reynolds number of 10^5 is considered, the friction coefficient of turbulent boundary layer is almost twice the friction coefficient of a laminar boundary layer. This factor increases with increasing local Reynolds number: when the local Reynolds numbers is 10^7 this factor increases to almost 8 [37]. Unfortunately, the conflicting requirements stemming from these different aspects are not easily integrated. A compromise should be found between these two demands when designing a vehicle that travels at transonic speeds or faster.

TFAST
In 2012, a project on the transition location effect on a SWBLI has started as part of the seventh framework program of the European Commission. The main challenge of this project, named TFAST [18], is to investigate the effect of transition on the interaction and provide guidelines on how transition should be induced. By optimising the transition location and the means by which transition is forced, a contribution is made to the greening of the aircraft (by minimising losses which results in fuel savings) as well as to the safety (diminishing the unsteadiness of the interaction will lead to calmer conditions and less mechanical damage/fatigue).
TFAST has multiple research partners that vary from educational facilities, such as the University of Cambridge and the Technical University of Delft (TUD), to partners from the industry, such as Rolls Royce Germany and Dassault-Aviation. All these parters investigate, numerically and/or experimentally, one of the following research cases: the laminar transonic wing, the supersonic engine intake or the compressor/turbine blades. These cases will be investigated at a Mach number in the range of Ma=1.2-1.7.

The TUD contributes to the test case of the oblique shock interaction, which is related to the supersonic engine intake. The test conditions correspond to those of the environmentally friendly high speed business jet as investigated by the HISAC project (which was part of the sixth framework programme) as a reference case. This business jet is designed for a Mach number of Ma=1.6. This Mach number will be investigated by ONERA DAFE and IUSTI, while the TUD will investigate the slightly off-design condition of Ma=1.7.
To simplify the problem, the SWBLI in the engine intake is simulated by an incident shock wave on a flat plate. The benefit of the flat plate is that it does not create an additional pressure gradient, thereby limiting the number of variables. A second advantage is the increased optical access when performing experiments.

Research question
The purpose of this research is to determine how the two seemingly incompatible demands can be combined by using passive flow control devices. The accompanying research question is:

Which tripping device is the most effective in enhancing the ability of a boundary layer to withstand an adverse pressure gradient which derives from an incident shock wave in a Mach 1.7 flow?

The following set of sub-questions is used to quantify the effectiveness of the tripping devices:

- *Which trip can ensure that the boundary layer does not separate?*
  Preventing boundary layer separation is the main goal of placing the trip.
  SWBLIs have been observed to lead to unsteady flow phenomena, especially in the case of a separated boundary layer [13]. The separated flow and the associated increase in the unsteadiness are not only detrimental for the structural properties of the engine, such as fatigue, but will also lead to vortex shedding and losses in the efficiency of the

engine. These vortices will, in turn, lead to fluctuating loads on the compressor blades of the engine.

- *Which trip is the most effective in forcing transition?*
  In order to be able to place the trip as far downstream as possible, the distance downstream of the trip in which the boundary layer is not yet turbulent should be minimized.
- *Which trip results in the fullest velocity profile throughout the interaction?*
  The fuller the profile, the further the boundary layer is from separating. Therefore, a trip that leads to the lowest peak value of the incompressible shape factor is preferred,
- *Which trip results in a boundary layer that can recover the fastest after an interaction?*
  This is especially of importance if there is a possibility of a second SWBLI.
- *Which trip results in the shortest interaction length?*
  In multiple research projects, such as that of Souverein et al. [42], a function of the ratio of the interaction length over the incoming displacement thickness is used to determine how close a flow is to separation. The higher this ratio, the closer a flow is to separation. Since the unsteadiness of the system increases significantly after the flow separates or when the flow is close to separation, it is preferred to limit the interaction length as much as possible.

This research is carried out in the TST-27, a supersonic wind tunnel of the TU Delft. Three different trips will be investigated: a 2D step, 3D distributed roughness and a zig zag strip. To obtain quantitative information of the flow field, Particle Image Velocimetry (PIV) will be used. To obtain qualitative information in this same area, e.g. the position and curvature of the incident shock wave and the reflected shock wave, Schlieren visualisations will be used. Qualitative information concerning the flow topology on the surface of the flat plate, such as whether or not the boundary layer is separated, will be obtained by oil flow visualizations.

Report set-up

The following chapter provides some background chapter, as it elaborates on the physics of a SWBLI resulting from an incident shock wave. It is discussed what the differences in the flow field are between a separated and a non-separated boundary layer. A short description is given of one of the main theories that is used to predict the effect of an interaction on the boundary layer, the *free interaction theory*. Chapter 2 is concluded with a section on the effect of a trip on a SWBLI. This chapter is followed by the introduction of the current experiment in Chapter 3. In that chapter the model, the test conditions and the trips are discussed.
The subsequent chapter, Chapter 4, discusses the main flow measurement technique: PIV. This chapter presents a description of all the different stages in a PIV experiment, ranging from the set-up to the interpretation of the obtained velocity field.
Chapter 5 presents the results. The resulting integral boundary layer parameters as well as the drag and the interaction length of different trips is presented and compared to the case when no trip is used. Finally, in Chapter 6, the main conclusions are stated and recommendations for follow-up research are presented.

Chapter 2

Shock wave boundary layer interactions

In the supersonic freestream, information on the effect of a shock wave on the flow cannot propagate upstream. This is, however, no longer the case when the incident shock wave reaches the boundary layer. In the the boundary layer of a supersonic flow, the velocity will vary from 0 m/s at the surface to the supersonic freestream velocity at the top end of the boundary layer. As the inner layer is subsonic, information on the interaction can suddenly propagate upstream. As a consequence, the discontinuous jump in pressure will in this region be distributed over a finite area upstream as well as downstream of the incident shock wave. The increase in pressure will in turn slow down the flow, which will lead to a dilatation of the subsonic inner layer [25]. Depending on the shock strength and the state of the boundary layer, this can lead to two possible situations: the boundary layer will either remain attached or it will separate a finite distance upstream of the incident shock wave.

One of the parameters that is often used to describe the interaction is the *interaction length*. The interaction length is defined as the observed upstream shift of the reflected shock in comparison to the location of the reflected shock in an inviscid flow [42]. To further illustrate this definition, the interaction length is indicated in purple in Figure 2.1 and Figure 2.2. As the interaction length is a function of the height of the sonic channel, the interaction length is much larger when the boundary layer is laminar [11]. If the boundary layer is turbulent, the velocity profile will be much fuller and as a result the sonic channel will be more narrow. The beneficial effect of a turbulent boundary layer is also confirmed by the experiments of Schülein [41].

In the following sections, a distinction is made between an interaction that does not lead to separation, and an interaction that does lead to separation. Subsequently, the unsteady nature of the interaction is discussed. Also presented in this chapter is one of the main theories applicable to SWBLIs: the free interaction theory. Based on this theory, it can be predicted which combination of shock strength and boundary layer state leads to separation and which combinations do not. This chapter concludes with an overview of how a tripping device can possibly affect the interaction.

2.1 Attached boundary layer

If the shock wave is relatively weak, the boundary layer will be able to withstand the resulting pressure rise without separating. The sonic channel will still dilate, thereby leading to compression waves upstream of the incident shock wave. The incident shock wave will slightly curve upon entering the boundary layer as a result of the decreasing Mach number. An expansion fan will be present at the same location. This can be explained in two ways. First, as discussed by *Lees and Reeves* [30], no discontinuities can exist in the viscous boundary layer. As a result, the shock wave is reflected as an expansion fan and the flow is turned towards the wall again. Second, the boundary layer will start to recover downstream of the impinging shock wave. During the recovery the flow is turned away from itself, thereby creating an expansion fan. For a weak interaction, the dilatation will be small and thus the flow is only turned away from itself over a small angle. This will lead to a relatively weak expansion fan. The graphical representation of the flow field is shown in Figure 2.1.

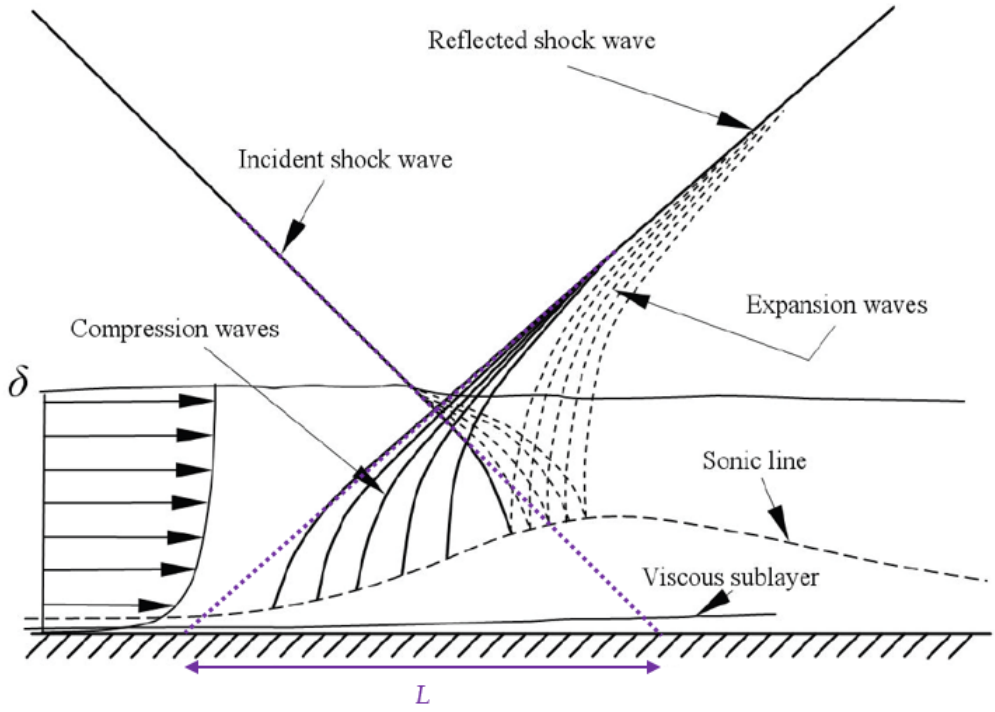

Figure 2.1: Flow field around an attached SWBLI, adapted from [28]

2.2 Separated boundary layer

If the shock is sufficiently strong, the boundary layer will no longer be able to withstand the pressure gradient and will separate. This will lead to a more complex flow field. There will be a separation bubble, leading to a significant thickening of the boundary layer. The streamline dividing the separation bubble and the outer part of the boundary later is termed the dividing streamline. The compression waves that are present in the region in which the thickening starts will soon coalesce into a shock wave. This shock wave is known as the separation shock, or the reflected shock. This shock will interfere with the incident shock wave at a certain distance from the wall. Due to this interaction the incident shock wave will bend towards the plate. As the flow travels over the separation bubble on the dividing streamline, the momentum of the flow on the streamline will increase due to the mixing. After a certain length, the momentum will be sufficient to overcome the pressure rise inherent to reattachment, and the boundary layer will reattach. As during the reattachment the flow is turned into itself again, the reattachment is accompanied by compression waves, coalescing to form the reattachment shock. Expansion waves will be present directly behind the incident shock wave, as discussed in the previous paragraph. The resulting flow field can be seen in Figure 2.2.

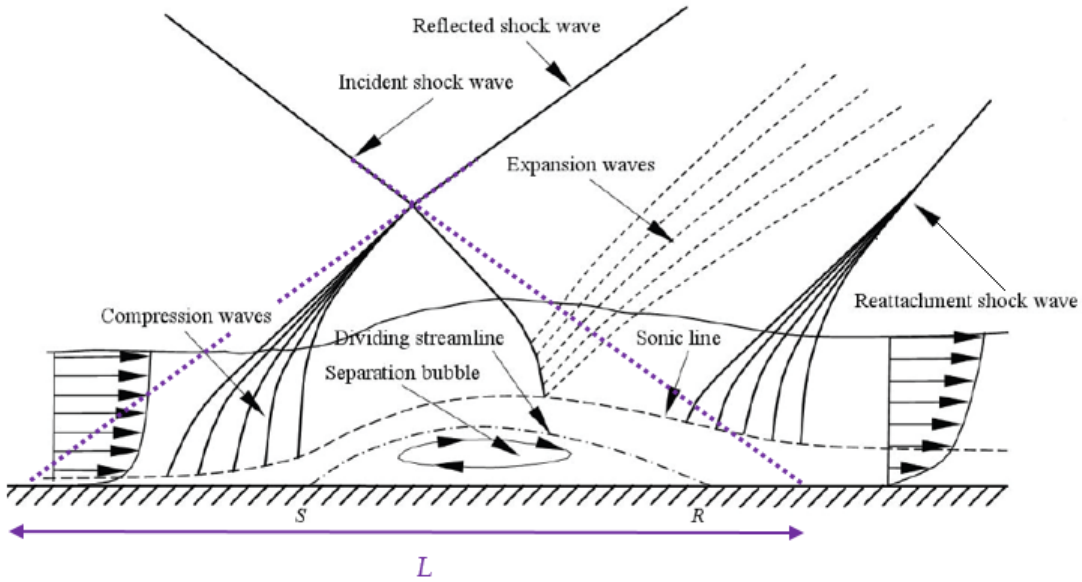

Figure 2.2: Flow field around a separated SWBLI, adapted from [28]

2.3 Unsteadiness

SWBLIs have been observed to lead to unsteady flow phenomena, especially in the case of a separated boundary layer [13]. The presence of a highly unsteady shock system in the engine is disadvantageous for several reasons. Besides losses in the efficiency of the engine, the moving shock system has a detrimental effect on the structural properties of the parts in the interaction region. The fluctuating loads in this region will lead to fatigue. Secondly, the moving shock system will shed vortices. This will lead to fluctuating loads on the compressor blades of the engine.

The unsteadiness of the interaction between a shock wave and a turbulent boundary layer has been studied in multiple research projects. An example is the research of Hou et al. [27], in which it was found that the global structure depends very much on the location of the separation shock foot. It was observed that when the separation shock is in its most upstream position, the scale of the separated flow, the velocity fluctuations and the domain of the perturbed flow are much larger. Similar results were obtained by Beresh et al. [5]. In their PIV experiment ensemble averaging was performed after the images were grouped on the basis of the shock location. From the experimental results it followed that positive velocity fluctuations in the incoming boundary layer, leading to a fuller velocity profile, are accompanied by a downstream moving shock and vice versa. It is stated that a possible explanation for this might be the enhanced capability of the boundary layer with the fuller profile to remain attached.
A similar analysis is performed by Oudheusden et al. [33] for the incipient separation of a natural turbulent boundary layer. Here it was found that there is a stronger link between the upstream boundary layer and the separation bubble than between the upstream boundary layer and the shock itself. It was also observed that the bubble frequency is between the upstream boundary layer frequency and the frequency of the separation shock. Based on the preceding observations, they concluded that the results could support the concept that the bubble dynamics act as a low-pass resonance filter that determines the dominant frequency of the overall interaction and the reflected shock in particular. This concept was earlier introduced by Dussauge [15].
A distinction between the three different boundary layer states (i.e. no separation, separation most of the time and incipient separation) when investigating what affects the unsteadiness was made by Souverein et al. [43]. Here it is claimed that when the boundary layer remains attached, the upstream effects govern the unsteadiness of the shock system and the frequency is relatively high. For a flow that is separated most of the time, downstream unsteadiness related to bubble pulsation is predominant. This unsteadiness has a significantly lower frequency. Finally, unsteadiness at incipient separation is a superposition of different mechanisms on different time scales. This results in spectra comparable to that of a separated flow. The extent to which they compare depends on the probability of instantaneous flow separation.

2.4 Free interaction theory

It has been attempted to predict the behaviour of the boundary layer when encountering a SWBLI. Examples are the research by Lees and Reeves [30] and Gadd [19]. In this thesis, the results of Chapman et al. [9] and Hakkinen [26] are presented. Although both of these papers were written over 40 years ago, these research are still applicable to the research of today.

In the experiments of Chapman et al. [9], it was observed that certain characteristics of separated flows do not depend on the downstream model geometry or the mode of separation. These interactions are termed free interactions. This paper argued that the pressure rise in the free interaction region can be determined with Equation 2.1.

$$\frac{p - p_0}{q_0} = \frac{2}{\sqrt{M_0^2 - 1}} \frac{d\delta^*}{dx} \tag{2.1}$$

in which,

p	pressure at the wall in the interaction region
p_0	pressure at the wall at the onset of the interaction
q_0	dynamic pressure at the onset of the interaction
M_0	Mach number at the onset of the interaction
δ^*	displacement thickness of the boundary layer
x	coordinate in streamwise direction

The observation that the flow parameters near separation depend only on the local conditions, given that the separated flow region is sufficiently long, was confirmed by the experimental results on a shock wave - laminar boundary layer of Hakkinen et al. [26]. In this paper, the pressure rise resulting from a separating boundary layer is divided into three parts. The first part is the pressure rise inherent to the separation. The pressure rise encountered up to the point of separation is termed Δp_s. Downstream of this initial rise, but upstream of the rise to the final pressure, the pressure is reasonably constant. This pressure rise is called the plateau pressure difference, Δp_{pl}. According to the free interaction theory, these pressure rises are not directly affected by the downstream model geometry or the mode of separation. Eventually, the pressure will rise to its final value after reattachment, p_f. Figure 2.3 gives a graphical representation of the pressure distribution. The theoretical relations that are found to determine the pressure coefficient associated with Δp_s and Δp_{pl} are shown in Equation 2.2 and Equation 2.3. The experimental results of Hakkinen et al. showed a maximum deviation from these relations of approximately 15%.

$$C_{p_s} = \sqrt{\frac{2c_{f0}}{\beta}} \tag{2.2}$$

$$C_{p_{pl}} = 1.65 C_{p_s} \tag{2.3}$$

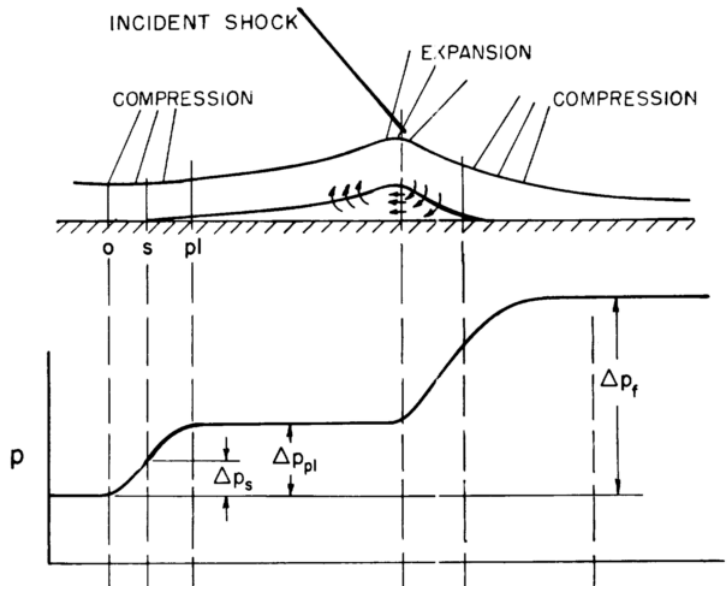

Figure 2.3: Pressure distribution for a separated boundary layer [26]

in which,

C_{p_s}	pressure coefficient at separation point
$C_{p_{pl}}$	pressure coefficient of the plateau
c_{f0}	skin friction coefficient at the onset of the interaction
β	$\sqrt{M_0^2 - 1}$

When there is incipient separation, the pressure will increase approximately linear until the final pressure is reached a small distance downstream of the incident shock. The simple relation $(C_p)_{incipient} = 2C_{p,s}$ approximates the pressure rise for incipient separation of a laminar boundary layer [26]. This relation can be used to obtain a first estimate of the maximum shock strength a laminar boundary layer can encounter without separating. A different equation should be used for turbulent boundary layers [4]. In this case, the following relation should be used:

$$\frac{p_2}{p_1} = 1 + 6\frac{\gamma}{2}M_1^2\sqrt{\frac{2c_{f0}}{\beta}} \tag{2.4}$$

which leads to the pressure coefficient presented in Equation 2.5.

$$(C_p)_{incipient} = 6\sqrt{\frac{2c_{f0}}{\beta}} \tag{2.5}$$

The friction coefficient at a set local Reynolds number will always be larger for a turbulent boundary layer than for a laminar boundary layer. This means that the pressure jump that

a turbulent boundary layer can withstand without separating is a at least three times the pressure jump that a laminar boundary layer can withstand.

2.5 The effect of forced transition on a SWBLI

Clearly, it is beneficial to have a turbulent boundary layer at the location of the interaction. A laminar boundary layer can be forced to transition into a turbulent boundary layer by placing a trip in the boundary layer. Since placing the trip far upstream of the interaction will lead to an increased friction drag, the trip should be placed close to the interaction. If placed at the correct location, the trip can prevent separation while not substantially adding to the friction drag.
Based on the information in the previous section, several parameters are identified that can be used to describe the interaction. These parameters can be used to investigate the effectiveness of the trips.

Shape factor
A first parameter to investigate is the boundary layer shape factor. As previously described, a boundary layer with a full velocity profile is more resistant against an adverse pressure gradient than when it displays an empty profile. The shape of the profile is characterized by the incompressible shape factor, H_i, and is defined as follows:

$$H_i = \delta_i^* / \theta_i \tag{2.6}$$

The incompressible displacement thickness δ_i^* and the incompressible momentum thickness θ_i are calculated as follows:

$$\theta_i = \int_0^\delta \frac{u}{U_e}\left(1 - \frac{u}{U_e}\right) dy \tag{2.7}$$

$$\delta_i^* = \int_0^\delta \left(1 - \frac{u}{U_e}\right) dy \tag{2.8}$$

The laminar Blasius profile has a shape factor of $H_i \approx 2.6$, while the shape factor of a fully turbulent profile is much lower, $H_i \approx 1.3$ [34].

The shape factor resulting from a specific trip can therefore be used as an indicator of the ability of a boundary layer to remain attached. A trip is deemed more effective if a lower shape factor is attained close to the trip. Besides in the region upstream of the incident shock wave, the development of the shape factor in the region downstream of the shock is interesting as well. This development is a good indicator of the recovery time of the

boundary layer. If there is a possibility of a second shock wave impinging on the surface close to the first shock wave, one would want to limit this recovery length as much as possible.

Interaction length
As discussed in the introduction of this chapter, the interaction length of a shock wave - turbulent boundary layer interaction will be shorter than that of a shock wave - laminar boundary layer interaction. In the introduction of this report it was discussed that a scaled version of the interaction length can be used as an indicator of how close a flow is to separation. For these reasons, a trip is deemed more effective if the interaction length is shorter.

Drag
When there is no shock, the trip will only result in an increase in the drag, while not having any favourable effects on the flow. f there is an incident shock, it would be possible to use the drag for the determination of how close a boundary layer has been to separation. When the flow separates, the skin friction at the location of the bubble will be negative. As a result, the total friction drag decreases when there is separation.

Chapter 3

Experimental set-up

As was mentioned in the introduction, this experiment is part of the TUD contribution to the TFAST project. The TUD has already started working on this project in 2012, and has finished the complete boundary layer study for the clean case. Their results can be found in the *24 month progress report* [23]. This experiment continues where the previous test-campaign left off: the same model and conditions will be used, but this time with the addition of trips. The goal of the experiment is to determine if this form of passive flow control, placed closely to the interaction, can prevent the boundary layer from separating as a result of a SWBLI. The design of the current experiment is based on two findings of this previous study. The first is the transition location. The transition location has been determined with infra red measurements, Schlieren measurements, oil flow measurements and PIV measurements. The results of the latter two measurements are presented in this chapter. The second finding is the flow deflection angle that leads to the separation of a laminar boundary layer while a turbulent boundary layer is able to remain attached.

In this chapter the experiment is described. In the first sections the test conditions and the model are presented. The last section is completely devoted to the trips. There are three trips that will be investigated: a 2D strip (which will be termed 'the step'), a distributed roughness strip and a zig zag strip. Based on the findings of the previous experiments and literature, the height and the location of the trips are selected. Additionally, the three trips are placed under a microscope to investigate their true dimensions.

3.1 The facility

The experiments are carried out in the TST-27. The TST-27 is a supersonic blow-down wind tunnel at the TU Delft. The maximum achievable Mach number is 4.2, and the maximum running time is on the order of several minutes. However, due to a gradual decrease in the total temperature, the maximum test time should be limited to 30 seconds. For a test time

shorter than 30 seconds, the variation in the total temperature will be within 5 K.

This test campaign is performed at a Mach number of $Ma = 1.7$, as is specified by the TFAST project. As these experiments continue where the previous test campaign of the TUD TFAST project left off, the other test conditions are similar as well. An overview of these freestream conditions can be found in Table 3.1 [22].

Table 3.1: Freestream conditions

parameter	symbol	value	unit
unit Reynolds number	Re	$34 \cdot 10^6$	[-]
total pressure	p_0	2.30	bar
static pressure	p_∞	0.47	bar
static temperature	T_∞	174	K
total temperature	T_0	275	K
density	ρ_∞	0.93	kg/m^3
turbulence level u	u'/U_∞	0.57	%
turbulence level v	v'/U_∞	0.43	%

3.2 The model

The SWBLI in the inlet of an engine is simulated with a flat plate and a shock wave generator. The advantage of using this configuration is that the flat plate, if placed aligned with the flow, does not induce a (significant) pressure gradient. This limits the number of variables that can have an influence on the flow field. The configuration is presented in Figure 3.1 (side-view) and Figure 3.2 (top-view). The flat plate is mounted such that it can be moved along the longitudinal axis of the wind-tunnel. This way, the location of the incident shock wave can be varied.

The flat plate

Ideally, the flat plate is placed under an angle of exactly 0° relative to the incoming flow, and remains in this position during a wind tunnel run. However, as a result of the precision with which the plate can be mounted in the test section and the resulting force on the model during a wind tunnel run, this situation is in practice very hard to achieve and maintain. If the flat plate is unintentionally placed under a negative angle of attack, an expansion fan will be created at the leading edge of the flat plate at the test-side. Due to the sharp leading edge of the flat plate, even a small negative angle can lead to separation of the laminar boundary layer, thereby creating a laminar separation bubble. When the boundary layer reattaches, it will have possibly transitioned into a turbulent boundary layer. To avoid this from happening, the flat plate will be placed at the small angle of 0.3° away from the shock generator. During a wind tunnel run, this angle will decrease to 0.1°-0.2°. As a result of this angle, the flow will

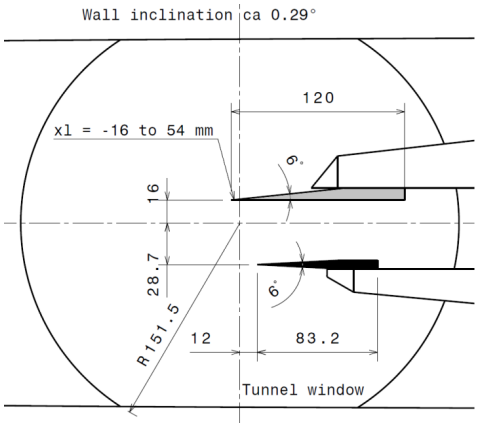

Figure 3.1: Flat plate and shock generator placed in the test section of the TST-27, side view. The grey area represents the flat plate, the black the shock generator

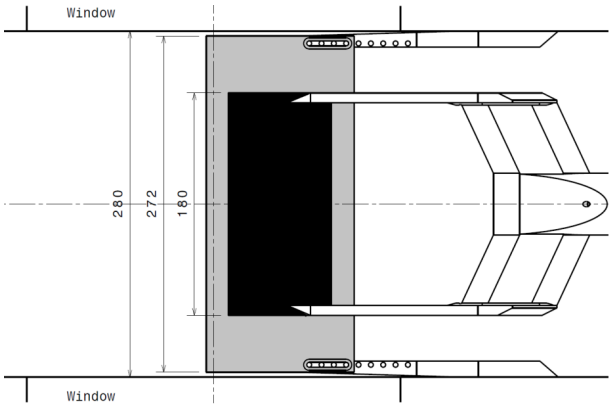

Figure 3.2: Flat plate and shock generator placed in the test section of the TST-27, top view. The configuration that is used to hold the shock generator is included as well.

be turned into itself. While this leads to the undesired presence of a weak leading-edge shock wave, this set-up will increase the probability that the boundary layer is still laminar at the location of the trip.

In the previous test campaign the natural transition location of the flat plate has been determined. The oil flow visualisation that was used to this purpose is presented in Figure 3.3. In this image, as well as in the remainder of this report, the x-coordinate is relative to the leading edge, i.e. at the leading edge x = 0 mm. The skin friction is higher for turbulent flows, and as a result less oil will remain on the flat plate when compared to the amount of oil that remains on the flat plate in a laminar region. Based on this difference, it could be concluded that the transition location is $x_{tr} \approx 70$ mm.

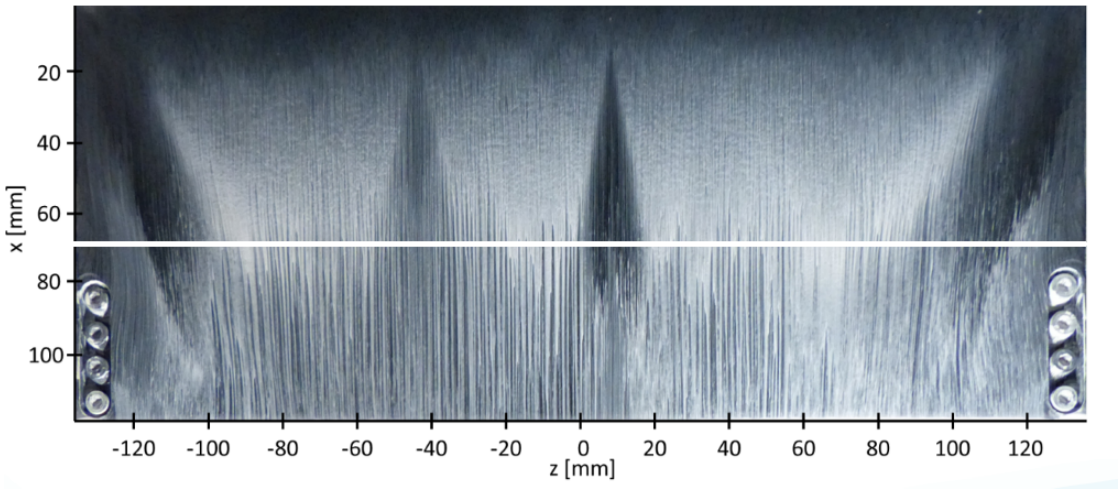

Figure 3.3: An oil flow measurement to determine the natural transition location. The white line indicates the approximate transition location. [22]

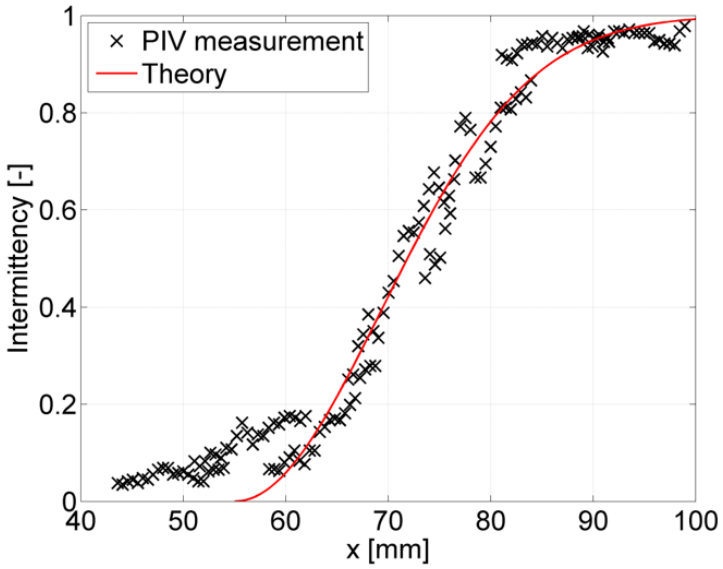

Figure 3.4: The intermittency of the boundary layer as a function of x-position [23]. The theoretical values are obtained from the research of *Dhawan and Narasimha* [37]

The transition location was subsequently verified from the images that were gathered for the PIV measurements. It was found that the near-wall seeding density in a laminar boundary layer is much lower than the seeding density in a turbulent boundary layer. This is most likely due to a combination of the strong curvature of boundary layer at the leading edge of the plate, the Magnus effect in the thin laminar boundary layer and the non-mixing nature of any laminar flow. A benefit of the difference between the seeding densities of the two states, is that the seeding density can be used to determine the local intermittency. The result is presented in Figure 3.4. It can be seen that the intermittency starts to rise at x $\approx$ 55 mm and reaches the value of 0.5 at x $\approx$ 72 mm. This is in good agreement with the result of the oil flow measurements.

The flat plate is made out of steel. The plate is polished to increase its smoothness, after which it is spray-painted black in order to decrease reflections of the laser light. The final surface texture of the flat plate has been examined with confocal laser scanning microscopy. This technique allows for a 3D reconstruction of the model surface. From this reconstruction individual profiles can be drawn to find the variation in height over a single line. It was found, based on 26 samples that each have a length of 920 μm, that the standard deviation of the flat plate surface height is approximately 7 μm.

The trips should be placed at a location upstream of the transition region, i.e. x = 55 mm. Also, it is desired to place the trips as far downstream as possible. The boundary layer thickness increases with increasing x-position, thereby facilitating the measurements in the boundary layer. Based on these considerations, it was decided to place the trips at x = 40 mm. At this location, the incompressible momentum thickness is θ_i = 0.030 mm and the incompressible displacement thickness is δ_i^* = 0.085 mm. The boundary layer thickness at this location is $\delta \approx$ 0.2 mm [23].

The shock generator

When determining the shock angle and the shock impingement location, two requirements were taken into account. The first requirement is that the trip is placed in close proximity of the SWBLI, in order to benefit as long as possible from the laminar state of the boundary layer. The second requirement is the possibility to obtain valid PIV measurements which do not suffer from laser reflections. These reflections are particularly severe in the first 5 mm downstream of the trips. Some additional distance should be accounted for, if the difference in the state of the incoming boundary layers needs to be determined. Based on these requirements, and the fact that a study of the clean case with $x_{sh} = 51$ mm has already been performed, it is decided to place the shock generator such that the incident shock wave again impinges at $x_{sh} = 51$ mm.

In the previous boundary layer study, flow deflection angles of $\alpha = 1 - 3 - 5°$ were tried for $x_{sh} = 51$ mm. For $x_{sh} = 71$ mm and $x_{sh} = 101$ mm only $\alpha = 3°$ was investigated. At the first location the flow is completely laminar, at the second transitional and at the third fully turbulent. It was found that the laminar flow is able to remain attached for a flow deflection angle of $\alpha = 1°$, but will separate if the flow deflection angle increases to $\alpha = 3°$ (this result is presented in Section 5.1). At x = 101 mm, the boundary layer did not separate for $\alpha = 3°$.

To further substantiate the result that a turbulent boundary layer for $\alpha = 3°$ at $x_{sh} = 51$ mm does not separate, a comparison with theory is made. To this purpose, the free interaction theory (Equation 2.5) is used. The Von Karman equation (Equation 3.1) is used for the estimation of the skin friction coefficient [39]. Based on these equations it is expected that in order to reach incipient separation of a turbulent boundary layer at $x_{sh} = 51$ mm, the pressure jump over the complete shock system should equal $p_3/p_1 = 1.78$.
To compare this pressure ratio to the pressure ratio for which a laminar boundary layer reaches incipient separation, again the free interaction theory is used. The skin friction coefficient of a laminar boundary layer is determined with the reference temperature concept for compressible flat plate flow, Equation 3.2 [48]. Based on this relation in combination with the free interaction theory and the assumption of an adiabatic wall, it is expected that incipient separation of a laminar boundary layer at x = 51 mm is reached if the pressure ratio equals $p_3/p_1 = 1.11$.

$$\frac{0.242}{\sqrt{c_f}}\left(1+\frac{\gamma-1}{2}Ma^2\right)^{-1/2} = \log(Re_x c_f) - \frac{1}{2}\log\left(1+\frac{\gamma-1}{2}Ma^2\right) \tag{3.1}$$

$$c_f \approx \frac{0.664}{\sqrt{Re_x}} \cdot \sqrt{\left(0.5 \cdot 0.039 Ma^2 + 0.5\frac{T_w}{T_e}\right)^{-1/3}} \tag{3.2}$$

For an inviscid interaction and $\alpha = 3°$, the shock relations have been used to determine that under the present conditions $p_3/p_1 = 1.35$. Therefore, it is assumed that also at x = 51 mm the turbulent boundary layer is able to remain attached. The laminar boundary layer, however, is expected to separate under these conditions. This makes $\alpha = 3°$ (corresponding to a shock angle of 38.9°) and $x_{sh} = 51$ mm suitable test conditions.

3.3 The trips

Three different trips are investigated: a step, distributed roughness and a zig zag strip. While the first is a 2D trip, the latter two are both 3D trips. An advantage of the 2D trip is that it is easier to simulate its flow field with CFD. In this section it is discussed why these trips are chosen and what they look like under a microscope. In the first paragraph, a previous experiment in which a wire was tested is discussed. This experiment led to the decision to investigate trips with a height of 0.10 mm. Subsequently, the trips that were used in the final experiment are presented.

Trip wire experiments and trip height selection

It was initially planned to use a wire as the 2D trip. The motivation for the wire was based on the large amount of research that has already been done on wires by the experimental community. Examples are the work of Dryden [14], Gibbings [20], Klebanoff and Tidstrom [29], Brinich [8] and more recently Reshotko and Tumin [36]. The research of both Gibbings and Brinich considers supersonic flow.
In the work of Gibbings, the roughness-based Reynolds number Re_k is used to determine whether a roughness element affects the transition location:

$$Re_k = \frac{U_\infty \cdot k}{\nu_\infty} \tag{3.3}$$

in which k is the roughness height, and U_∞ and ν_∞ are the velocity and the kinematic viscosity of the freestream. Under the conditions stated in Section 3.1, the minimum Re_k for which transition will occur in close proximity of the wire is then $Re_k > 2000$. This corresponds to $k > 0.06$ mm. Since this is only an estimate and wires of 0.05 and 0.10 mm are available, it was decided to first investigate the wire of 0.05 mm. If a wire of this diameter is already an effective trip, there is no need to investigate the wire of 0.10 mm. It was found that a wire of this diameter indeed promotes transition, but transition did not take place in near proximity of the trip. PIV measurements showed that if the wire is placed at 40 mm from the leading edge, the boundary layer will still be fully laminar 4 mm behind the trip. Based on additional oil flow measurements, it was estimated that transition would only take place 5-10 mm downstream of the trip.

The major disadvantage of the wire of 0.05 mm was the difficulty of attaching the wire to the model, and ensuring that the wire remained attached during a run. Different glues were tried, such as spray glue and super glue, but no glue was found that had sufficient adhesive strength while still maintaining the 2D character of the wire. A wire with a diameter of 0.10 mm was then tried. The increase in diameter indeed led to an increase in the number of runs during which the wire remained attached, but the number of runs was still not sufficient to complete a full boundary layer study. For this reason, not the wire but the step is used as a 2D trip.
Based on the substantial region behind the 0.05 mm diameter wire in which the boundary layer was still laminar, it was decided to continue with trips that have a height of 0.10 mm. This corresponds to $Re_k = 3555$.

The step

It was decided to use a step with a width in the streamwise direction of 2 mm, which corresponds to approximately 10δ at the trip location. The height of the step has been measured with a calliper, $k \approx 0.11$ mm.
Just as for the flat plate, the step has been placed under the confocal microscope. The resulting 2D image is presented in Figure 3.5 and the 3D image is presented in Figure 3.6. The previously determined height of the step has been used to calibrate the microscope. From the 3D image 26 profiles, each spanning 744 μm, are extracted. An example of a profile is presented in Figure 3.7. The dashed line indicates the average of the presented profile, while the dash-dot lines indicate the average standard deviation of all the profiles. The step has a smoothing effect on the surface: the standard deviation decreases from 7 μm to 5 μm.

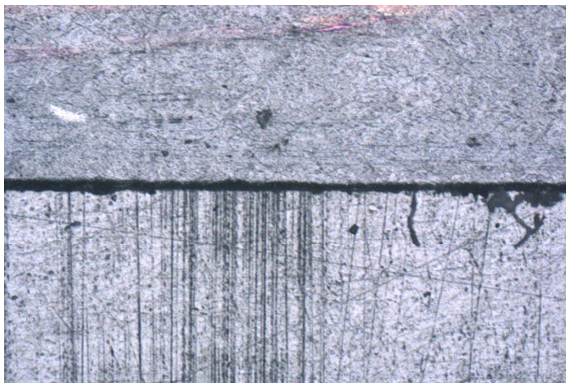

Figure 3.5: 2D microscopic image of the step (top is step)

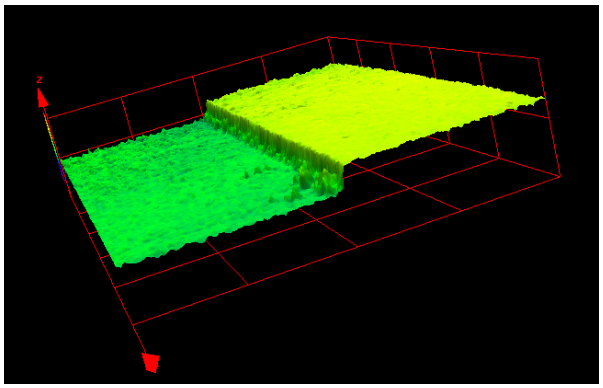

Figure 3.6: 3D microscopic image of the step

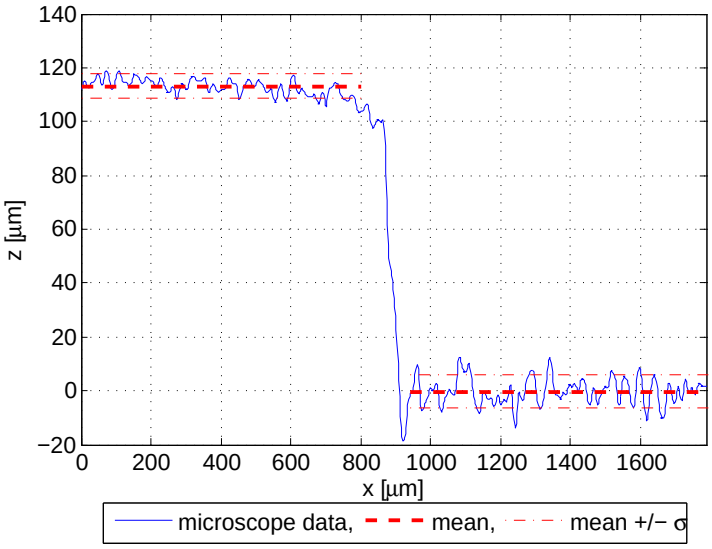

Figure 3.7: Profile of the step, spanning a section of the clean model and the trip

Distributed roughness

The effect of distributed roughness on the state of the boundary layer has been investigated extensively at supersonic speeds by *Braslow* [6, 7]. An advantage of the 3D trip over the 2D trip should be its increased efficiency [2] [48]. As a result, a lower roughness height can be used to promote transition. However, to limit the number of variables in this experiment, it was decided to investigate distributed roughness with the same roughness height (i.e. the grain size) of 0.10 mm and a the same width in the streamwise direction of 2 mm. The distributed roughness particles were made of Carborundum (SiC). To attach the distributed roughness particles to the flat plate, super glue was used.

The 2D microscopic image of the distributed roughness is presented in Figure 3.8. The separate grains can be easily distinguished, and the presence of the glue can be observed as well. In Figure 3.9 the 3D image of the distributed roughness can be seen.

Due to its different structure, the distributed roughness cannot be quantified with the simple technique that has been used for the step. One of the profiles of the distributed roughness can be seen in Figure 3.10. From this profile, it can be concluded that the roughness height is often much lower than the intended 100 μm. Three reasons are found that can explain this difference. The first is an incorrect scaling. The step could be scaled, since the height of this trip has already been determined. For the distributed roughness, however, this was not possible since it is unknown if a peak in Figure 3.10 corresponds to the top of a grain.
The second is the fact that the particles 'sink' into the liquid glue and will be partly covered by the glue. There will also be a reaction between the paint and the glue. This argument is supported by the presence of metal patches that appeared between the roughness particles,

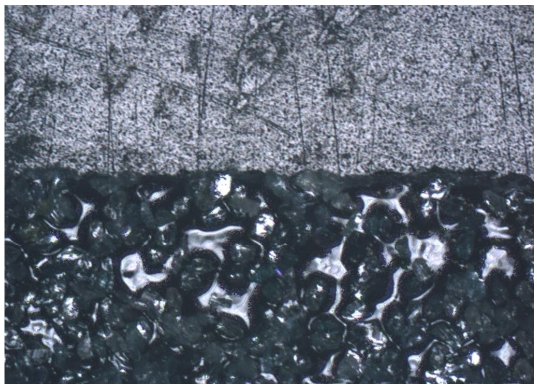

Figure 3.8: 2D microscopic image of the distributed roughness

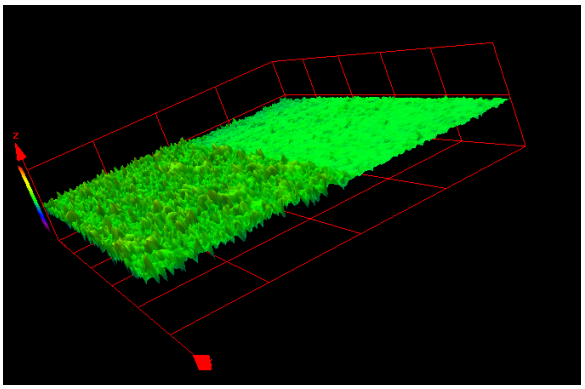

Figure 3.9: 3D microscopic image of the distributed roughness

where apparently no paint was present any longer. The occurrence of this reaction affects the profile: in the region of the trip, measurement points indicate heights lower than the clean part of the model. The minimum height of the profile is approximately -20 μm. Based on the determined scaling factors of both the step and the zig zag strip, which were of the order of 0.9, it is expected that the maximum height of the roughness elements will be at least 0.08 mm.
The final reason is that perhaps no grains were aligned such that their maximum height appears in the profile. In order to obtain an accurate estimate of the roughness density and height, a 3D image of a known scaling would be preferred.

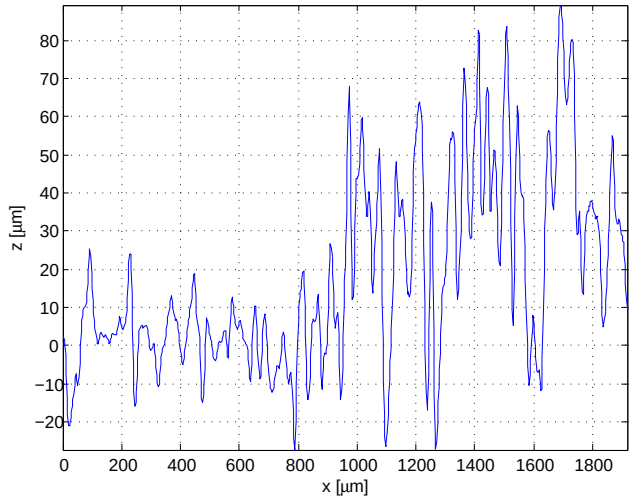

Figure 3.10: Profile of the distributed roughness trip, spanning a section of the clean model and the trip

The zig zag strip

The third trip that is investigated is the zig zag strip. The flow field behind a zig zag strip has been extensively studied at subsonic speeds by Elsinga and Westerweel [17]. An advantage of the zig zag strip should be that it significantly increases the mixing in the boundary layer, as a result of the vortices that are created. According to other research on the zig zag strip in subsonic flows, such as the research by Timmer and Van Rooij [46], the zig zag strip will not significantly add to the momentum thickness: it will lead to transition but it will hardly result in additional drag.

The height of the zig zag strip is $k \approx 0.11$ mm, the peak-to-peak pitch is 3 mm and the total width is 5.5 mm. The angle of the zig zag strip is 60°. The dimensions can also be seen in Figure 3.11.

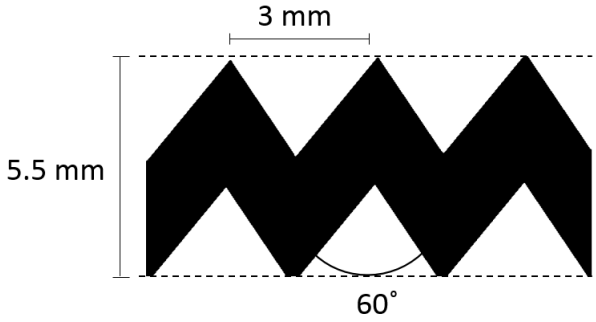

Figure 3.11: Dimensions of the zig zag strip

The 2D and 3D images of the zig zag strip are shown in Figure 3.12 and Figure 3.13. A profile of the 3D image is presented in Figure 3.14. The same quantification procedure as for the step is used to determine the height and the roughness of the trip. In this case 22 samples are used, of which per sample 902 μm was covered with the zig zag strip. Based on these samples, the roughness of the zig zag was determined to be 4 μm.

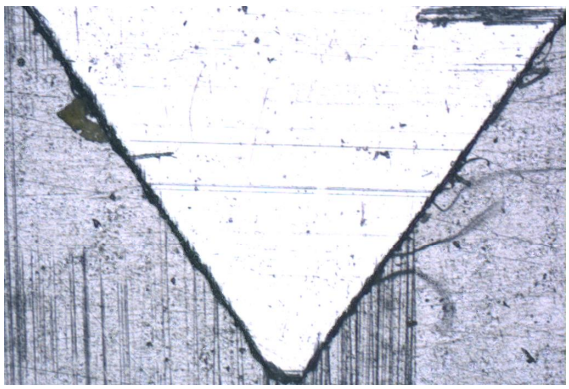

Figure 3.12: 2D microscopic image of the zig zag strip

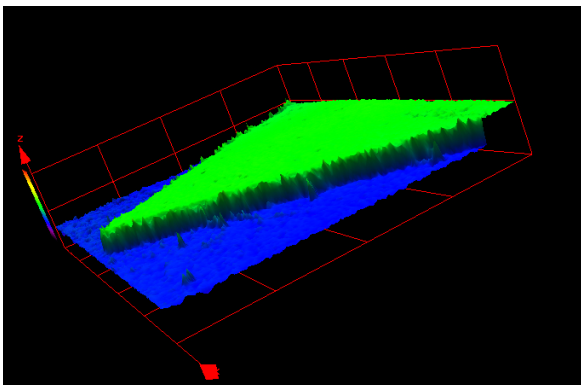

Figure 3.13: 3D microscopic image of the zig zag strip

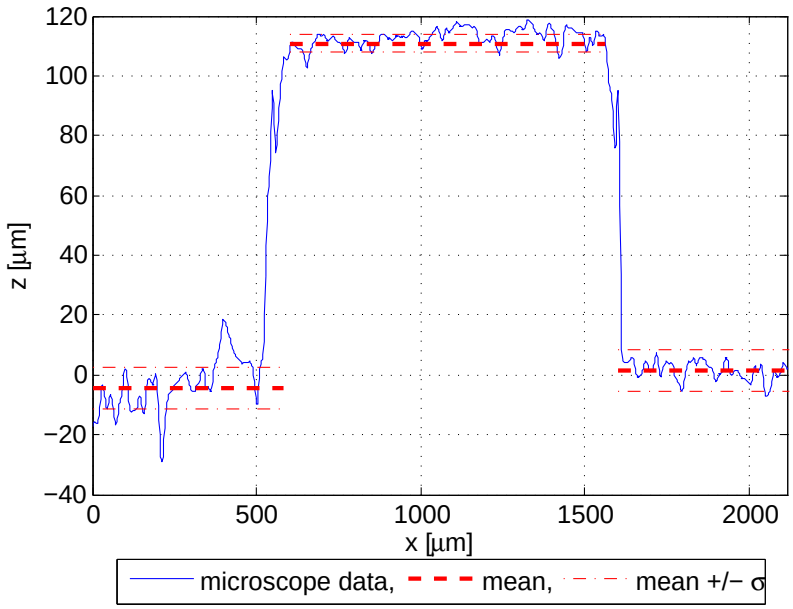

Figure 3.14: A profile of the zig zag strip (in spanwise direction), spanning a section of the clean model and the trip

3.4 Summary of the experiment

On the basis of oil flow measurements and PIV measurements of an earlier test campaign, it was determined that the boundary layer of the clean configuration will transition into a turbulent boundary layer at $x \approx 70$ mm. The transition onset will be at $x \approx 55$ mm. To ensure that the incoming boundary layer is laminar, while taking into account the advantage of a thicker boundary layer for PIV measurements, the trips will be placed at x = 40 mm.

The SWBLI should take place in the proximity of the trip. Taking into account the severe reflections in the 5 mm downstream of the trip, the shock impingement location is set at x = 51 mm.
In the previous test campaign it is found that a laminar boundary layer at x = 51 mm is able to remain attached for a flow deflection angle of 1°, but will separate if the angle is increased to 3°. At x = 101 mm, which is downstream of the natural transition location of the model, the boundary layer is able to remain attached for a flow deflection angle of 3°. Therefore, it is decided to use a shock generator that leads to this deflection angle, corresponding to a shock wave angle of 38.9°.

Three different steps are investigated: a 2D step, a zig zag strip and distributed roughness. While it was the intention to test all three trips at the same height, i.e. k = 0.10 mm, microscopic research showed that this is not the case. While the step and the zig zag strip both have a roughness height of $k \approx 0.11$ mm, the roughness height of the distributed roughness is lower. This is most likely a result of the reaction between the paint and the glue. The roughness height is now assumed to be of the order of 0.08 mm, but further research should be conducted to obtain a more accurate estimate.

Chapter 4

Particle image velocimetry

Particle Image Velocimetry (PIV) is a flow measurement technique that is used to measure the instantaneous velocity field in a 2D plane. It is an indirect flow measurement technique: not the velocity of the flow, but the velocity of tracer particles is measured. The velocity is based on the displacement of the tracer particles, over a short time span. By firing the laser twice, the time between the pulses equal to the separation time Δt, and capturing the light scattered by the particles, the displacement can be determined.
The obtained images are then divided into smaller windows, the interrogation windows. The displacement can now be determined by a Fast Fourier Transform (FTT) based correlation of the interrogation windows of the images that are taken at different moments.

Several PIV challenges are encountered during this research:

- *small scales*
  The boundary layer thickness varies between 0.2 mm for the laminar incoming boundary layer up to approximately 1 mm after the interaction. In order to resolve the flow in the thin boundary layer, a high spatial resolution is required.
- *high velocity gradients*
  Since the velocity in the boundary layer will increase from 0 m/s at the wall due to the no-slip condition to the freestream velocity of 450 m/s, the velocity gradient will be very large. This will lead to a broadening of the correlation peak.
- *non-uniform density*
  A gas will have a different refractive index at a different density. High density gradients are present in the boundary layer and around the shock wave, and can lead to optical aberrations and a blurring of the particles [16].

- *shock waves*
  The tracer particles do not have the same properties as air, and will need a certain time before they are adjusted to new conditions. Especially around shock waves and expansion fans, where there is a sudden increase or decrease in the velocity, the tracer particles will not be able to accurately follow the flow.

- *lack of light and seeding*
  There will be a lack of light resulting from the shadow of the trip and the deflection of the light due to the non-uniform density in the test section. The latter is termed the Schlieren effect. The lack of seeding is most severe in the laminar boundary layer upstream of the trip, and becomes much less pronounced after the boundary layer has transitioned into a turbulent boundary layer. The lack of seeding in the laminar boundary layer is most likely a result of a combination of the strong curvature of the flow at the beginning of the plate, the non-mixing nature of the laminar boundary layer and the Magnus effect.

In this chapter, a chronological overview of the different steps in the PIV process is presented. In the first section, the set-up of the instruments is presented. The set-up is designed such that the earlier discussed negative effects are minimised as much as is reasonably possible. Section 2 discusses the pre-processing that is done on the images. After the data is pre-processed, the displacement field is determined with a programme called Fluere. Exactly how this programme works, and which parameters affect the result, is presented in Section 3. Section 4 will discuss how the obtained displacement field can be improved by locating and replacing invalid vectors. In Section 5, it is stated how the parameters of interest can be determined based on the PIV results. In the final section it is tried to quantify the effect of processing parameters on the uncertainty of the results.

4.1 The set-up

In this section the configuration and the settings of the PIV-system are presented. A distinction is made between the settings that are used for the mapping of the boundary layer (small FOV), and the settings that are used for the overview measurements (large FOV). The settings of the cameras and the laser are summarized in Table 4.1. In the next section, the settings of the small FOV measurements (which are more challenging than the large FOV measurements) are elaborated upon.

The PIV experiment is performed with two Lavision Imager LX cameras of 2 MP (1624 $\times$ 1256 pixels) each, one on each side of the test section. The images are recorded at the cropped size of 1624 $\times$ 651 pixels, in order to increase the acquisition rate of the camera. The benefit of the increased frequency is the decreased test-time. The first camera is used to measure the velocity field downstream of the trip. The second camera is focused on the region upstream of the trip, and is used to determine if the incoming boundary layer is laminar.

The cameras are placed at an angle of 1° upwards from the horizontal plane and at an sidewards angle varying between 3° upstream and 6° downstream. The benefit of placing the camera under an angle, is that the blur resulting from the varying density in the test section will be less [16].
The spatial resolution of the cameras is set to 130 pix/mm at an f# of 16. It was found that a higher spatial resolution is not beneficial, since the increase in spatial resolution is accompanied by a decrease in the depth of focus. This will complicate the focussing of the camera on the light sheet, leading to more out-of-focus particles. The difficulty of focussing the camera at a higher spatial resolution can in part be overcome by increasing f # . A disadvantage of increasing f # is that the captured light intensity is less and that the particles become wider. Taking into account these disadvantages, 130 pix/mm was found to be the optimal spatial resolution.

The cameras have a minimum separation time of Δt = 430 ns. The minimum Δt is of importance since the shear in the boundary layer is substantial. A lower Δt decreases the range of displacements in one interrogation window; this is favourable since a large range of displacements leads to a broadening of the displacement peak.
Based on the minimum Δt and the spatial resolution, the shear in pix/pix in the laminar boundary layer is determined. At 40 mm from the leading edge, the boundary layer thickness will be approximately 0.2 mm. At a spatial resolution of 130 pix/mm, 0.2 mm will correspond to approximately 26 pixels. The displacement in the freestream will be $450/(130 \cdot 10^3 \cdot 430 \cdot 10^{-9}) \approx 25$ pixels. Taking into account that the main part of the laminar velocity profile is linear, the shear is calculated to be 0.96 pix/pix. While it is typically preferred to have a shear of less than 0.3 pix/pix, it is found that the shear of 0.96 pix/pix did not prevent the identification of the correlation peak with reasonable accuracy [21] [32].
To decrease Δt, the single frame - two images variant of PIV can be used. In this case both laser pulses are captured in one image. To determine the displacement field, auto-correlation is used: the correlation between an image and its duplicate. When auto-correlation is used, the minimum Δt will no longer be restricted by the camera. The shortened Δt will result in a decrease of the displacement gradient. The benefit of having a shorter Δt comes, however, at a price. The main disadvantage of this PIV-variant is inherent to the auto-correlation process: since the image is correlated with itself, multiple peaks will appear on the correlation map. These peaks will correspond to $\vec{U_{exp}} = 0$, $\vec{U_{exp}} = \vec{U}$ and $\vec{U_{exp}} = -\vec{U}$. This will make it harder to determine the velocity in regions in which the direction of the flow is not known beforehand, such as in separated flow regions. If the displacement is small, a second consequence can be that the three peaks blend into one single peak, thereby decreasing the accuracy with which the location of the true displacement peak can be determined. For this reason, it is decided to use cross-correlation.

The laser that is used to illuminate the particles is the double-pulse Nd:YAG Spectra Physics Quantra Ray PIV-400. The pulse duration is approximately 7 ns. This leads to a displacement of the flow of 0.4 μm, or 0.4 px, during one pulse. These displacements are low enough to not cause significant blurring of the particles. The power per pulse is 140 mJ.

Table 4.1: Settings of the PIV system

		small FOV	**large FOV**
camera	object focal length	105 mm	105 mm
	f #	16	16
	FOV	1624 pix × 651 pix	1624 pix × 880 pix
		12.5 mm × 5.0 mm	25.0 mm × 13.5 mm
	spatial resolution	130 pix/mm	65 pix/mm
laser	separation time	430 ns	800 ns
	pulse duration	7 ns	7 ns
	power per pulse	140 mJ	140 mJ

4.2 Seeding

With PIV it is possible to determine the displacement of the tracer particles, but it is not possible to directly determine the displacement of the flow. As a consequence, the accuracy of a measurement depends strongly on the ability of the seeding to follow the flow. Finding particles that can follow the flow becomes even harder when there are sudden velocity gradients, such as those induced by shock waves and to a lesser degree expansion fans. How fast the seeding can adjust to new conditions, is described by the equation of motion of small spherical particles [31]:

$$\frac{d\vec{U_p}}{dt} = \frac{3}{4} \cdot C_d \cdot Re_p \cdot \frac{\mu}{\rho_p d_p^2} \left(\vec{U_p} - \vec{U_f}\right) = -K \left(\vec{U_p} - \vec{U_f}\right) \tag{4.1}$$

in which the particle Reynolds number is defined as follows:

$$Re_p = \frac{d_p \left(\vec{U_p} - \vec{U_f}\right)}{\nu} \tag{4.2}$$

Based on Equation 4.1, one would conclude that the smaller particles follow the flow more accurately, an should thus be used in PIV experiments. There are, however, two other properties of the particles that should be taken into account. The first is the tendency of the seeding to form agglomerates. If seeding with a smaller grain size forms more or larger agglomerates than seeding with a larger grain size does, the actual particle size of the larger grains can be smaller. As a result, these initially larger particles will adjust faster to new conditions. [35]
The second is the light scattering behaviour of particles. When decreasing the particle size, the light scattered from the particles will decrease as well. A good balance should be found between the light scattering properties of a particle, and its ability to follow the flow.

For this experiment, it is decided to use TiO_2 particles with a grain size of 30 nm. The particles will be injected into the flow by a cyclone seeder. The possibility to use DEHS has also been investigated. This possibility is discarded since it was found that DEHS, which is injected into the flow by a different seeder, did not lead to seeding densities that were sufficient to accurately resolve the boundary layer.
The TiO_2 particles are dehydrated before an experiment, as was advised by *Ragni et al.*[35] in order to decrease the size of seeding agglomerates. To dehydrate the particles, the particles are placed in an oven that is set at $120°C$ for 40 minutes.

The oblique shock wave test

Two parameters that are often used to describe the accuracy with which the seeding particles track the flow, are the particle response time τ_p and the particle response length ξ_p. These two parameters, which are characteristics of the combination of the flow and the type of seeding, describe how fast (the first in time, the second in distance travelled) the seeding particles can adapt to the new conditions following a step input. The definition of these parameters is based on Equation 4.1. Assuming that K is constant, an analytical solution for the differential equation over an step input can be obtained:

$$ln\left(\frac{u_n - u_{n,2}}{u_{n,1} - u_{n,2}}\right) = ln(u_n^*) = -Kt = -\frac{t}{\tau_p} \tag{4.3}$$

in which u_n is the velocity component of the particle normal to the shock, and $u_{n,1}$ and $u_{n,2}$ are the velocity of the fluid before and after the step input. Integrating this equation again, leads to the distance travelled by the particles. Then using the fact that at $t = \tau_p$, $u_n^* = 1/e$, an explicit relation between τ_p and ξ_p is obtained:

$$x_n = u_{n,2} \cdot \tau_p \cdot ln\left(\frac{u_{n,1} - u_{n,2}}{u_n - u_{n,2}}\right) + \tau_p(u_{n,1} - u_n) \tag{4.4}$$

$$x_n(\tau_p) = \xi_p = \tau_p[u_{n,1} + (u_{n,1} - u_{n,2})e^{-1}] \tag{4.5}$$

An oblique shock wave test (OSW-test) is used to determine ξ_p. The idea is that the presence of a shock wave in the inviscid freestream will lead to a sudden deceleration of the flow, which is comparable to a step input. The OSW-test is set-up such that it complies with the requirements as presented by *Ragni et al* [35].
When processing the images of an OSW-test, the field of interest is rotated such that the oblique shock ends up as a normal shock. This way, the u component of the velocity determined by PIV will equal the velocity component normal to the shock. As the variation of u with y should be negligible while the variation of u with x in the region of the shock is significant, the window size will be stretched in the direction tangential to the shock. This

window shape will lead to the highest spatial resolution in the x-direction, while sufficient particles in the window are ensured by the relatively large height of the window.

The resulting velocity profile over a shock wave of the TiO_2 particles in the current experiment is presented in Figure 4.1. The same data is presented in a semi-log plot in Figure 4.2. The component of the velocity normal to the shock is represented by the non-dimensional variable u_n^*, of which the definition was presented in Equation 4.3. Using the fact that $u_n^*(\xi_p) = 1/e$, it can be determined from Figure 4.1 that $\xi_p = 0.74$ mm. Subsequently, the response time is calculated with Equation 4.5 to be $\tau_p = 2.12\ \mu s$. This value is in good agreement with the result of *Ragni et al.*, who found a particle response time of 2.20 μs for dehydrated TiO_2 with a particle size of 30 nm.

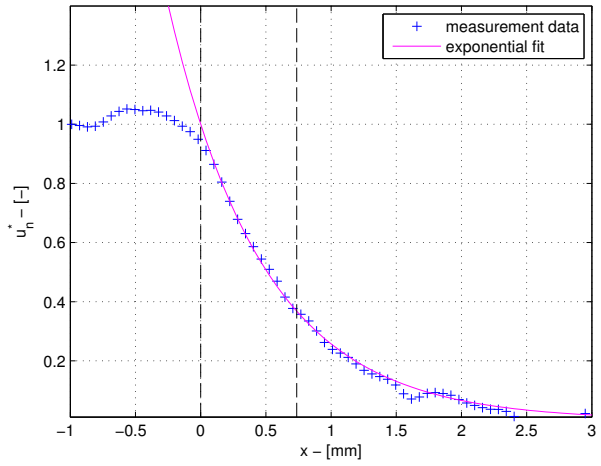

Figure 4.1: OSW-test

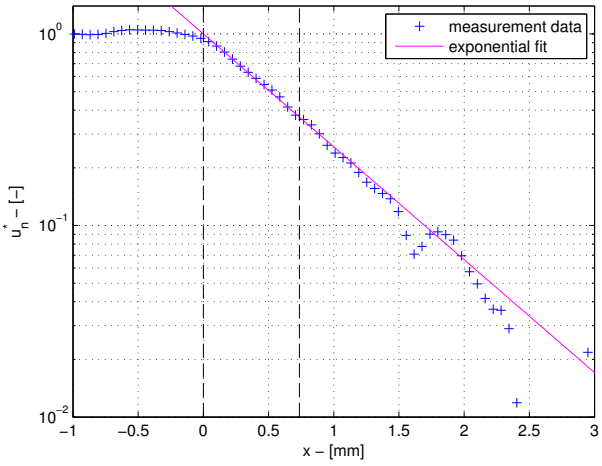

Figure 4.2: OSW-test on semi-log plot

4.3 Image pre-processing

Before the images are processed and the displacement field is obtained, several pre-processing steps need to be taken. To increase the accuracy, the read-out noise of the cameras is filtered out and a min-max filter is applied. To account for the movement of the model during an experiment and the small angle between the model and the camera, the images are rotated and shifted such that the wall is at the same location in all images. Finally, based on the average wall location of all images a mask is created.

Removing camera read-out noise

The cameras that are used for the PIV measurements add noise to the images. This read-out noise has a constant spatial frequency, and thus can be corrected for in all images in order to increase the signal-to-noise ratio (SNR). To determine how the cameras add to the noise, an image is taken when there is no laser light present. If there is no light, the resulting image (from now on called the dark image) will only contain noise. To compensate for the read-out noise, a Fourier transform is applied to the dark image to find the frequency of the noise. Subsequently, when a PIV image is transformed to the frequency domain, the peak value at the previously determined locations in the dark image is substituted by the average of its surrounding cells. At this stage, the PIV image can be transformed back into the spatial domain and the read-out noise will have been filtered out. The effect of this correction can be seen in Figure 4.3, in which an original image and an image corrected for the read-out noise are presented.

Applying a min-max filter

The PIV images can be further enhanced by applying a min-max filter [1]. The min-filter searches for the minimum light intensity in a predefined area (the filter size) around a pixel, which is subsequently subtracted from the original image. This will decrease the background noise, by setting the background light intensity to zero. Since the filter is applied locally, variations in the background can be accounted for. The filter size must comply with two conditions: it must be larger than the characteristic particle size and it must be small compared to the image size. The reasoning behind the first requirements is that if one particle is larger than the filter size, no good representation of the background light intensity will be obtained. The reasoning behind the second requirement is that one wants to correct the image based on the local noise, which cannot be determined if the filter size is in the order of the image size.
The second step is applying the max-filter. This filter works in the same fashion as the min-filter, but finds the maximum light intensity. Based on this information, the image can then be normalised by the resulting max-field. The advantage of applying the max-filter, is that all particle pairs will contribute equally to the correlation. If the image is not normalised, the contribution of one exceptionally bright particle would outweigh the contribution of multiple

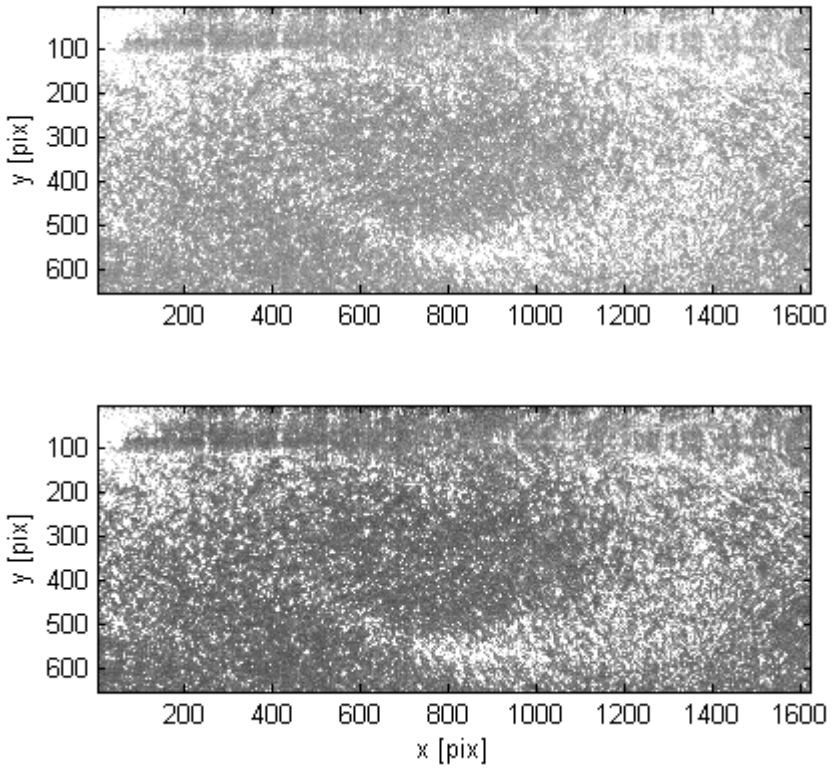

Figure 4.3: The original PIV image and the PIV image that is corrected for the camera read-out noise

less bright particles.

Rotating images and identifying the wall

The images should be corrected for the angle of the plate relative to the horizontal. This angle is a result of the positioning of the camera and the positioning of the model. To determine this angle, the wall location in multiple images is identified on the basis of the reflection of seeding particles. For this purpose, a MATLAB program is used. This program requires two inputs. The first input is the range of the possible wall locations, the second is the band around the possible wall location in which the program will look for reflections. The image is then split into smaller images that have a width of 200 pixels. In these smaller images, the local wall location is then determined by correlating the window above every possible wall location to the window below every possible wall location. The width of these windows equals the width of the smaller images, i.e. 200 pixels, while the height of these windows equals the previously specified band in which the program looks for reflections. The wall location that leads to the highest correlation is then set as the local wall location. By applying a linear fit through the local wall locations, the angle of the plate can then determined. This routine is repeated for at least 50 images, after which the average is used to correct all images.

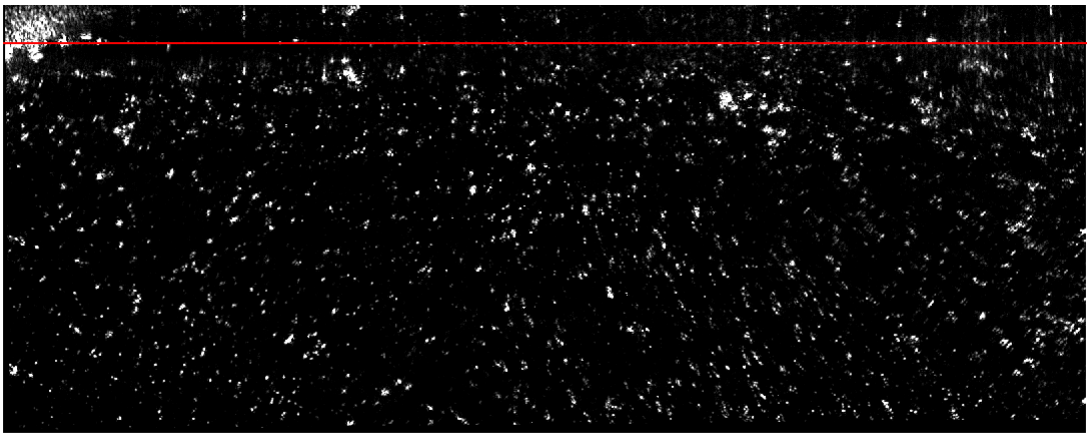

Figure 4.4: Identified wall location in an already rotated PIV image

A second parameter to adjust for is the relative location of the wall in the images. For this research, ensemble averaging will be used (this averaging technique is further elaborated on the next section). This averaging technique will combine the correlation maps of numerous images to determine the average flow field. In these experiments, the number of images that is used to determine the average flow field ranges from 200 up to 500. During the run, the model will move up and down as a result of the flow. It goes without saying that if an averaging technique is used, it is of the utmost importance that the average is taken over numerous correlation maps that represent the exact same location. Therefore, the small fluctuations in the position of the model should be accounted for. The technique that is used to determine the rotation of the model, can again be used to this end. The main difference is that there is no need to split the image into multiple windows, since the rotation correction has already been applied. The wall location is determined for all images separately, after which they are all shifted to ensure that the wall is at the same location in all images.
The result of these two steps, i.e. rotating and shifting the image on the basis of the identified wall location, is presented in Figure 4.4. A large reflection with a high intensity is present in the upper left corner. This reflection is a result of the trip, of which the trailing edge is located approximately 2 mm from this field of view. Since the reflection prevents from finding the wall, this area is not taken into account when determining the rotation or the location of the wall. The red line indicates the expected wall location. Several reflections at different x-positions can be identified. Based on the fact that the expected wall location is at all x-locations halfway between the actual particle and the reflection of the particle, it is decided that the original image is rotated over the correct angle.

Creating a mask

The last pre-processing step is creating a mask. This mask is used when the images are processed in Fluere, to indicate in which regions no useful data can be present. Creating this mask is relatively easy. All the images have already been shifted, and thus the wall location should be constant. Based on this information, a matrix with the same dimension as the

digital image is constructed which contains only ones and zeros: a one indicating that the data should be blanked and should not be used for the correlation, a zero indicating that the data should be used for the correlation.

4.4 Image processing

After all the images are preprocessed, the program Fluere [38] is used to determine the displacement field by performing a Fast Fourier Transform (FFT) based cross-correlation of image A and B. Fluere is a home-built program; its algorithm is based on the deformation of the interrogation windows with an iterative multi-grid approach. To increase the stability and the spatial resolution, a Gaussian window weighting function is applied [3]. At every pass the displacement is determined. The results of one pass can then be used to shift and deform the interrogation window of image B. As a result, the standard $1/4^{th}$ rule does not apply any longer to the window size of any pass but the first.

The mask that has been made during the pre-processing is used to tell Fluere where the wall is located [21]. Every interrogation window corresponds to a an equally sized part of the mask, which consists out of ones and zeros. The ones indicate that the wall is located at that specific position and the data at that position should thus not be taken into account; the zeros indicate that the data should be considered. Also in these windows a Gaussian window weighting function is applied, which is partly based on the mask. Subsequently, the displacement vector is relocated according to the weighting function. While the vector is normally located at the center of the interrogation window, the vector locations close to the wall are now relocated to the positions defined by the found first moments.

A second feature of Fluere that can be used near the wall, is the vector-limiter function. This function is especially useful when the images suffer from severe reflections in the wall region. The reflections will result in a peak in the correlation map at $\vec{U} = 0$. By enabling the vector limiter, and setting the lower limit of the u-component of the velocity at a value higher than zero, this peak will be discarded. It goes without saying that the vector limiter function should only be used in this fashion if it is certain that the flow will not be separated.

Effect of the window size

The velocity vector of an interrogation window represents the average of the velocities present in the interrogation window. Especially in areas with a high velocity gradient, this will lead to a broadening of the displacement peak, thereby affecting the accuracy with which the displacement can be determined. There are two regions in which the velocity gradient is substantially higher than the remaining part of the flow: the boundary layer and the region around the shock waves. In the boundary layer the highest gradients in the direction normal to the plate can be found, while in the region around the shock waves the highest gradients in the streamwise direction can be found.
A second aspect that should be taken into account is the scale of the flow features that is being

investigated. If the window size is significantly larger than the scale of these flow features, the flow features will be filtered out and will not appear in the final solution.
While for these two reasons it seems tempting to use very small interrogation windows, this is not necessarily true. The decreased effect of the displacement gradient on the accuracy of the results and the increase in the range of scales that can be resolved, comes at a price. Since the seeding density is quite low, the amount of seeding that is present in a small interrogation window might not be sufficient to accurately determine the location of the displacement peak. This will lead to relatively many spurious vectors. Therefore, a balance between the accuracy of the vectors and the effect of averaging is needed.

To quantify how the window size affects the results a test in which a shock wave was present has been processed at three window heights and three window widths. Six passes were used and the overlap in both x- and y-direction was set to 75%. The window sizes corresponding to the pass number can be found in Table 4.2. Also indicated in this table are the search radii of every pass. The search radius of the first step is relatively large, as the window shift is not yet applied and it is crucial to 'capture' the displacement. A search radius of 32 pixels should be sufficient, since for a flow of 450 m/s, a resolution of 130 pix/mm and a separation time of 430 ns the displacement between the two instances is just under 25 pixels.

Table 4.2: Window size and search radius of every pass

		Pass number					
		1	2	3	4	5	6
window height	[pix]	128	64	32	16	8	8
		128	64	32	32	12	12
		128	64	32	32	16	16
window width	[pix]	256	256	128	128	64	64
		256	256	256	128	128	128
		256	256	256	256	256	256
search radius	[pix]	32	16	16	16	16	8

One of the parameters that can be used to investigate the effect of the window size is the shape factor. The shape factor reaches its maximum value in the interaction region. Downstream of the interaction region, the shape factor shows a quick recovery. This variation over a small streamwise distance makes the shape factor a suitable parameter for the investigation of the effect of the window size on the solution. Besides the fact that the incompressible shape factor is a suitable parameter for this purpose, determining the variation in this parameter (both upstream as well as downstream of the interaction) is one of the main goals of this research. Therefore, it is deemed important to know how significantly the shape factor is affected by the selection of the window size.
The variation in the shape factor using various window sizes is presented in Figure 4.5. The two distinct features earlier mentioned can be clearly identified: with increasing window size, both the noise and the maximum value of the shape factor decrease. It seems that a good balance between the averaging effect and the noise is found for a window size of 128 $\times$ 12 pixels. This window size will therefore be used for the processing of all the runs.

At this point, it can be quantified what the effect of the window size is. Since the highest gradients are present in the interaction region, the effect of the window size should be most prominent when one looks at the peak value of the shape factor. When comparing the results obtained with a window size of 128 x 12 pixels to the results of the other eight test cases, the maximum deviation from the peak value of the shape factor is 4%.

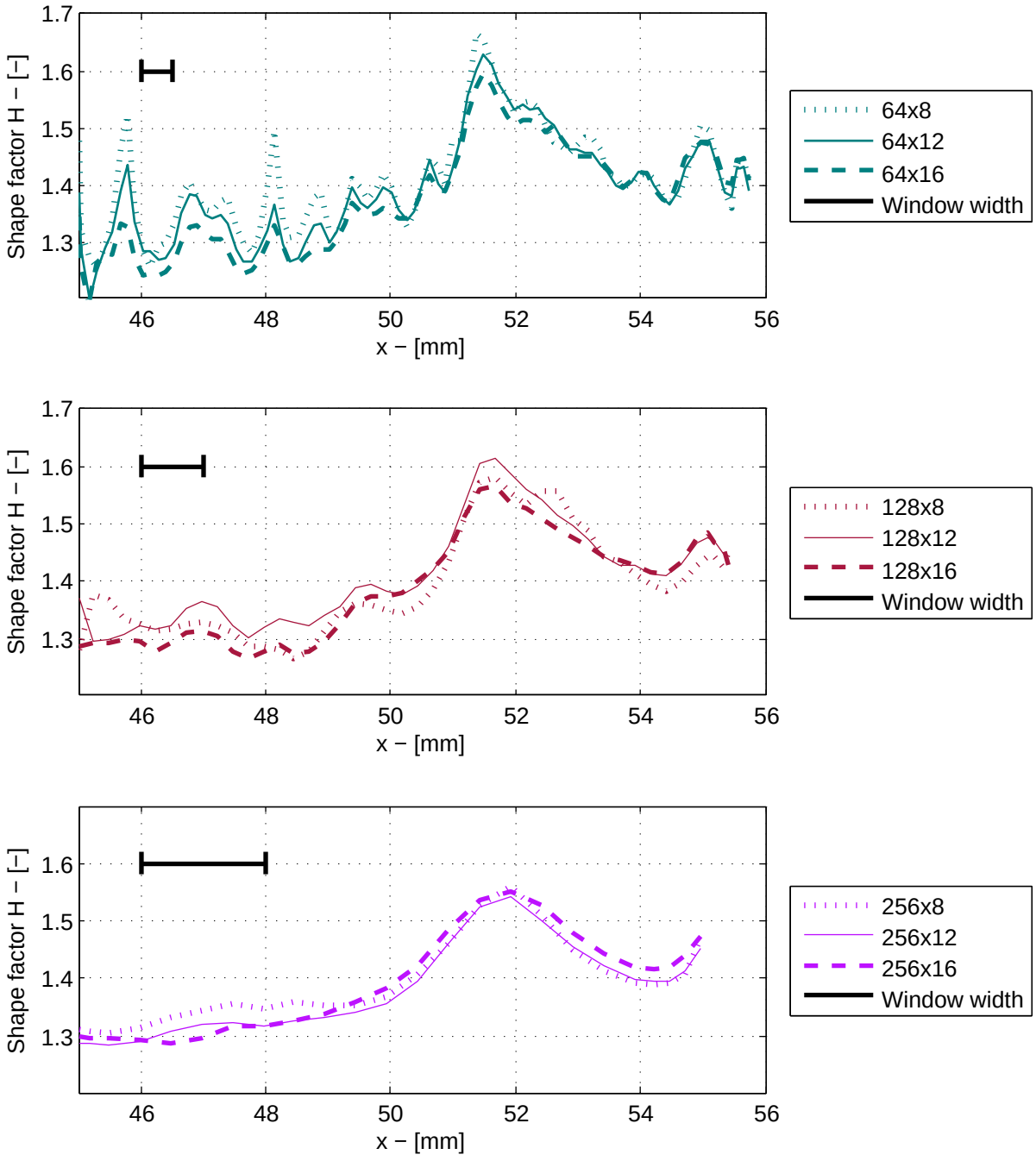

Figure 4.5: Effect of window size on the variation of the shape factor with x-location, $x_{sh} = 51$ mm

Ensemble averaging vs single image correlation

In the boundary layer the seeding density is relatively low. When using only one image pair to determine the displacement field, there will be many interrogation windows that do not contain (a sufficient number of) particle pairs. This will result in inaccurate displacement vectors. This problem can be solved by ensemble averaging. With this technique, the correlation planes of all interrogation windows are determined. Subsequently, all these correlation planes are summed in order to find the average correlation plane. If the flow is steady, the displacement peak should appear at the same location in all images and the averaging should thus not affect the height of the peak much. In contrast to the displacement, the noise that is still present in the correlation plane after the pre-processing is mostly random. As a consequence the noise and the erroneous displacement peaks are averaged out, which results in an increase of the signal-to-noise ratio.

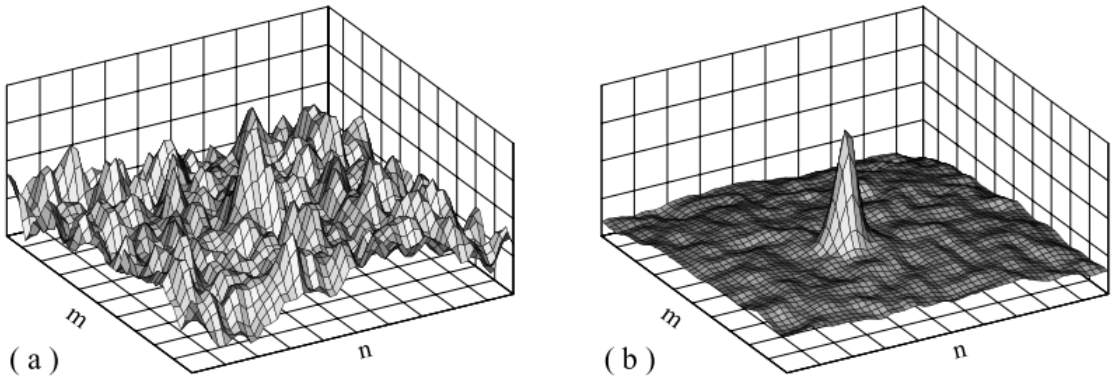

Figure 4.6: The correlation planes that are obtained with (a) conventional correlation of one image pair and (b) ensemble correlation of 101 image pairs [47]

The effect of ensemble averaging can be illustrated further by the velocity fields that are obtained when the number of images used for correlation is varied. The velocity field corresponding to a cross correlation of one image pair is presented in Figure 4.7. Clearly, the velocity field is severely affected by the noise. It is even impossible to identify the location of the reflected shock wave with a reasonable accuracy. When an ensemble size of 10 images is used for the cross-correlation, there is much less noise in the image (Figure 4.8). The accuracy with which the location of the incident shock wave as well as the reflected shock wave can be identified has significantly increased. This accuracy increases even further when 100 images are processed, see Figure 4.9. Most of the noise is gone and the flow in the three regions (i.e. in front of the incident shock wave, between the incident and reflected shock and after the reflected shock) is becoming more uniform.

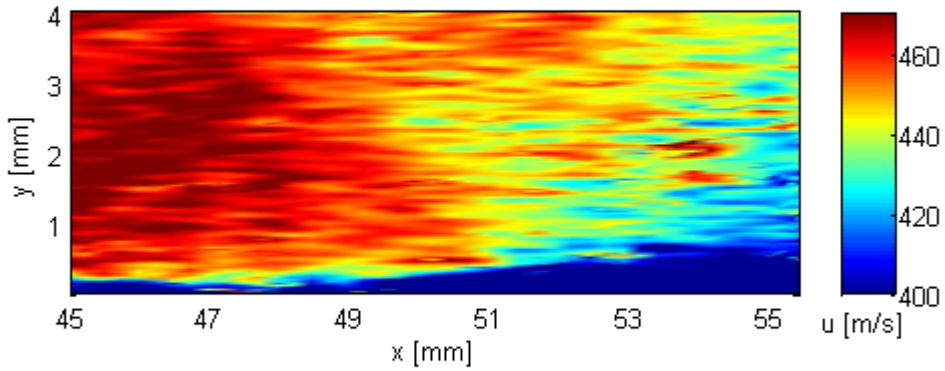

Figure 4.7: Velocity field around a shock. Correlation based on 1 image

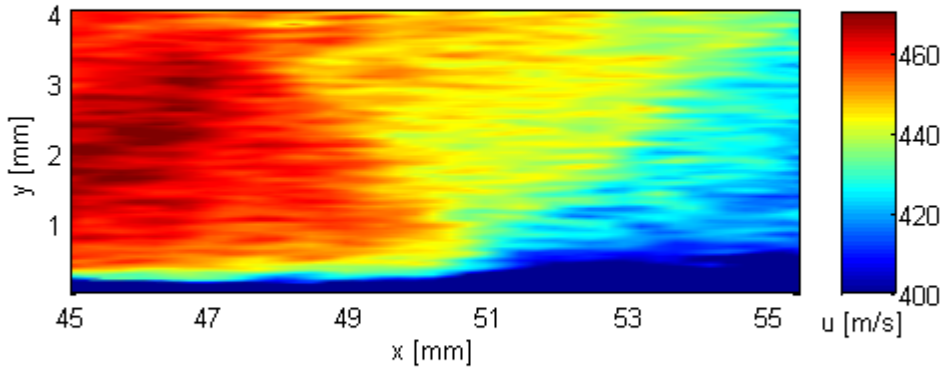

Figure 4.8: Velocity field around a shock. Correlation based on 10 images

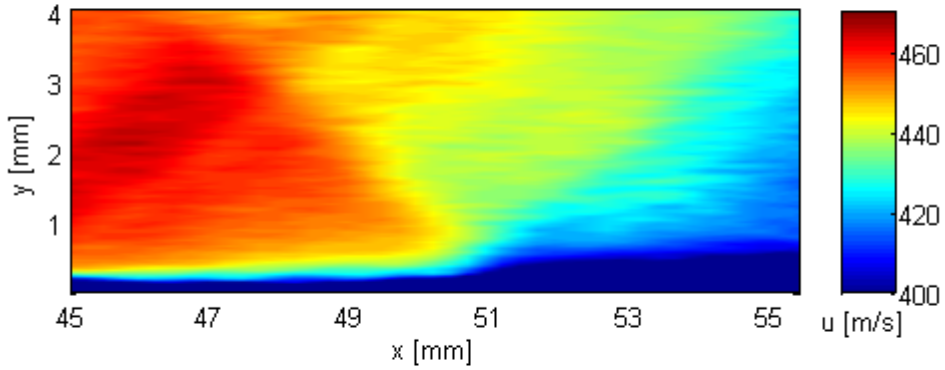

Figure 4.9: Velocity field around a shock. Correlation based on 100 images

To further illustrate the effect of the ensemble size, the u-component of a velocity vector at one location but for different ensemble sizes is determined. For a vector in the freestream, see the left figure in Figure 4.10. The solid line and the bold dashed line indicate the values of the u-component found with an ensemble size of 500, +/- 0.5% and +/- 1.0%, respectively. The difference between the result of an ensemble size of 50 and the result of an ensemble size of 500 is lower than 0.5%. If the ensemble size is increased from 50 to 200 images, the difference when compared to the result obtained with an ensemble size of 500 is even less than 1 m/s. Due to the lower seeding density in the boundary layer and the unsteady nature of the interaction, more images will be needed before a velocity vector close to the wall in the interaction region has converged. This is again investigated at three locations. The first location is approximately 5 mm before the incident shock wave, while the other two locations are within one mm from the incident shock. All vectors are at y = 0.06 mm. The results are presented in the right figure of Figure 4.10. Note that these plots have a different y-scaling than the plots on the left of the figure, and that the value of u(500)+/- 0.5% is no longer indicated in the plots. In this case, significant differences between the convergence at different x-positions can be observed. At x = 45.7 mm, which is upstream of the interaction region, 200 images would suffice. Just downstream of the shock impingement location, at x = 51.2 mm, the minimum number of images that is required to obtain a solution that is within 1% of the solution that is obtained with an ensemble size of 500 images, is approximately 400 images. To ensure a converged solution in case of even less favourable conditions, 500 images of the interaction region will be acquired.

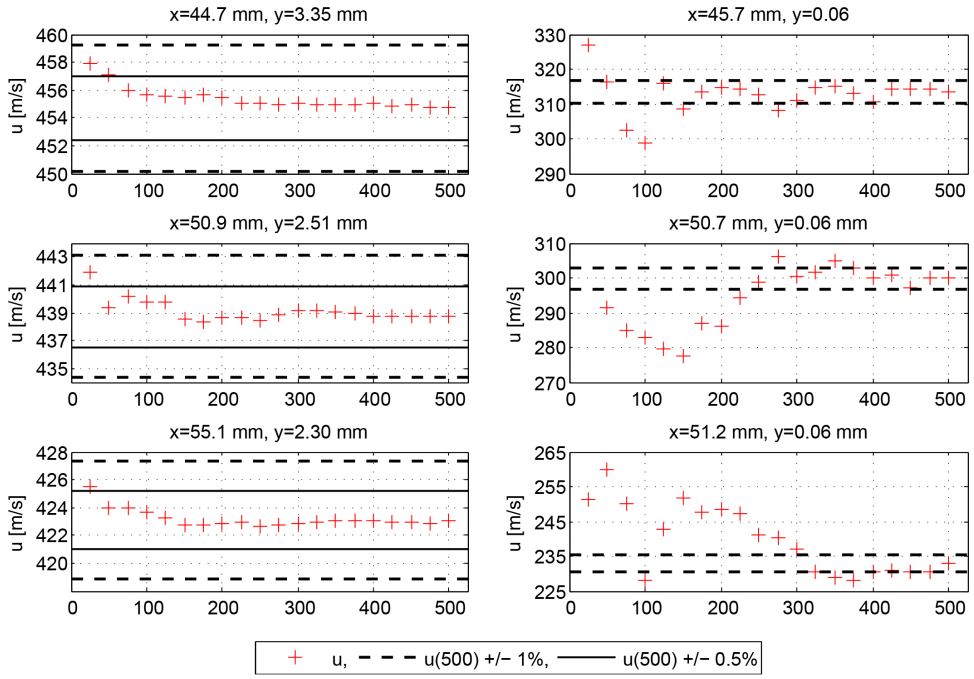

Figure 4.10: Convergence of the u-component of the velocity vector with increasing ensemble size. Left: vectors in the freestream, right: vectors in the boundary layer

4.5 Post-processing

Determining the displacement close to the wall poses some specific challenges. The first challenge is dealing with the reflections of the laser light. While this can already be problematic on the clean flat plate, the severity of the problem increases when the trips are placed on the plate. As the laser is placed downstream of the model, the laser light will be reflected from the trailing edge of the trip, thereby making it impossible to accurately determine the displacement field directly behind the trip. A second challenge is imposed by the lack of seeding close to the wall. While this is a problem everywhere on the plate, there are a few regions in which the lack of seeding affects a larger area (further from the plate). These regions are the non-mixing laminar boundary layer (covering the plate from the leading edge up to the trip location) and the region directly behind the trip. A third problem, which also manifests itself upstream of the trip location, is the lack of light. The reason behind the lack of light is twofold: a part of the laser light will be blocked by the trip and a part will be deflected as a result of the density gradient in the boundary layer. A final complication results from regions in which the velocity is highly fluctuating, such as regions of separated flow. As averaging techniques need to be applied, highly unsteady flow will severely affect the accuracy of the results.

In this section, it is discussed how it is determined which vectors are valid and how the invalid vectors are replaced. Also the way of determining the boundary layer thickness is discussed. A correct determination of the boundary layer is essential for accurately determining the integral boundary layer parameters.

Validity of the vectors close to the wall

To check which vectors obtained from the image correlation are valid, the measured velocity vectors in the log/wake-region are compared to the theoretical turbulent boundary layer profile described by the compressible Log-Wake Law (Equation 4.6) in combination with the Van Driest transformation (Equation 4.7) [48]. Since these relations describe the theoretical velocity profile of a turbulent boundary layer, this method of validation of the vectors is most accurate when applied to a fully turbulent boundary layer. However, it still gives an indication of the validity of the vectors in the regions in which the flow is transitional.

$$\frac{u_{eq}}{v^*} \approx \frac{1}{\kappa} ln\left(\frac{yv^*}{\nu_w}\right) + B + \frac{2\Pi}{\kappa} w\left(\frac{y}{\delta}\right) \tag{4.6}$$

$$u_{eq} = \frac{U_e}{a} sin^{-1}\left(\frac{a\bar{u}}{U_e}\right) \tag{4.7}$$

in which,

$$w \approx 3\left(\frac{y}{\delta}\right)^2 - 2\left(\frac{y}{\delta}\right)^3$$
$$a^2 = 1 - \frac{T_e}{T_{aw}}$$
$$v^* = \sqrt{\frac{\tau_w}{\rho_w}}$$
$$B \approx 5$$
$$\Pi \approx 0.55$$
$$\kappa \approx 0.41$$

When the theoretical profile is plotted in the semi-logarithmic Clauser plot, it is a straight line in the log-law region. Given that the boundary layer thickness behind the trip is of the order of 0.7 mm (see Chapter 5), the log-law region covers $30 \leq y^+ \leq 140$ [34]. By plotting the measurement data (for which v^* needs to be determined iteratively) and the theoretical profile in the Clauser plot, it can easily be determined how many vectors should be replaced. An example of a Clauser plot containing data of the current experiment normalised by the iteratively determined v^* is presented in Figure 4.11. The same data, but now expressed in y and u/u_e, can be seen in Figure 4.13. It is clear that the three vectors closest to the wall are probably invalid vectors and should be replaced.

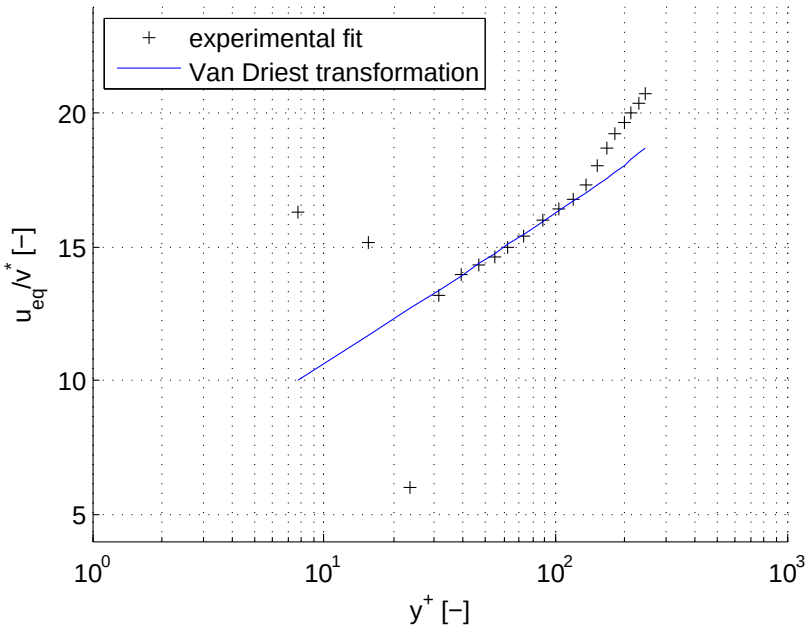

Figure 4.11: Comparison between the experimental data and a theoretical boundary layer profile, x = 59 mm

Replacing erroneous vectors

The velocity in the lower part of the boundary layer can be approximated by a power law fit of the form $u_{nd} = c_1 \cdot y^{c_2}$. The value of c_2 will be approximately 1 for a laminar boundary, since the laminar boundary layer has a linear velocity profile. For a turbulent boundary layer the value of c_2 will decrease to a value of approximately 1/7. For this fit, the first ten reliable vectors are used. The obtained fit is then used to determine the velocity at y-locations smaller than the y-location of the first valid vector. Note that this fit can only be used for an attached boundary layer.

The adjusted boundary layer profile can be seen in Figure 4.12. The adjusted profile seems to be physically correct, in contrast to the original profile.
An incorrect feature of this fit can be seen in the viscous sub-layer, i.e. $y^+ \leq 5$. In this region, the values of u_{eq}/v^* should be lower than the values as predicted by the log-law [48]. However, this mistake is not corrected for, as this discrepancy in the lowest region did not seem to considerably affect the value of the calculated integral parameters.

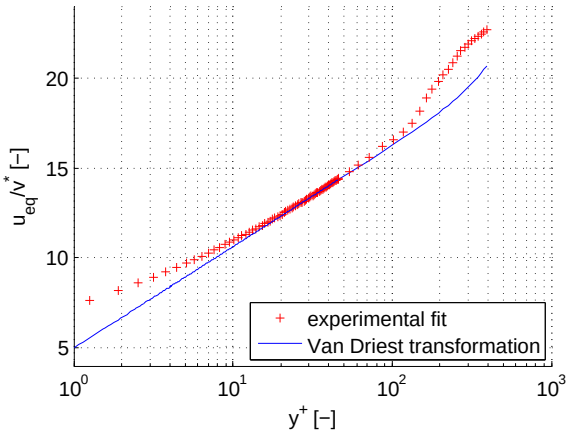

Figure 4.12: Comparison between the fit and a theoretical boundary layer profile, x = = 59 mm

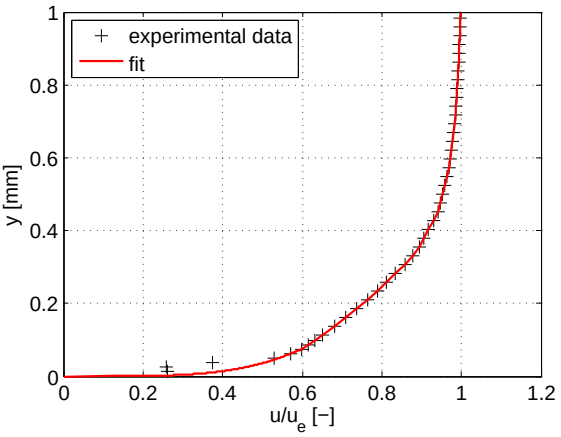

Figure 4.13: Experimentally determined velocity profile and the determined fit, x = 59 mm

Determining the boundary layer thickness

To calculate the integral boundary layer parameters, it is required that the boundary layer thickness is known. In an ideal situation, without flow features such as shock waves and expansion fans, the determination of the boundary layer thickness is relatively straightforward. In that case, the velocity will monotonically increase over the boundary layer until it reaches the freestream velocity at the top of the boundary layer. If the displacement or momentum thickness of such a velocity profile is determined, the upper integration limit will not affect the result as long as it is equal or higher than the boundary layer thickness.

However, due to the presence of shock waves and expansion fans in the flow, determining the boundary layer thickness for the current experiments is not straightforward. The shock waves and expansion fans will result in kinks in the velocity profile, thereby still leading to a variation in u_∞ with y in the freestream. To ensure that the integral boundary layer parameters are indicative of the state of the boundary layer, and not of the freestream, the upper integration limit when calculating the integral boundary layer parameters should therefore be set to the boundary layer thickness and not higher.
The effect of a shock wave on a velocity profile is illustrated in Figure 4.14: while the two profiles show a strong resemblance from $y = 0$ up to $y \approx 1$ mm, the incoming shock wave significantly affects the region $y > 1$ mm. The integral boundary layer parameters of these two profiles will be considerably different (in spite of the similarity of the velocity profiles in the boundary layer), if the upper integration limit is set higher than the boundary layer thickness.

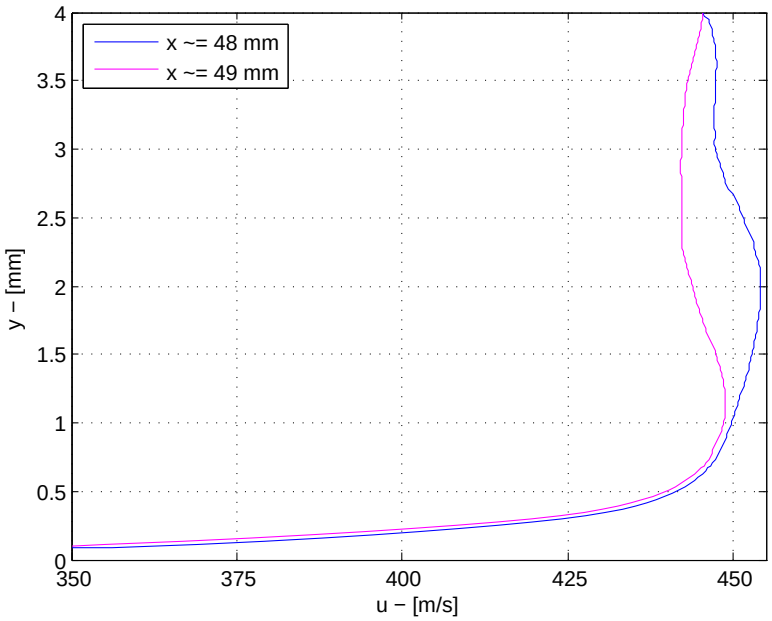

Figure 4.14: Velocity profiles at different x-locations during run with strip placed at 40 mm, $x_{sh} = 51$ mm

To determine the boundary layer thickness, the vorticity field is used. When considering a flat plate, the vorticity field outside of the boundary layer should have a vorticity of zero, i.e. $\xi = 0$. In the ideal situation, δ could then be found by determining the location where the vorticity becomes zero. However, due to the noise in the PIV images, the velocity in the freestream will show small fluctuations, thereby preventing the vorticity from becoming zero. To take this into account, the average vorticity ξ_∞ computed from the upper 40 vectors (covering approximately 3 mm $< y <$ 4 mm) is determined. A study has been performed to find how the freestream vorticity can best be used to find the boundary layer thickness. The resulting variations in δ with x (combined with the vorticity field) are shown for the case without a shock wave in the top figure of Figure 4.15. The behaviour of the boundary layer thickness indicates that for a vorticity threshold value of $\xi_{th} = \xi_\infty$, an area much larger than the true boundary layer is included in the found boundary layer. For higher thresholds, however, not the complete boundary layer seems to have been captured. This is especially the case for $\xi_{th} \geq 8 \cdot \xi_\infty$.
It goes without saying that δ will show a larger and more sudden increase for the cases in which a shock wave is present, compared to the cases in which no shock wave is present. The vorticity field and the found δ-distribution when there is a shock present, is shown in the bottom figure of Figure 4.15. It can be seen that the effect of the threshold in this case, resembles the effect of the threshold for the case without shock: while $\xi_{th} = \xi_\infty$ the found boundary layer seems to include a part of the freestream, the highest thresholds (i.e. $\xi_{th} \geq 8 \cdot \xi_\infty$) do not seem to capture the complete boundary layer.

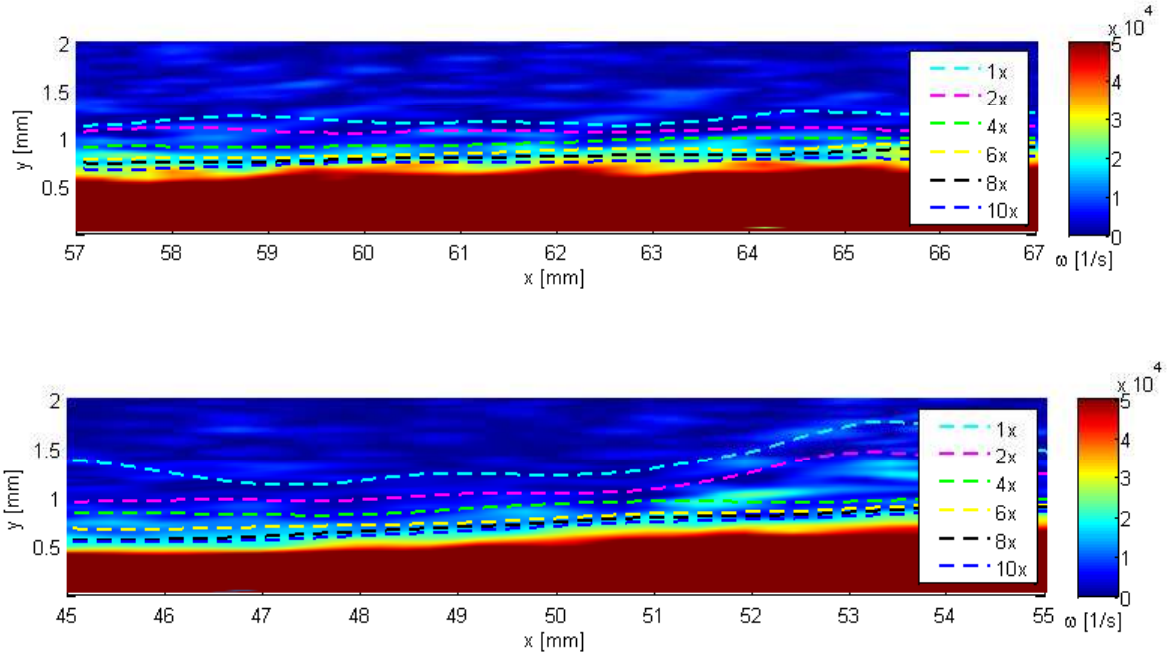

Figure 4.15: The variation in δ with x. Top image no shock, bottom image x_{sh} = 51 mm. Vorticity treshold set at different times the average freestream vorticity

To be able to better quantify the threshold that leads to the correct δ, the results to which the different thresholds led were investigated. The main focus of this study was whether or not the resulting solution could be physically correct. This is checked with the variation in the compressible momentum thickness with increasing x. Since the momentum thickness is proportional to the decrease in momentum flow due to the presence of the boundary layer, and no energy is added to the flow, the momentum thickness can only increase with increasing x. A decrease of momentum thickness should not occur, and would therefore imply that the boundary layer thickness is not set correctly (assuming that the extrapolation to the wall, discussed in the previous section, is correct). Only the resulting momentum thickness of the case with the shock is presented, since this is due to the high gradients a more interesting case than the case without a shock wave. The results for different ξ_{th} are presented in Figure 4.16. It can be seen that the effect of the vorticity threshold on the resulting momentum thickness is significant. It can be seen that if the threshold is set too low, i.e. $\xi_{th} < 4 \cdot \xi_\infty$, θ shows a decrease after the initial steep rise after the shock impingement. For $\xi_{th} = 4$ there is still a decrease in the momentum thickness, albeit much less severe. The general shape does not seem to change significantly for $\xi_{th} \geq 6 \cdot \xi_\infty$. Also the gradient of θ seems to be comparable for $\xi_{th} \geq 6 \cdot \xi_\infty$. To increase the chance that the complete boundary layer is covered while the results remain physically possible, it is chosen to use $\xi_{th} = 6$.

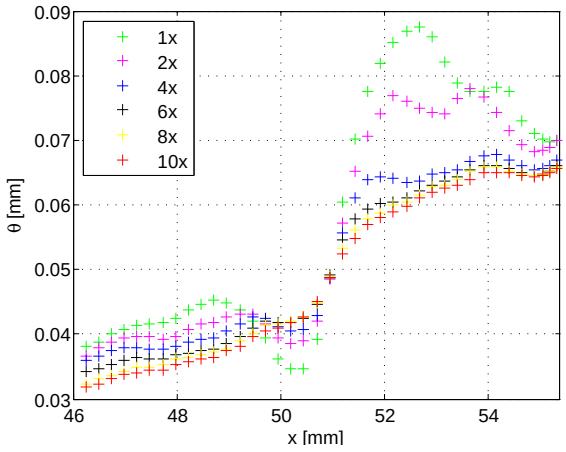

Figure 4.16: The variation in the compressible momentum thickness obtained with different vorticity thresholds

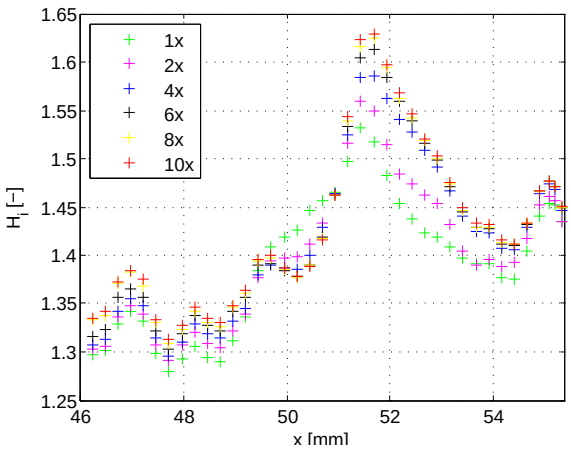

Figure 4.17: The variation in the incompressible shape factor obtained with different vorticity thresholds

Another parameter of interest of this study is the incompressible shape factor. It is therefore also investigated what the effect of the chosen vorticity threshold is on this parameter. The result is presented in Figure 4.17. It can be seen that the peak value for $\xi_{th} < 4$ (which led to non-physical results of the momentum thickness variation) is much lower than for the other thresholds. When comparing the results of $\xi_{th} = 4, 8, 10$ to the results of $\xi_{th} = 6$, a maximum deviation of 2.5% (both positive as well as negative) is found.

4.6 Calculating the parameters of interest

As was described in Section 3.3, several parameters will be used to describe the effect of a trip on a SWBLI. In this subsection it is explained how these parameters can be calculated with the information supplied by the velocity field.

$\delta_i^*, \theta_i, H_i$

The incompressible displacement thickness, momentum thickness and shape factor (the definitions of these parameters can be found in 2.5) can be determined relatively easy if the boundary layer thickness is known. The parameters will be determined using the MATLAB function *trapz*, with the higher limit set at the pre-determined boundary layer thickness.

Drag

The drag of the trip and/or interaction can be determined by calculating the momentum loss over the area of interest. To determine the drag D' Equation 4.8 is used. This equation is applied to the control volume that is presented in Figure 4.18

$$D' = -\oiint_S \left(\rho \vec{U} \cdot dS\right) \vec{U} - \oiint_S p \, dS \tag{4.8}$$

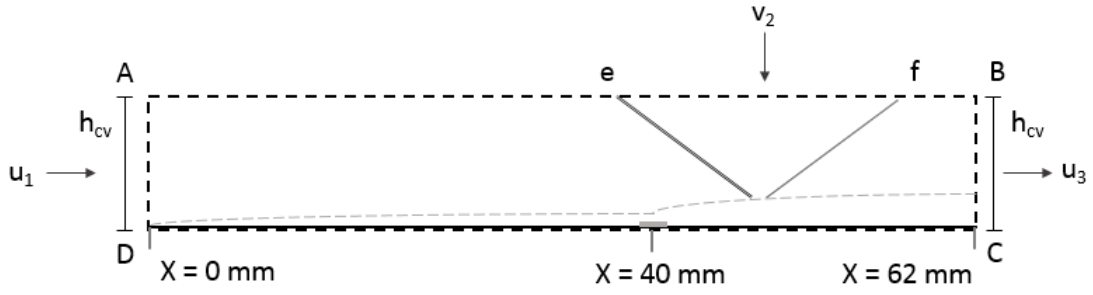

Figure 4.18: The control volume that is used to calculate the drag

The first term on the right hand side of Equation 4.8 describes the inflow and outflow of momentum. The momentum flow can be split into the momentum flux in three regions: region AD, region ef and region BC. In region AD the velocity field is uniform and normal to the plane. In plane BC the flow will no longer be uniform, as a result of the boundary layer formation. The flow will, however, be normal to the plane again. The momentum flux

through plane ef depends on v_2 and u_2. The flow across this plane is assumed to be uniform. The total momentum flux can now be rewritten as follows:

$$\oiint_S \left(\rho \vec{U} \cdot dS\right) \vec{U} = h_{CV}\rho_1 u_1^2 + v_2 \cdot u_2 \rho_2 \cdot (x_f - x_e) - \int_0^{h_{CV}} \rho u^2 \, dy \tag{4.9}$$

The upper boundary of the control volume is parallel to the flat plate, leading to $y_B - y_C = y_A - y_D = h_{CV}$. The pressure on top of the control volume will then cancel out the contribution of the pressure on the lower side of the control volume, i.e. the wall. The pressure acting on plane AD and plane BC are not equal, but are both assumed constant over the plane. The pressure term can then be rewritten as follows:

$$\oiint_S p \, dS = h_{CV}p_3 - h_{CV}p_1 \tag{4.10}$$

Substituting these equations into Equation 4.8 leads to the final equation that is used to calculate the drag:

$$D' = h_{CV}\left((p_1 - p_3) + u_1^2\rho_1\right) + v_2 \cdot u_2\rho_2(x_f - x_e) - \int_0^{h_{CV}} \rho u^2 \, dy \tag{4.11}$$

For an inviscid interaction, all parameters can be determined based on the initial freestream conditions and the shock wave relations. Since the flow needs to be parallel to the wall downstream of the reflected shock, it is also known that the deflection angle of the second shock equals the deflection angle of the incident shock, i.e. $\theta = 3°$. The resulting parameters in the region before the incident shock wave, the region in between the incident and reflected shock wave and downstream of the reflected shock wave (respectively region I, II, III) are presented in Table 4.3.

When these values are substituted in Equation 4.11, it is found that $D' \approx 0$ N/m (the contribution to the total drag per term is presented in Table 4.4. This is to be expected, since the total drag of a flat plate parallel to the freestream is determined by the friction drag only. In an inviscid flow, however, there can be no friction drag.

The application of Equation 4.11 to the PIV results is substantially more complicated, since now only the measured velocity is available. The pressure is not readily available; instead the theoretical pressures as calculated with the shock wave relations need to be used. It goes without saying that this will decrease the accuracy of the momentum balance. Besides the pressure, the density has not been measured either. This can, however, be solved indirectly

Table 4.3: Flow parameters of an inviscid interaction, as determined with the shock wave relations

		region		
		I	II	III
p	Pa	$47 \cdot 10^3$	$54 \cdot 10^3$	$63 \cdot 10^3$
ρ	kg/m^3	0.93	1.04	1.15
T	K	174	182	190
Ma	-	1.7	1.6	1.5
$\vec{U}$	m/s	449.5	432.4	414.1
u	m/s	449.5	431.8	414.1
v	m/s	0	22.6	0

Table 4.4: Contributions to the drag, split up into the pressure and momentum terms

momentum	left	-752	N/m
	top	-101	N/m
	right	+791	N/m
pressure	left	-186	N/m
	right	+252	N/m

by using the Crocco-Buseman relation in combination with the assumption of an adiabatic wall:

$$\bar{T} \approx T_e + \frac{r}{2c_p}\left(U_e^2 - u^2\right) \tag{4.12}$$

in which $\bar{T}$ is the local temperature in Kelvin, T_e is the freestream temperature and c_p is the specific heat at constant pressure. For c_p, the constant value of 1004 $JK^{-1}kg^{-1}$ is used. Finally, r is the recovery factor and equals $r \approx 0.89$ for a turbulent flow and $r \approx 0.85$ for a laminar flow [48]. With this relation the ratio of the freestream temperature to the local temperature can be determined. If the pressure is constant, $T_\infty/T = \rho/\rho_\infty$. Thus, if it is assumed that the freestream density is equal to the theoretical freestream density after an inviscid interaction, it will be possible to determine the local density.

4.7 Limitations of the PIV experiment

As explained in this chapter, there are several challenges when performing the PIV measurements. As a consequence of these challenges, there are certain limitations on the information that can be derived from the results. All the following aspects lead to either a decrease in the accuracy of the results, or make it impossible to determine certain properties.

- **The determination of the velocity vectors in the close proximity of the wall**
  The low seeding density and reflections of the laser light on the flat plate and/or trip, make it difficult to accurately determine the velocity vectors which are in close proximity to the wall. On average, approximately the first 5 vectors (corresponding to the first 0.06 mm) are deemed invalid. These vectors will be replaced by a fit that is based on the higher located vectors. It goes without saying that while replacing these vectors increases the accuracy of the solution, some inaccuracies will remain.

- **The window size**
  In Section 4.4 a study on the window size was presented. Based on a compromise between the number of particles in a window and the spatial resolution, it was decided to select a window size of 128 $\times$ 12 pixels, or 1 $\times$ 0.09 mm. It should be noted that as a result of this window size, small flow features can be filtered out of the solution. The window size can also result in a flattening of steep gradients, such as present in the region of the shock waves.

- **The determination of the boundary layer thickness**
  As has been discussed in Section 4.5, the presence of shock waves and expansion fans makes it hard to accurately determine the boundary layer thickness. In that section, it is also discussed how the boundary layer thickness is determined on the basis of the local vorticity. If the boundary layer thickness is set at an incorrect value, the values of the integral boundary layer parameters will show inaccuracies as well. It was shown that the incompressible shape factor H_i can vary up to 4%, depending on which vorticity level is used in the determination of the boundary layer thickness.

- **The particle slip**
  The tracer particles will not be able to instantly adjust to new conditions. In Section 4.1 it was determined that under the present test conditions, the tracer particles have a relaxation time of 2.12 μs. Especially when travelling trough the shock wave, after which the velocity is suddenly decreased, the particles will have a substantial velocity relative to the flow. This particle slip leads to a broadening of the measured shock wave when compared to the actual shock wave.

- **The Stokes number**
  The Stokes number is defined as $S_k = \tau_p/\tau_f$, in which τ_f is a time scale of the flow. In order for the seeding particles to accurately track the flow at time scale τ_f, it is required that $S_k << 1$ [44]. For the time scale of the largest turbulent structures in the boundary layer, $\tau_f = \delta/U_\infty$ is used. Under the current conditions, δ ranges from approximately 0.2 mm for the incoming boundary layer at the trip up to approximately

0.8 mm after the interaction (these values are presented in Section 5.1 and Section 5.3, respectively). This would lead to a τ_f between $\tau_f = 0.2 \cdot 10^{-3}/450 = 0.44\mu s$ and $\tau_f = 0.8 \cdot 10^{-3}/450 = 1.78\mu s$. Inserting the particle relaxation time $\tau_p = 2.12\mu s$ leads to $1.2 \leq S_k \leq 4.8$. Apparently, it is impossible for the seeding to accurately follow turbulent structures in the boundary layer at any location on the model.

Chapter 5

Experimental results

To get a visual impression of the flow field, Schlieren visualisations are used. The Schlieren visualisation of the clean case is presented in Figure 5.1. This case, in which no trips are placed on the model, will serve as the reference case. The visibility of the expansion fan indicates that there is a strong interaction. The expansion fan is preceded by the compression waves that result from the thickening of the boundary layer. Apparently, the thickening starts a significant distance upstream of the shock impingement location: the first compression waves originate approximately 10 mm upstream of the incident shock wave. This suggests that the separation bubble will be of substantial size. The expansion fan is followed by the reattachment compression waves.

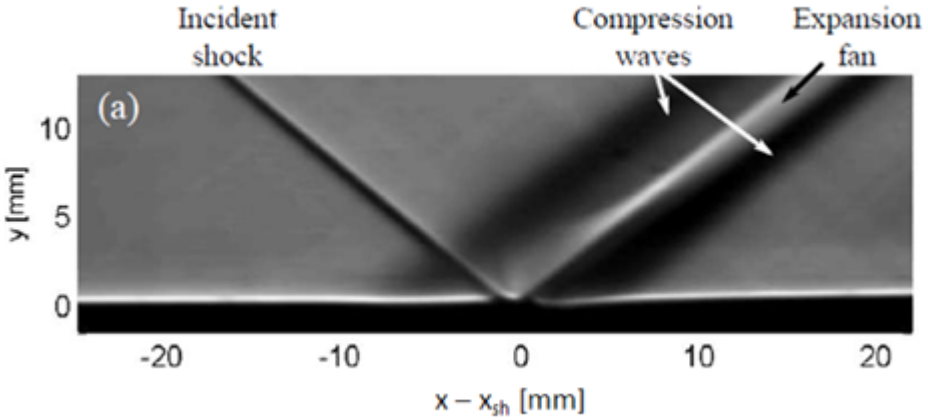

Figure 5.1: Schlieren visualisation of the flow field, no trip (reference case) [24]

The Schlieren visualisations of the experiments with the different trips are presented in Figure 5.2. The flow fields resulting from the different trips are all comparable. There are compression waves upstream and downstream of the trip, while an expansion fan is present on top of the trip. Also visible in the visualisations is the variation in the trip width: while the step and the distributed roughness span approximately 2 mm, the zig zag strip spans 6 mm. A distinct difference when comparing these visualisation to the reference case, is that no expansion fan can be observed. The absence of an expansion fan would indicate that the interaction has weakened and that there is no separation. The fact that the interaction is weaker when a trip is placed can also be inferred by the significantly shorter interaction length. In all three cases, the reflected shock wave is formed close to the impingement location of the incident shock wave.
The most significant difference between the three visualisations is the width of the reflected shock waves. The reflected shock of the step spans a wider area than the reflected shock waves of the zig zag strip and the distributed roughness. This might indicate that the interaction length of the step is longer when compared to the other trips.

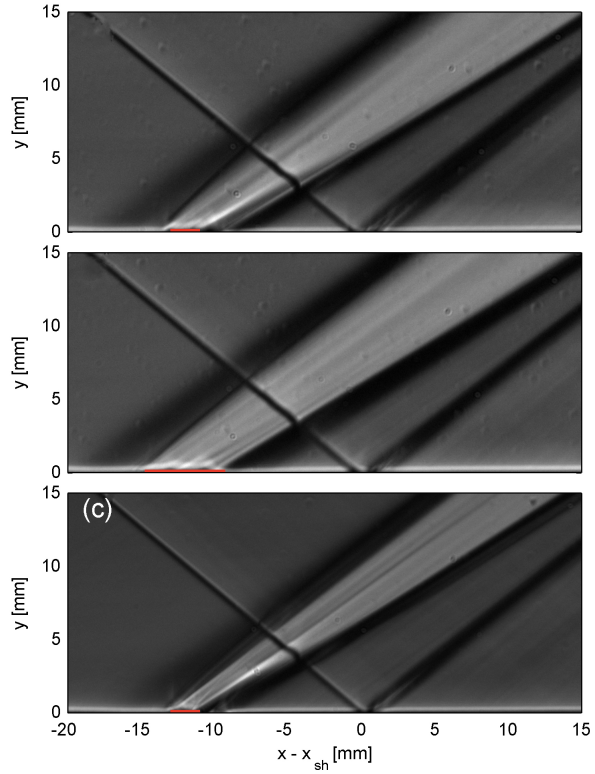

Figure 5.2: Schlieren visualisations of the flow field. From top to bottom: (a) step, (b) zig zag strip and (c) distributed roughness.

The velocity field of the three interactions is also determined by means of PIV. First, to get a clear overview of the shock system, the velocity field is determined with a relatively large FOV: 25 mm $\times$ 12 mm. For this FOV the resulting spatial resolution has been decreased to approximately 65 pix/mm while the separation time Δt has been increased to 800 ns. The resulting images are presented in Figure 5.3. The same features that are present in the

Schlieren visualisations can also be seen in these images. An additional feature, the velocity overshoot in the region of the shock wave, is a PIV artefact resulting from the inhomogeneous density field.

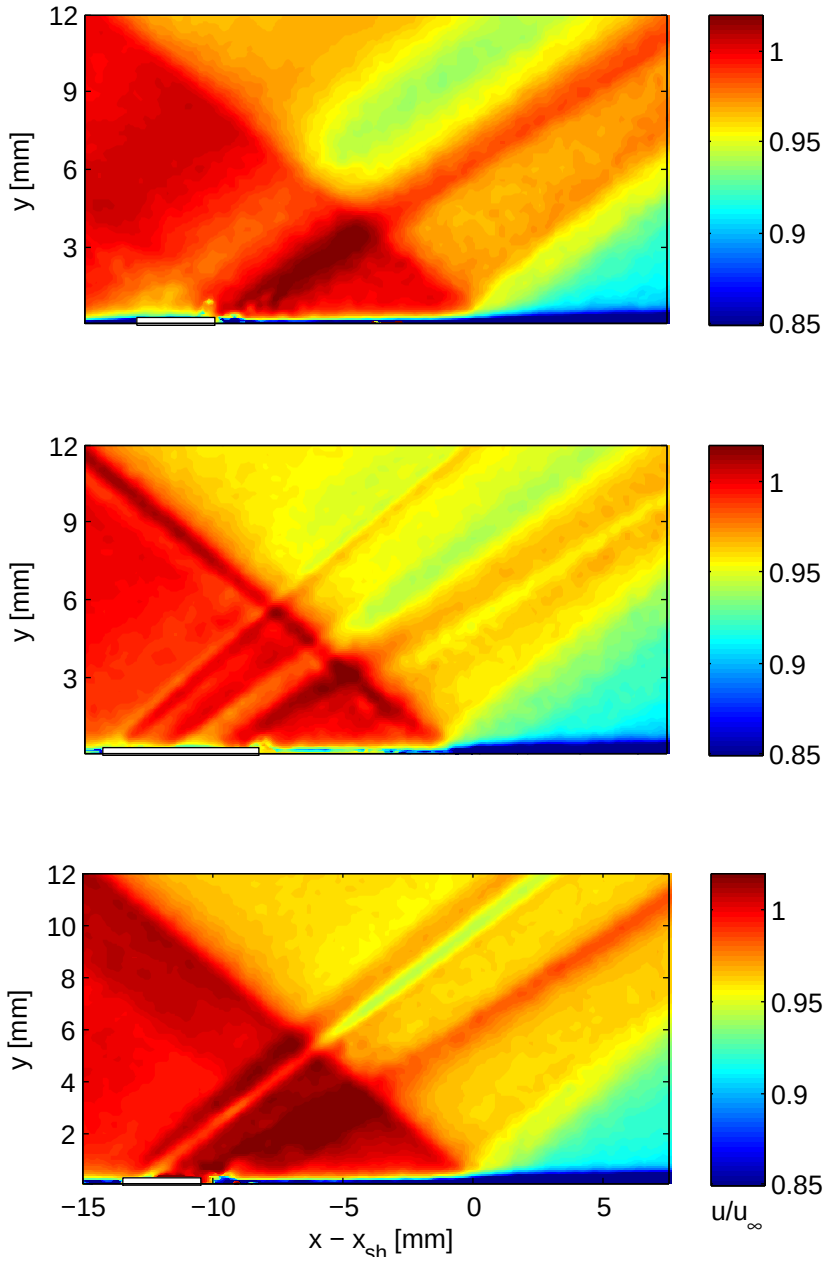

Figure 5.3: Velocity field around the SWBLI. From top to bottom: the step, the zig zag strip and distributed roughness.

It is evident that the Schlieren images and the velocity field determined with the large FOV are not sufficient to draw a sound conclusion on which trip is the most effective. In order to draw a conclusion on the difference in effectiveness, PIV images with a higher spatial resolution are used. It has been presented in Section 4.1 that if a spatial resolution of 130 pix/mm is required, the FOV of the camera will be limited to approximately 12.5×5.0 mm. This FOV is too small to capture the whole area of interest in one run. As a consequence, multiple runs with different FOVs will be performed from which the results are stitched together. To allow for the stitching, an overlap of approximately 4 mm between the FOVs of subsequent runs is required. A graphical overview of the location of the different small FOVs, as well as the large FOV measurements, with respect to the interaction can be found in Figure A.1, page 87.
On the basis of the displacement field that is obtained from the high-resolution PIV images, the parameters of interest are determined. To strengthen the conclusions on the flow topology that are drawn based on the result of the PIV measurement, oil flow measurements are used.

In the first section of this chapter, the case without tripping device is presented. This case will serve as the reference case throughout the remainder of this report. In the second section, high-resolution PIV velocity fields will be used to check if there is indeed no separation as a result of the SWBLI when a tripping device is placed on the model. Subsequently, the parameters of interest are presented: the integral boundary layer parameters, the interaction length and the drag. All of these parameters are compared to the parameters of the other trips and to the parameters of the reference case. In addition to the main experiment, where $x_{sh} = 51$ mm, it is also investigated how a decreased distance between the shock wave and the trip affects the boundary layer development. In this additional test-case the trips are placed at the same location (x = 40 mm), while the shock position is shifted to $x_{sh} = 46$ mm. For this additional case, only the step and distributed roughness are investigated. The results are presented in the final section of this chapter. The experimental matrix of all PIV measurements is presented in Table A.1,88.

5.1 Benchmark test-case

To determine the efficiency of the trips, the resulting flow fields are compared to the clean case. Two separate comparisons can be made. The first comparison is between the flow field of the clean case when no shock is present, C_{ns}, and the flow field resulting from the trip when no shock is present T_{ns}. From this comparison, the additional drag due to the presence of the trips can be determined. The additional drag is important if the trips are placed at locations at which a shock wave is not permanently present. Besides the drag, this comparison is also used to determine if the roughness elements have tripped the boundary layer.
For the second comparison a shock wave is impinging on the flat plate and the flow is studied for the case with (T_s) and without trips (C_s) The second comparison will be between the flow fields of the clean case while a shock is present C_s and of the trip while a shock is present T_s. This way, it can be determined if and how beneficial a trip can be in the presence of an incident shock wave.

Clean case, no shock

The clean case without a shock wave is investigated by *Giepman et al.* [22]. The integral boundary layer parameters of this benchmark at two locations are used for the comparison: x = 38 mm and x = 62 mm. The first location is positioned just upstream of the location of the trips, which are applied at x = 40 mm. The second location is 22 mm behind the streamwise centre of the trip and 11 mm downstream of the incident shock wave. This location is chosen as it is the most downstream location at which data for all four cases (i.e. C_{ns}, C_s, T_{ns}, T_s) is collected. It is expected that at this location the boundary layer will have recovered from the interaction.

The velocity profiles at the specified locations are presented in Figure 5.4. It can be seen that δ_{99} increases from $\delta_{99} \approx 0.2$ mm at x = 38 mm to $\delta_{99} \approx 0.3$ mm at x = 62 mm. The boundary layer thickness combined with the linear character of the profiles seems to indicate that the boundary layer is still laminar at x = 62 mm. This is confirmed by the values of the integral boundary layer parameters, presented in Table 5.1: the shape factor only decreases from $H_i = 2.66$ to $H_i = 2.37$ when comparing the boundary layer at x = 38 mm and x = 62 mm.

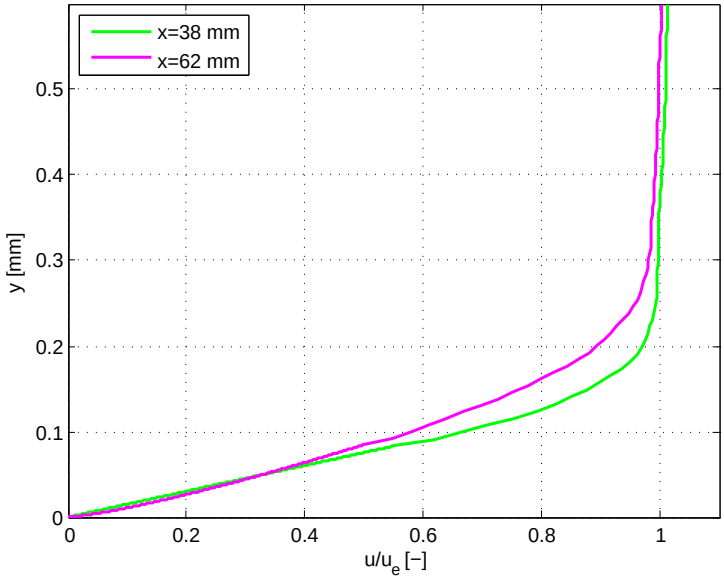

Figure 5.4: Velocity profiles of the clean case, no shock

Table 5.1: Boundary layer parameters, clean case, no shock

		x = 38 mm	x = 62 mm
H_i	[-]	2.66	2.37
δ_i	[mm]	0.082	0.101
θ_i	[mm]	0.031	0.043
θ	[mm]	0.025	0.035

As previously discussed, the FOV of the camera is too small to capture the whole area of interest in one run. This means that multiple runs with different FOVs need to be performed to cover the region between x = 38 mm and x = 62 mm. As the boundary layer is very sensitive to surface roughness, it is possible that transition occurs prematurely due to deposition of seeding on the model. Therefore, to ensure that all the runs that are used in this research are comparable to the benchmark case in terms of the incoming boundary layer, one camera is permanently focussed on the region upstream of the trip. While the shadow of the trip impedes determining the velocity vectors close to the wall, sufficient information can be deduced from the velocity profiles to determine whether the boundary layer was laminar or turbulent.
Examples of a laminar velocity profile and a turbulent velocity profile, obtained during different runs but at the same x-position, are presented in Figure 5.5 and Figure 5.6. The black crosses represent the vectors as found by Fluere, the blue line the theoretical compressible Blasius solution and the pink line the fit as determined during the post-processing. Even though the lower vectors cannot be used, the boundary layer thickness and the fact that the lower part of the velocity profile in Figure 5.5 is much better approximated by a Blasius fit than the velocity profile in Figure 5.6 indicates that the first profile is laminar, while the second is already turbulent. If the incoming boundary layer was found to be turbulent, the plate would be polished with sand paper with a roughness of $P1200$ to make the surface smooth again. This was in all cases sufficient to ensure a laminar incoming boundary layer for the subsequent run.

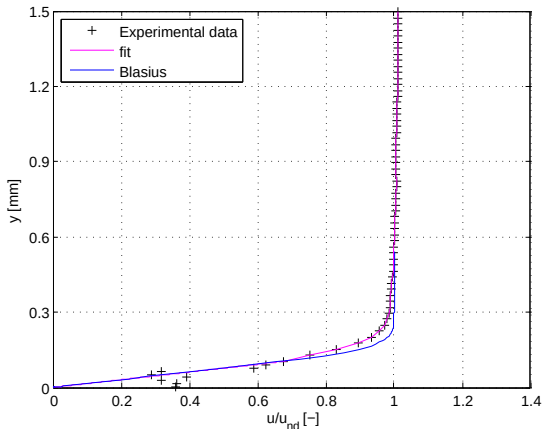

Figure 5.5: Laminar incoming boundary layer, $x \approx 31$ mm

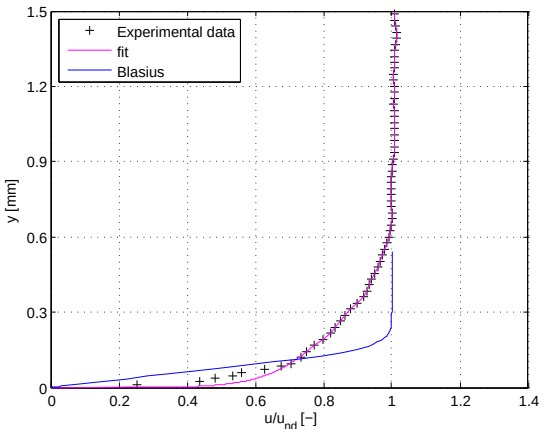

Figure 5.6: Turbulent incoming boundary layer, $x \approx 31$ mm

Clean case, with shock

The clean case with a shock impinging at x = 51 mm has been investigated by *Giepman et al.* [23]. It was found that if a shock wave that results from a shock generator with a flow deflection angle of 3° impinges on the boundary layer at 51 mm, the laminar boundary layer will separate. The resulting flow field can be seen in Figure 5.7. The separation bubble is covered by a white patch, and spans the region of approximately 7 mm upstream of x_{sh} up to 3 mm downstream of x_{sh}. The maximum height of the bubble is approximately 0.2 mm. Downstream of x_{sh}, there is region in which the flow is accelerated. This indicates that there is an expansion fan; one of the features of a strong interaction. The same conclusion was earlier drawn based on the Schlieren visualisation of the interaction (see Figure 5.1).

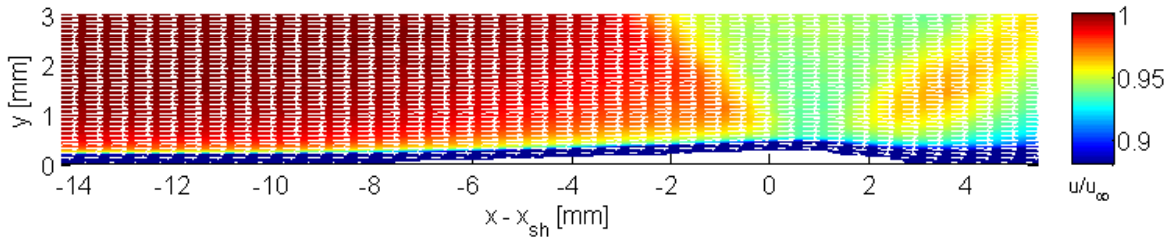

Figure 5.7: Velocity field around the shock wave, no trip. The region in which the flow is separated is covered by a white patch.

As a result of the low seeding density, ensemble correlation had to be applied to obtain this velocity field. The low seeding density also prevented the solving of the flow in the separation bubble. The lack of data in this region makes it impossible to determine the development of the integral boundary layer parameters. However, since the flow reattaches approximately 3 mm downstream of the incident shock wave, the integral boundary layer parameters can be determined at positions downstream of the interaction. To compare this case with the cases of the trips, the integral boundary layer parameters are determined at x≈ 62 mm. These values can be found in Table 5.2. As expected, the boundary layer will no longer be laminar. While the incompressible shape factor of the clean case without the shock was H_i=2.37 at x = 62 mm, this decreases to H_i=1.31 if there is a SWBLI. The incompressible momentum thickness will increase from 0.043 mm to 0.072 mm, the compressible momentum thickness will increase from 0.025 to 0.064 mm. The decrease in the incompressible displacement thickness will be relatively small when compared to the difference in momentum thickness: δ_i^* decreases from 0.101 mm to 0.094 mm.

Table 5.2: Boundary layer parameters, clean case with shock

		x = 62 mm
H_i	[-]	1.31
δ_i^*	[mm]	0.094
θ_i	[mm]	0.072
θ	[mm]	0.064

To investigate the flow topology on the surface of the model, an oil flow measurement is performed as well. The resulting oil film can be seen in Figure 5.8. The most important features are numbered. The '1' indicates the start of the separation bubble. Due to the opposing direction of the flow on the plate at the start of the separation bubble, an accumulation of oil will be present where the flow separated. The '2' indicates the location of the incident shock wave, which is accompanied by a shorter region in which the oil has accumulated. This accumulation is a result of the pressure gradient induced by the shock wave. It should also be noted that upstream of the interaction, the remaining oil film is much thicker than downstream of the interaction. This dissimilarity results from the different states of the boundary layer: while the incoming boundary layer is laminar, the boundary layer is turbulent after reattachment. The turbulent boundary layer has an increased shear stress when compared to a laminar one, and will therefore 'push' more oil in the downstream direction. This results in a thinner oil film in the turbulent regions. Due to the fact that the oil accumulates around the separation line and at the shock impingement location, while the oil is again transported downstream after the interaction, an especially dark region appears just after the shock impingement location.
A final feature of the flow that is visualised with the oil flow measurement, is the effect of the walls of the tunnel. On these walls, there will be a thick turbulent boundary layer. This results in a turbulent wedge upstream of the interaction. This region, which is limited to the sides of the plate, is indicated with the '3'.

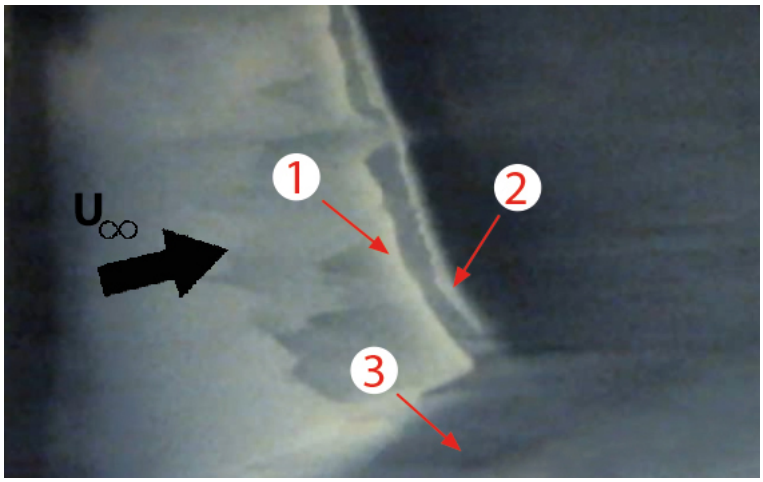

Figure 5.8: Oil flow measurement of the clean case, with an incident shock

5.2 Separation

The main objective of placing the trips is to prevent separation. Based on the Schlieren visualisations, it was concluded that it is unlikely that there is separation. To further strengthen this conclusion, the results of the PIV measurements and the oil flow measurements are now discussed. The resulting oil films are presented in Figure 5.9. In these figures, only one oil flow accumulation can be observed. Based on the relatively small size of the accumulation, it is expected that this accumulation is a result of only the shock wave, and not of separation. This is in agreement with the conclusion that was drawn based on the large FOV PIV images (Figure 5.3 and the Schlieren visualisations (Figure 5.2.

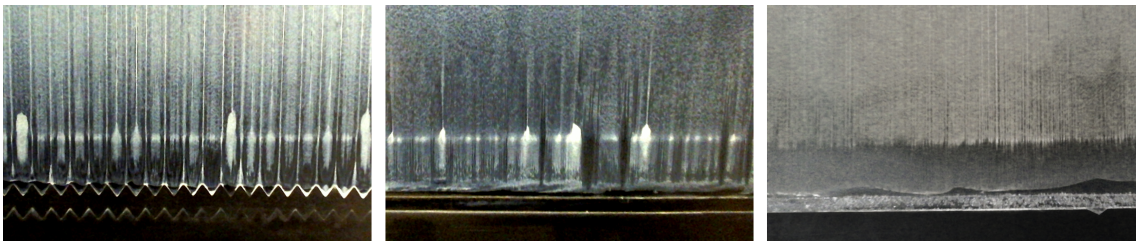

Figure 5.9: Oil flow measurement of the SWBLI behind a trip, $x_{sh} \approx 51$ mm. From left to right: the zig zag strip, the step and the distributed roughness. The flow direction is from bottom to top.

The PIV images, centred on the interaction region, can be seen in Figure 5.10 (the u-component) and in Figure 5.11 (the v-component). No negative values of the u-component of the velocity are observed, which indicates that there is no separation. The absence of a region in the freestream in which the flow accelerates (inherent to the presence of an expansion fan), such as is present in Figure 5.7, also strengthens the conclusion that there is no separation if a trip is placed on the model.

The flow fields, especially the u-component of the velocity, behind the different trips are very similar. When looking at the v-component of the velocity, the main differences are observed in the region between the trips and the incident shock wave. In the velocity field behind the zig zag strip, for example, more variation in the v-component of the velocity is present. This is expected to be a result of the larger width and the 3D shape of the zig zag strip. A relatively high value of the v-component in this region is observed behind the distributed roughness. This cannot be explained on the basis of the Schlieren visualisations, but can be a result of the thickening of the boundary layer.
However, the global structure of the velocity field is comparable behind the three trips. No clear differences are observed when looking at the shock angle of the reflected shock wave and the interaction length. Therefore, no sound conclusions on the difference in effectiveness between the trips can be drawn from the visual inspection of these images. These conclusions will have to be based solely on the integral boundary layer parameters, and the more precise determination of the interaction length.

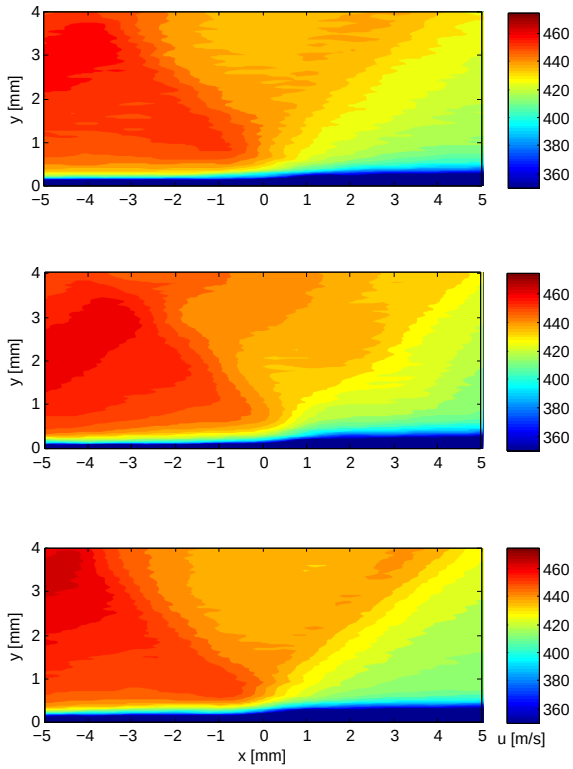

Figure 5.10: The u-component of the velocity. From top to bottom: the step, the zig zag strip and the distributed roughness

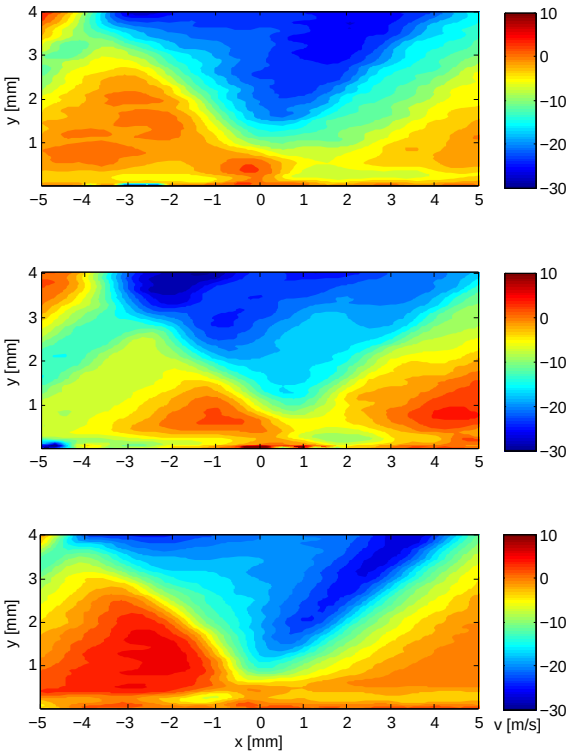

Figure 5.11: The v-component of the velocity. From the top to bottom: the step, the zig zag strip and the distributed roughness

5.3 Boundary layer development

In this section the variation of the incompressible displacement thickness, momentum thickness and the resulting shape factor is presented. The reason to determine the incompressible shape factor instead of the compressible shape factor, is that the incompressible shape factor is a measure of the fullness of the boundary layer without incorporating density effects.

The first trip to be discussed is the step. The variation in δ_i^*, θ_i and H_i are presented in Figure 5.13, Figure 5.14 and Figure 5.15, respectively. For the case without a shock, no data is presented for $x < 54$ mm. The data that was obtained in this region did not lead to valid vectors in the proximity of the wall. As a result of this, no good fit could be obtained. To show that the boundary layers for the case with and without shock wave are comparable, the fit for the run with and the (valid) experimental data for the case without a shock wave a presented in Figure 5.12. It can be observed that the data for $y > 0.15$ mm of both profiles is comparable.

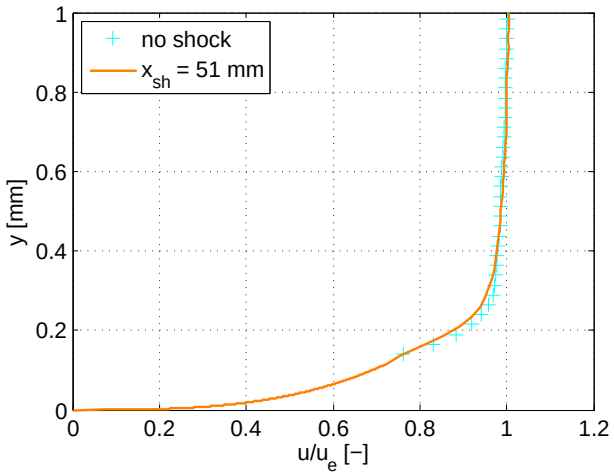

Figure 5.12: Velocity profiles at x = 46 mm

Due to the missing data, it cannot be stated at which location the boundary layer will have transitioned into a fully turbulent state. However, since H_i has reached the turbulent value of 1.4 at x = 55 mm, it can be stated that the transition location is upstream of x = 55 mm. For the case with a shock, a relatively steep gradient of all integral boundary layer parameters at x $\approx$ 52 mm is observed. The maximum shape factor is $H_i = 1.80$ and is measured at x = 51.8 mm. This value of the shape factor indicates that there is no separated flow. At $x \approx 60$ the incompressible shape factor downstream of the shock wave is again comparable to the incompressible shape factor of the case in which no shock wave is present.
In Figure 5.13 and Figure 5.14 a sudden rise in respectively the incompressible displacement thickness and incompressible momentum thickness can be seen. This rise starts at $x \approx 50$ mm, ans is a consequence of the thickening of the boundary layer in the interaction region.

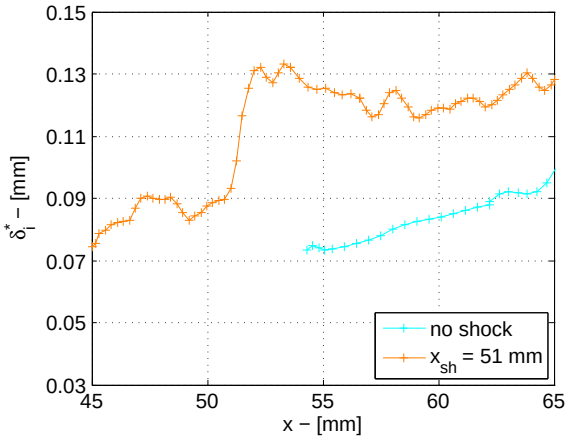

Figure 5.13: Displacement thickness variation with x. Trip = step

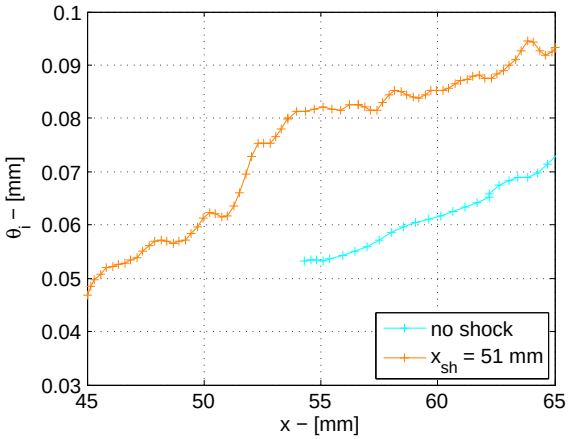

Figure 5.14: Momentum thickness variation with x. Trip = step

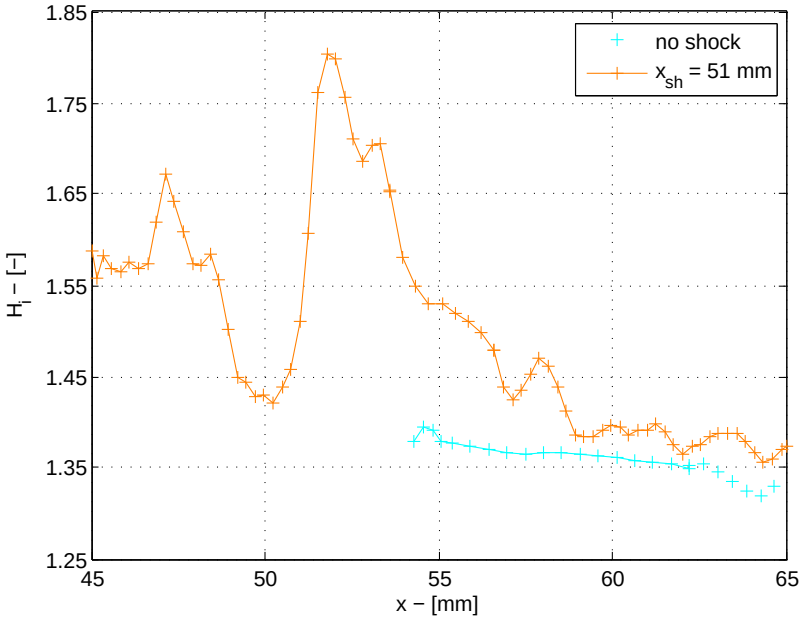

Figure 5.15: Shape factor variation with x. Trip = step

The same plots, but now for the zig zag strip, are presented in Figures 5.16-5.18. For this trip, the difference between the determined δ_i^* and the θ_i of the incoming boundary layer for the case with and without shock is much less substantial. The small differences do, however, lead to a clear difference between the determined shape factors.
When comparing the values of the integral boundary layer parameters to those of the case with the step, it is clear that the maximum shape factor is much lower: the maximum has decreased to $H_i = 1.60$. This is in agreement with another difference between the two trips, namely the state of the incoming boundary layer. The boundary layer parameters for the case of the zig zag strip imply that the boundary layer is already turbulent at x = 46 mm, whereas for the step the boundary layer is still in a transitional state at this location.
Besides the peak in the shape factor, there is a second notable effect of the shock wave on the shape factor. If there has been a shock wave, the shape factor settles at a value slightly higher than the value at which the shape factor would settle in the absence of a shock wave. For the step, the difference between the values at which the shape factor settles is smaller. However, these values are both comparable to the value of the zig zag strip in case there is a shock wave. A shape factor as low as the shape factor at a distance between the zig zag strip, $H \approx 1.3$ is not encountered when the step is used to force transition.
The behaviour of δ_i^* and the θ_i is comparable for both trips. Both the momentum thickness and the displacement thickness are initially lower. This was expected since the zig zag strip should enhance the mixing. At x = 65 mm, δ_i^* and θ_i for the cases of the step and the zig zag strip (without the shock) are comparable.

The final trip to discuss is the distributed roughness. The integral boundary layer parameters of this trip are presented in Figures 5.19-5.21. Also for this trip, the difference between the variation of the parameters upstream of the interaction is remarkable. Again, it seems that the data of the measurement with the shock shows non-physical behaviour as a result of an incorrect fit due to the limited amount of valid data at small y.
Although the peak value of the incompressible shape factor is lower than for the case with the step, i.e. a peak value of $H_i = 1.71$, both the incompressible momentum and displacement thickness are higher after the shock. Apparently, the boundary layer is thicker behind the interaction in case distributed roughness is used instead of the step.

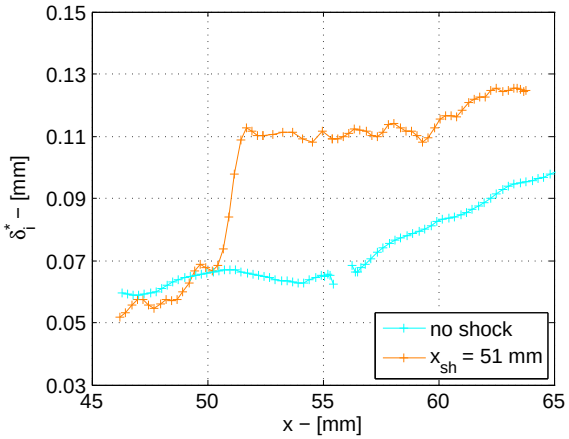

Figure 5.16: Displacement thickness variation with x. Trip = zig zag strip

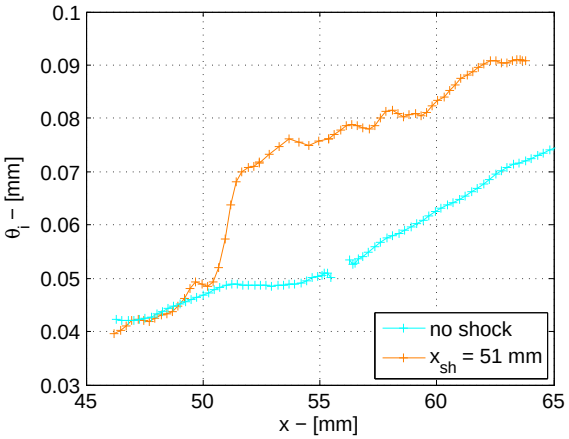

Figure 5.17: Momentum thickness variation with x. Trip = zig zag strip

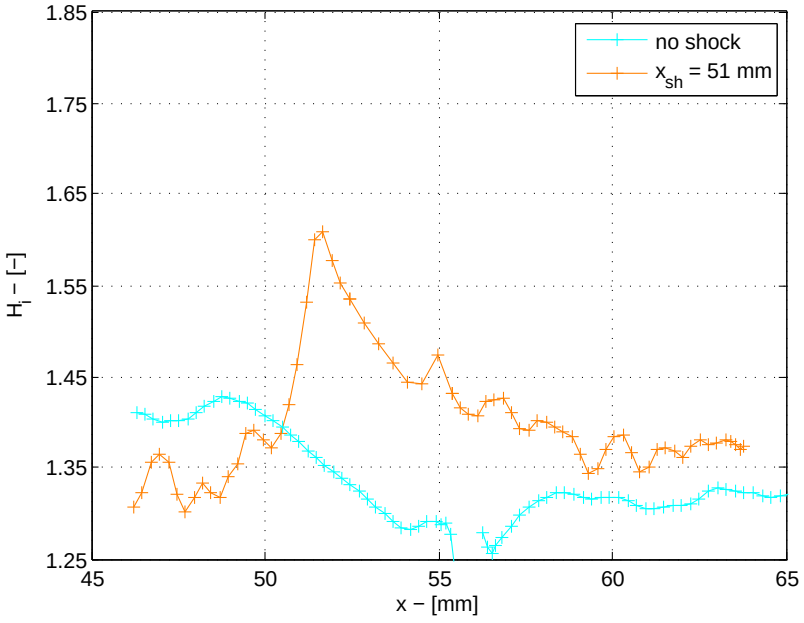

Figure 5.18: Shape factor variation with x. Trip = zig zag strip

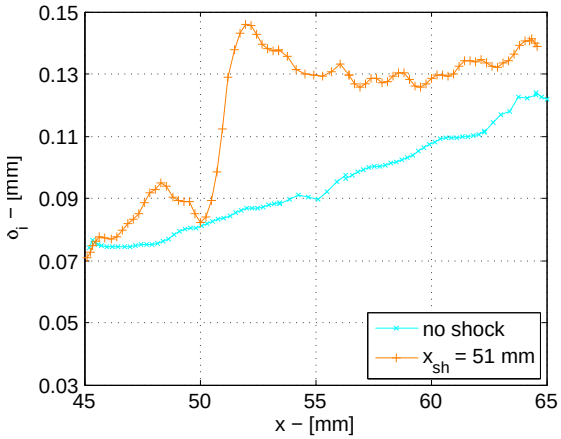

Figure 5.19: Displacement thickness variation with x. Trip = distributed roughness

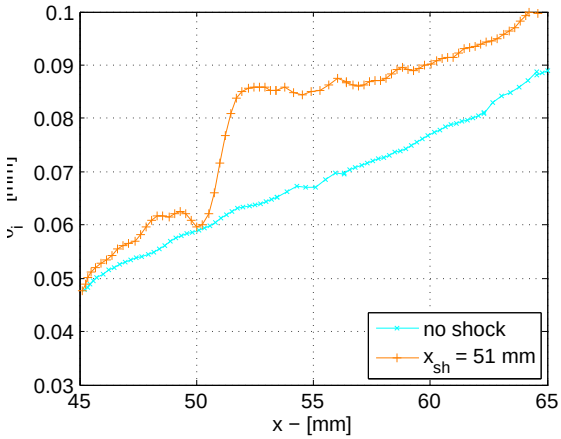

Figure 5.20: Momentum thickness variation with x. Trip = distributed roughness

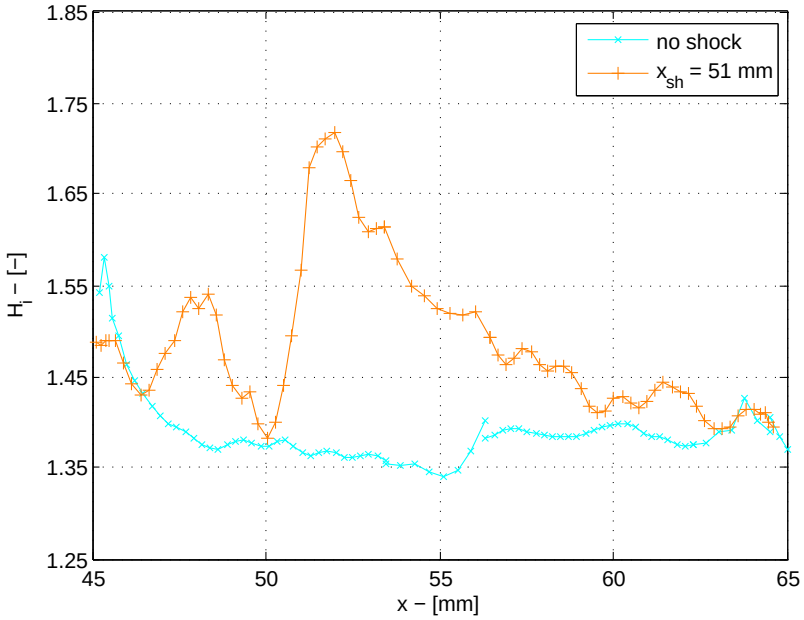

Figure 5.21: Shape factor variation with x. Trip = distributed roughness

In order to make a better comparison between the trips, the resulting incompressible shape factors of all trips are combined in Figure 5.22. It can be seen that the zig zag strip is the most effective: at x = 48 mm, 8 mm downstream of the trip, the shape factor of the zig zag is substantially lower than the shape factor of the other two trips. The rate with which H_i decreases after the interaction for the distributed roughness and zig zag strip are comparable. However, due to the difference in peak value, the zig zag has recovered faster than the distributed roughness case. For the distributed roughness, the incompressible shape factor downstream of the interaction is still gradually decreasing at x = 65 mm, although it seems that the boundary layer is close to its maximum recovery. The incompressible shape factor downstream of the step seems to recover the fastest. While the peak value behind this trip is the highest, the fast recovery of the boundary layer results in a lower H_i at x>55 mm than the H_i behind the distributed roughness. At x = 62 mm, the incompressible shape factor behind the step has become even as low as the incompressible shape factor behind the zig zag strip.
It is also observed, that all three trips lead to $H_i = 1.37 \pm 0.02$ just upstream of the interaction. It is not yet determined if this is a physical feature of the boundary layers, or merely a PIV artefact; further research is recommended.

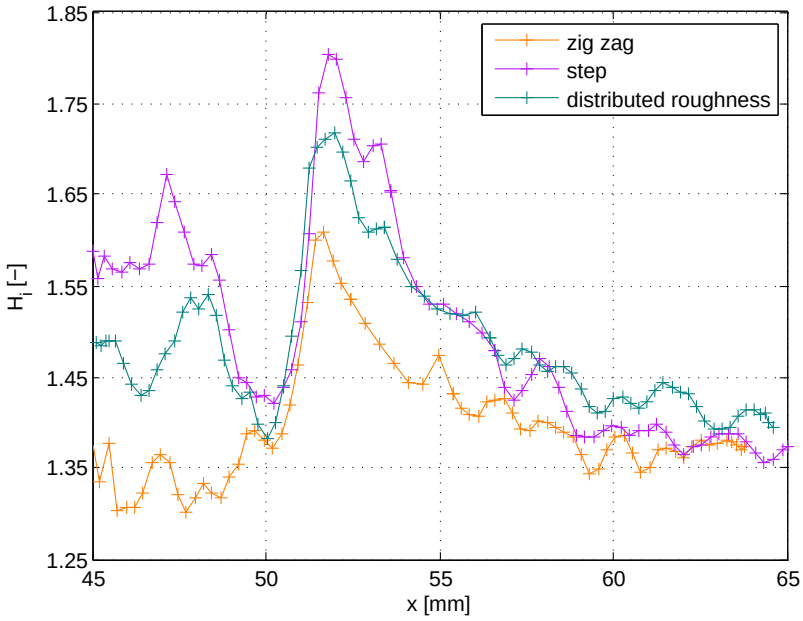

Figure 5.22: Shape factor variation with x, all trips

To compare the recovery lengths of the three trips, a rational fit of the experimental data for 54 mm $< x <$ 63 mm is determined. The R^2 values are 0.81, 0.94 and 0.94 for respectively the zig zag strip, the step and the distributed roughness. The asymptotic values of H_i are in the range 1.28-1.32. The result is presented in Figure 5.23. The dashed line indicates the value of H_i at which the boundary layer is considered recovered, and equals the highest asymptotic value $H_i = 1.32 + 10\% \approx 1.45$.

If the recovery length l_r is defined as the distance between $x_{sh} = 51$ mm and $x(H_i = 1.45)$, it can be observed that the zig zag strip leads to the lowest l_r: $l_r = 3.4$ mm. The difference between the distributed roughness and the step is less pronounced than the difference between the zig zag strip and the other trips. The recovery length of the step ($l_r = 6.2$ mm) is, however, shorter than the recovery length $l_r = 7.6$ mm that results from the distributed roughness. These values are also presented in Table 5.3.

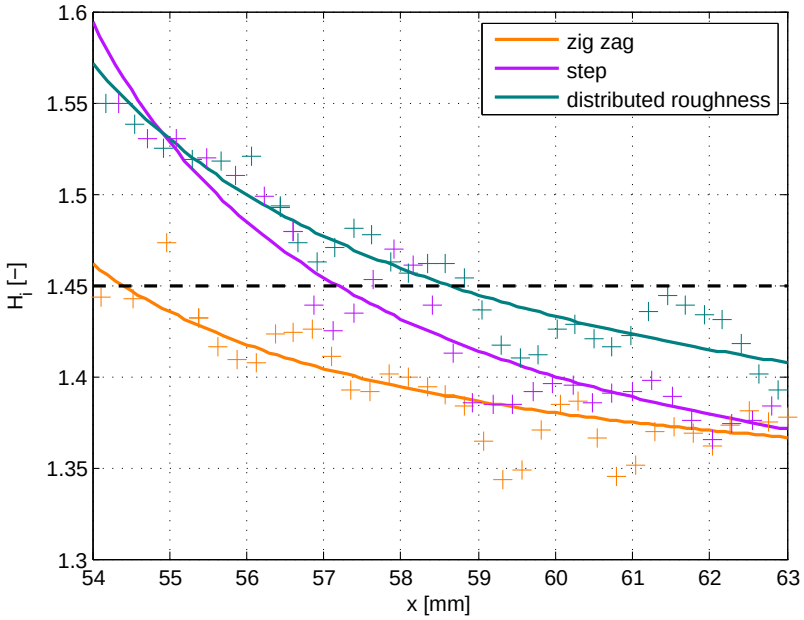

Figure 5.23: Shape factor variation with x, all trips. The solid line represents the fit, the dashed line represents the value of H_i at which the boundary layer is considered recovered and the '+' represents the experimental data.

The velocity profiles downstream of the three trips are compared at three different locations: at x = 48 mm, at x($H_{i,peak}$) and at x = 62 mm. These profiles are presented in Figure 5.24. The markers represent measured values. Below the lowest marker, the data consists out of the fit only. From this figures it again becomes clear that the zig zag strip results in the fullest profile at all locations. For the lowest y-values, i.e. y<0.1 mm, the profiles behind the step and the distributed roughness are nearly identical. However, the step always reaches 90% of its freestream velocity at a lower y-position than the distributed roughness. At x = 62 mm all the boundary layers have recovered such that the differences have become minimal. Especially the difference between the step and the zig zag has become insignificant at this location; the distributed roughness shows a slightly less full profile.

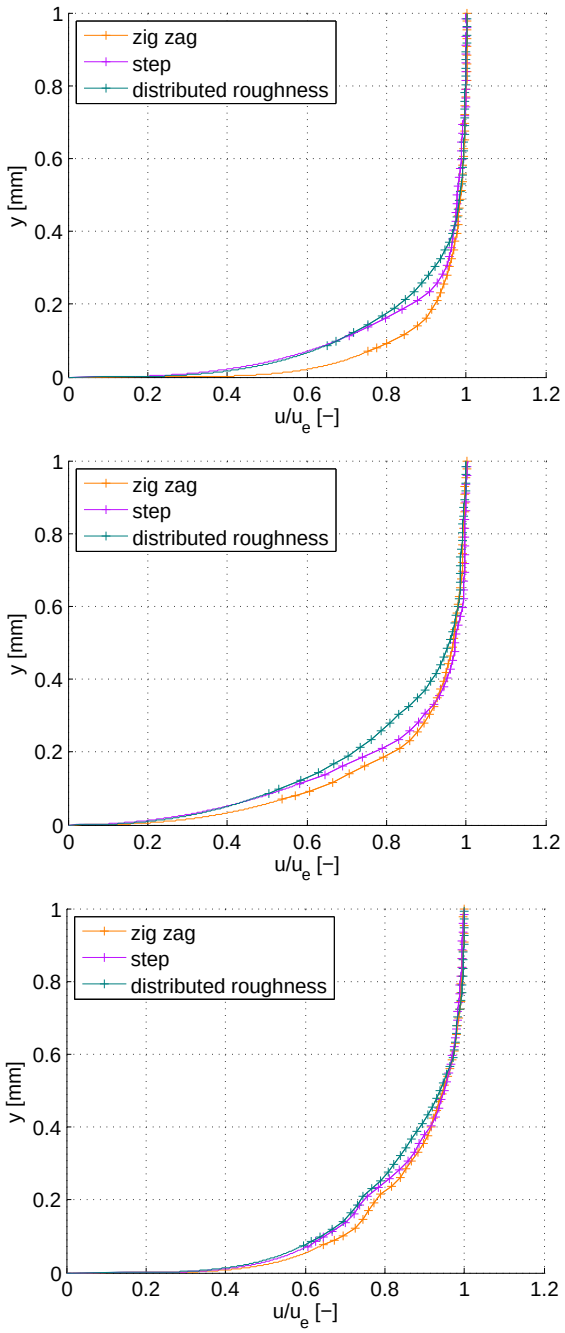

Figure 5.24: Velocity profiles at, from top to bottom, x = 48 mm, x = x(H_{peak}) and x = 62 mm, $x_{sh} \approx 51$ mm

All the determined integral boundary layer parameters at x = 62 mm are summarized in Table 5.3. The values of the incompressible shape factor indicate that all cases have recovered at x = 62 mm. While the peak values of H_i for the trips showed a significant variation, this is no longer the case at x = 62 mm. The case without a trip has recovered to the lowest shape factor, $H_i = 1.31$.
It can be seen that in particular the values behind the zig zag and the step, both with and

without a shock wave, are very similar. The velocity profile behind the zig zag when there is no shock, is slightly fuller than for the case of the step. Both trips show an increase in the displacement thickness and the momentum thickness when there has been a shock. The incompressible shape factor increases as well, but has already recovered to H_i=1.37 at x = 62 mm.
The integral boundary layer parameters downstream of the distributed roughness are higher than downstream of the other trips. Based on the fact that the shape factor is also higher, it is expected that the higher momentum thickness is a result of the friction drag around (and on) the trip.
When comparing the clean case without a shock wave to the cases with trips without a shock wave, it is clear that the clean case is more laminar at x = 62 mm. Not only the shape factor, but also the momentum thickness is much lower. The clean case still benefits from its initially smaller boundary layer thickness, and lower momentum thickness, if there is a shock wave. In this case the momentum thickness will still be significantly lower at x = 62 mm.

The increase in the compressible momentum thickness when comparing the values at x = 38 mm to the values at x = 62 mm for the cases with a trip, no shock, is in the range of 0.036 ± 0.006 mm. The highest increase is observed for the distributed roughness. The increase in this value is much smaller if no trip is placed; in this case the increase is only 0.010 mm. A substantial difference between the compressible momentum thickness of the cases with and without trips, in this case of 0.026 ± 0.006 mm, was to be expected, since the trip will result in a thicker boundary layer and a higher drag.
When considering the case with a shock wave and the trips, the increase in the compressible momentum thickness at x = 62 mm when compared to the values at x = 38 mm is 0.053 ± 0.03 mm. For the clean case, the increase is 0.039 mm. This gives a difference of 0.014 ± 0.03 mm when comparing the cases with the trips to the clean case. This decrease in the difference between the two configurations is assumed to be a result of the separation. The separation will lead to a significant thickening of the boundary layer, while the attached flows behind the trips will be less affected by the shock wave.

Table 5.3: Compressible and incompressible momentum thickness at x = 62 mm

	x_{sh} [mm]	δ_i^* [mm]	θ_i [mm]	H_i [-]	θ [mm]	l_r [mm]
clean case	-	0.101	0.043	2.37	0.035	-
clean case	51	0.094	0.072	1.31	0.064	-
zig zag	-	0.089	0.068	1.31	0.059	-
zig zag	51	0.122	0.089	1.37	0.078	3.4
step	-	0.089	0.066	1.35	0.056	-
step	51	0.120	0.088	1.37	0.076	6.2
distributed roughness	-	0.112	0.081	1.39	0.068	-
distributed roughness	51	0.134	0.094	1.43	0.081	7.6

5.4 Drag

The drag of a flat plate that is parallel to the flow consists out of friction drag only. In this section, an approach that is based on the gradient of the compressible momentum thickness to determine the local skin friction coefficient is presented. Subsequently, the total drag is presented. The determination of the total drag is based on the momentum balance, which was presented in Section 4.6.

To determine the local skin friction coefficient c_f, the Kármán momentum-integral relation is used [48]. This relation reduces, for no pressure gradient, to the following function of the compressible momentum thickness θ:

$$c_f/2 = d\theta/dx \tag{5.1}$$

Since there will be a substantial pressure gradient in the region around the shock wave, this relation is not valid in that region. Since a fuller velocity profile leads to a higher C_f, it can be stated that if the gradient of the momentum thickness is higher, the corresponding trip has led to a fuller velocity profile. The variation in the momentum thickness for the three trips with and without shock wave are presented in Figure 5.25 and Figure 5.26.

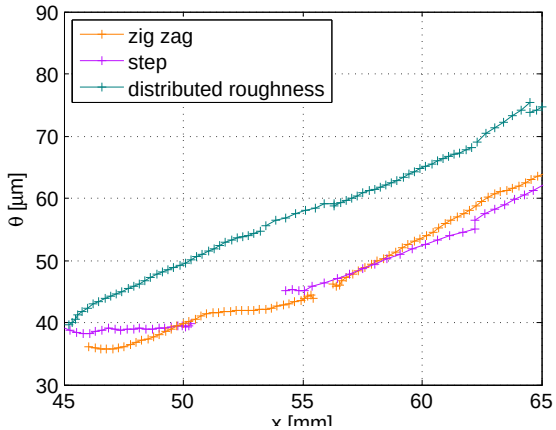

Figure 5.25: Compressible momentum thickness with x for the three trips, no shock

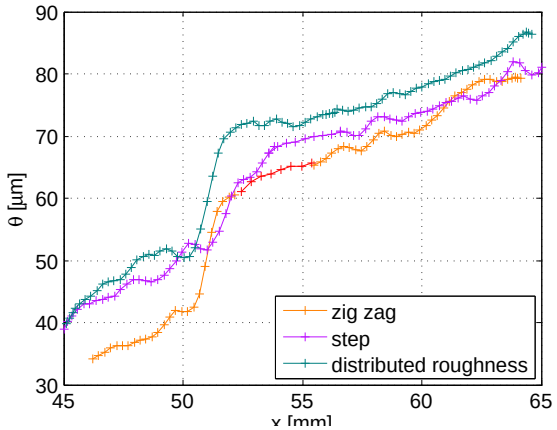

Figure 5.26: Compressible momentum thickness with x for various trips, $x_{sh} \approx 51$ mm

The skin friction coefficient is determined at x = 60 mm, and is based on one run per case. To determine the skin friction coefficient, a linear fit of the data points of the compressible momentum thickness centred around x = 60 mm is used. The results are collected in Table 5.4.

Table 5.4: Skin friction coefficient, x = 60 mm

	C_f [-]	
	no shock	shock
zig zag	0.0044	0.0035
step	0.0026	0.0025
distributed roughness	0.0032	0.0030

As could have also been concluded based on a visual inspection of Figure 5.25 and Figure 5.26, the skin friction behind the zig zag strip is the largest. From this it can be concluded that the zig zag strip will lead to the fullest profile. This is in agreement with the conclusion that was drawn in section 5.3, which was based on the incompressible shape factor. When there is a shock wave, the skin friction coefficient decreases from 0.0044 to 0.0035. This is to be expected, since the shock wave will lead (locally) to a less full profile.
The skin friction coefficient behind the step is significantly lower than the skin friction coefficient behind the zig zag strip. It should however be noted that the last data points of the case without the shock (i.e. for $60 < x < 62$ mm) seem to be lower than the value that would be expected based on the data of the following run (i.e. $x > 62$ mm). If the latter data set is correct, the skin friction coefficient would be higher than the currently determined value. This could also be a reason for the small difference between the cases with and without a shock wave. However, based on Figure 5.25 it seems highly unlikely that the skin friction coefficient can be higher than the skin friction coefficient of the zig zag. The determined skin friction coefficient behind the distributed roughness is comparable to the skin friction behind the step.

The determination of the total drag proved to be more difficult than was anticipated. One of the reasons was the sensitivity of the drag on the calibration procedure. To illustrate this, it is calculated what happens to the drag when the calibration is 1% off, leading to a freestream velocity of 418 m/s in the region downstream of the reflected shock. This would increase the contribution of the momentum flux on the right side of the control volume (Figure 4.18, page 46) from 791 N/m to 804 N/m. The effect of this sensitivity is even more severe since the results of multiple runs are needed to determine the drag, which are calibrated separately.
The detrimental effect of combining the measurements that are calibrated individually on the accuracy with which the drag is determined, can be reduced by using the information obtained from the large FOV PIV images for the calibration. While this would undoubtedly have a positive effect on the accuracy, time constraints prevented the implementation of this calibration method.

However, it is still attempted to find the drag on the basis of the readily available information. For both the pressure terms, as well as the inflow of momentum on the left side of the control volume, the theoretical values are used. The main part in which there is a momentum inflow due to the v-component of the velocity is captured in the measurements that are centred in the flow, while the outflow of momentum on the RHS of the control volume is based on a different run. The results are presented in Table 5.5. While the step and the distributed roughness show the expected behaviour, i.e. a decrease in the drag when there is a shock wave, the zig zag strip does not. The drag of the zig zag case actually increases when there is a shock wave. No reason, except for an erroneous determination of the drag, can be thought of that explains this behaviour. It is therefore concluded that if the drag needs to be determined, the experiment needs to be designed differently.

Table 5.5: Contributions to the drag, split up into the momentum influx over the upper boundary and over the right boundary of the control volume

		integrated flux top [N/m]	integrated flux right [N/m]	total drag [N/m]
inviscid theory	shock	-101	791	0
zig zag	no shock	0	726	27
	$x_{sh} = 51$ mm	101	745	44
step	no shock	0	723	31
	$x_{sh} = 51$ mm	97	765	21
distributed roughness	no shock	0	716	37
	$x_{sh} = 51$ mm	87	737	33

5.5 Interaction length

The interaction length L is defined as the distance between the location where the incident shock wave, if not disturbed by the viscous boundary layer, would impinge on the plate and the location on the wall to which the reflected shock wave can be traced back. Since both are severely affected by the presence of the boundary layer, the locations are determined by an extrapolation of the shock wave position in the freestream. However, as discussed in Section 4.2, the seeding particles will have a substantial slip velocity immediately after the shock since the seeding cannot adapt instantaneously to the new conditions after the shock. This will result in an apparent broadening of the shock in the PIV images. Therefore, the images need to be corrected for the slip effect before the location of the shock is determined. This correction is based on the equation of motion of a small spherical particle in a steady flow, with the density of the particle high compared to that of the fluid (Equation 5.2). The equation of motion can be rewritten such that the actual flow velocity can be relatively easily determined based on the particle velocity, see Equation 5.3 [40]. Note that the particle recovery time has already been calculated in Section 4.2 to be τ =2.12 μs.

$$\frac{d\vec{U_p}}{dt} = \frac{\vec{U_p} - \vec{U_f}}{\tau} \tag{5.2}$$

$$\vec{U_f} = \vec{U_p} + \tau \left[\left(\nabla \vec{U_p} \right) \vec{U_p} \right] \tag{5.3}$$

The corrected velocity field is used to find the shock location. As a decrease in the u-component of the velocity is inherent to a shock wave, the gradient du/dx is used to locate the shock. The resulting shock position in case the distributed roughness is used is presented in Figure 5.27. The shock waves are projected on the corrected velocity field (top image), as well as on the uncorrected velocity field (bottom image). Note that the v-component of the displayed vectors has been multiplied by 5, in order to enhance the visibility of the effect of the shock wave on the flow. The resulting images for the cases where the zig zag strip and the step are used are placed in Appendix B.
When comparing these images in Figure 5.27, it can be concluded that while the corrected velocity field allows for a less ambiguous shock wave location, the noise in the freestream regions has increased. Taking into account the increased noise and the fact that the streamwise gradients are only significant around the shock wave, this correction is only applied to find the interaction length and is not used when calculating the integral boundary layer parameters.

To further illustrate the effect of the slip correction, the velocity profile behind the distributed roughness at $y = 2.53$ mm is investigated. In Figure 5.28 the measured u-component of the velocity is presented, as well as the corrected and theoretical velocity. The theoretical values of the velocity are based on an inviscid interaction and the shock relations; the location of the shock in the theoretical profile corresponds to the location of the shock in Figure 5.27. It

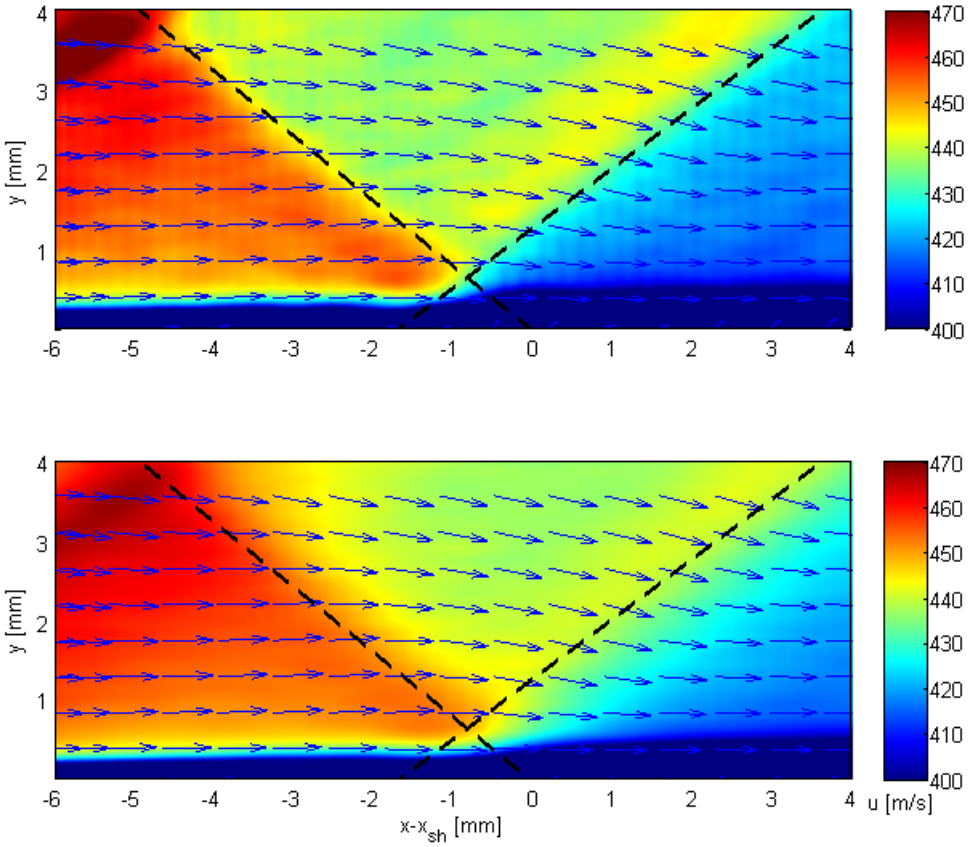

Figure 5.27: Determined shock location positioned on velocity field, trip = distributed roughness. Upper image is corrected for slip velocity, lower is uncorrected data

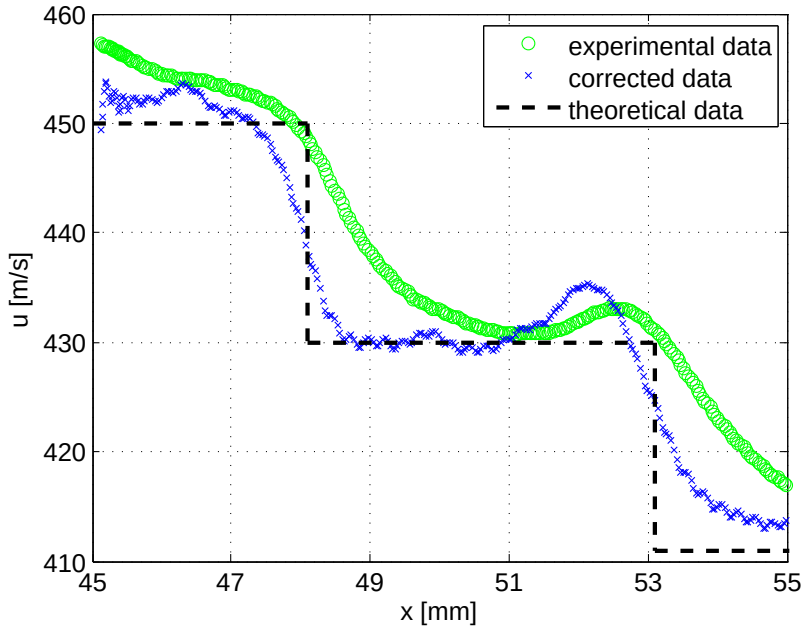

Figure 5.28: A comparison between the uncorrected measurement data, the corrected measurement data and the theoretical velocity

can be observed that the slip correction does indeed facilitate the determination of the shock location, but adds to the noise.

The determined interaction lengths are presented in Table 5.6. It is found that the interaction length of the zig zag strip, the distributed roughness and the step are 1.3, 1.7 and 2.0 mm, respectively. To compare how close to separation the flows behind the different trips are, the scaled interaction length $L/\delta_i^* n$ is determined. A higher value of this ratio, indicated that the flow is further from separation [42]. At $x \approx 47$ mm, the displacement thickness of the zig zag strip, the step and the distributed roughness is expected to be approximately 0.060, 0.080 and 0.075 mm, respectively (values are based on the figures presented in Section 5.3). The resulting non-dimensional values of the interaction length are presented in Table 5.6. It is found that the zig zag strip is the furthest from separation. The step, again, seems to be the closest to separation. However, the small difference in both the interaction lengths and the non-dimensional interaction lengths make it hard to draw a sound conclusion regarding the effectiveness.

Table 5.6: Interaction properties of the different trips

	shock angle [deg]		L [mm]	$L/\delta^*[-]$
	incoming	reflected		
inviscid theory	38.9	38.3	-	-
zig zag	39.3	36.3	1.3	22
step	39.9	36.7	2.0	25
distributed roughness	39.1	37.0	1.7	23

To check the validity of the results, the shock angle is determined. Since a Mach 1.7 flow is tested, and the shock generator has a half-angle of 3°, the shock angle of the incident shock wave should be 38.9°. The angle of the reflected shock for an inviscid interaction would be 38.3°. As can be seen in the table, the angles determined for the incoming shock vary slightly from 39.1 up to 39.9°. The angles of the reflected shock are lower than the theoretical inviscid value: they range from 36.3° up to 37.0°. A difference in this angle can be traced back to the difference between the theoretical inviscid interaction and the actual viscid interaction. In the actual flow there will be a gradual increase of the boundary layer height, which will initially lead to compression waves instead of a shock wave. Taking into account this difference, a deviation of 2° of the theoretical value is not found alarming.

5.6 Additional case: shock impinging at 46 mm

In the previous sections, the boundary layer development and shock interactions resulting from different trips have been described. It was found that when the shock impinges at $x_{sh} = 51$ mm, all three trips are sufficiently effective in eliminating separation. Therefore, it was decided to test a more upstream shock position: $x_{sh} = 46$ mm. For this shock position, only the step and the distributed roughness are tested. From the previous measurements it was found that the boundary layer 6 mm downstream of both these trips did not seem to be fully turbulent; as a consequence there is a greater probability that the trips are not able to ensure that the boundary layer will remain attached.

The resulting flow field behind the distributed roughness is presented in Figure 5.29. For clarity, the v-component of the shown vectors again equals five times the true v-component of the velocity. The velocities in the boundary layer seem rather high and there is no expansion fan visible in the PIV image. The reflected shock is, however, less defined than in the PIV images of the case where $x_{sh} = 51$ mm. This could indicate that the reflected shock has been replaced by a series of compression waves.
The vectors in the boundary layer of the interaction region are shown at a smaller pitch in Figure 5.30. Also in this image a full boundary layer can be seen; it does not seem as if the boundary layer is close to separation.

However, a different conclusion is drawn regarding the effectiveness of the step. The flow field downstream of the step is shown in Figure 5.31. The reflected shock is even less defined than it is behind the distributed roughness. It can also be seen that the v-component of the lowest vectors in the region just downstream of the interaction has has become more negative. This indicates that there is significant narrowing of the boundary layer, which could correspond to reattachment.
In Figure 5.32 the vectors in the interaction region are shown at a smaller pitch. It is clear that this profile is much less full than is the case for the distributed roughness. Based on the magnitude and direction of the vectors, an estimate of the region of separated flow is made. The expected location of the separation bubble is covered by the white patch. The size of the separation bubble is much smaller than the size of the separation bubble for the clean case. The expected length is now 3 mm and the maximum height is 0.1 mm. For the clean case, the length of the bubble is approximately 10 mm, with a maximum height of approximately 0.2 mm (see Figure 5.7).

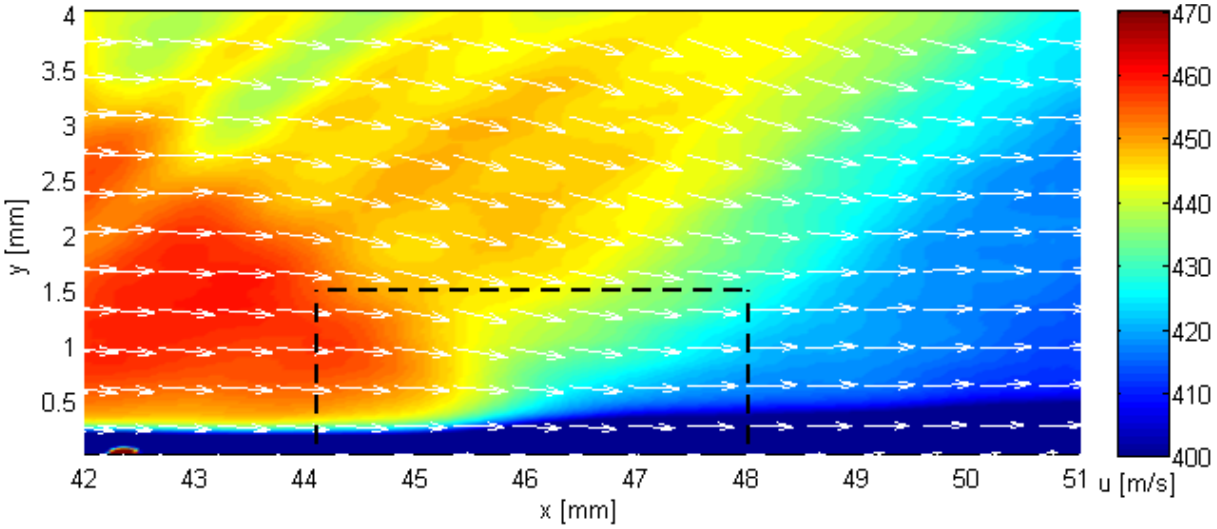

Figure 5.29: Flow field downstream of the distributed roughness, x_{sh} = 46 mm

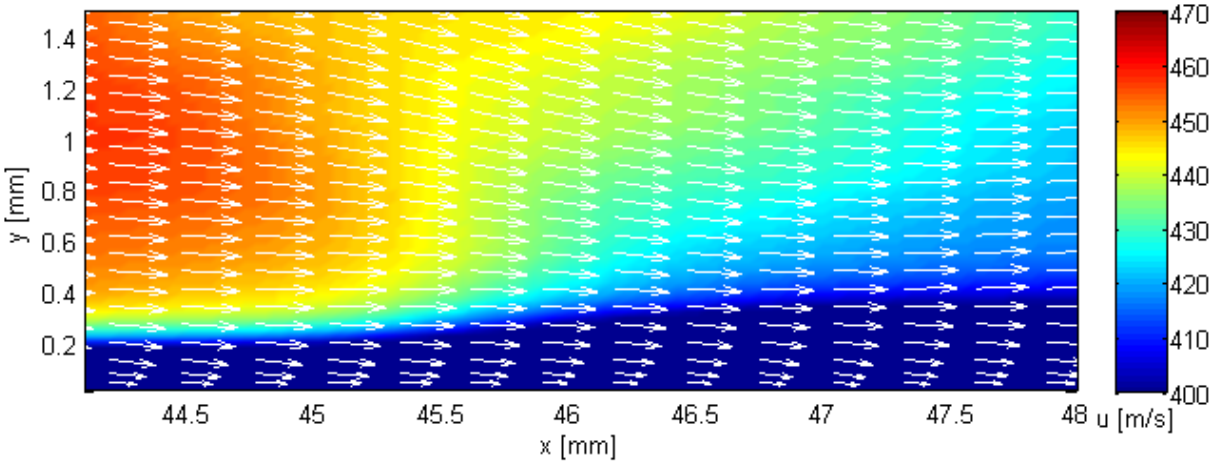

Figure 5.30: Flow field downstream of the distributed roughness zoomed in on the interaction, x_{sh} = 46 mm

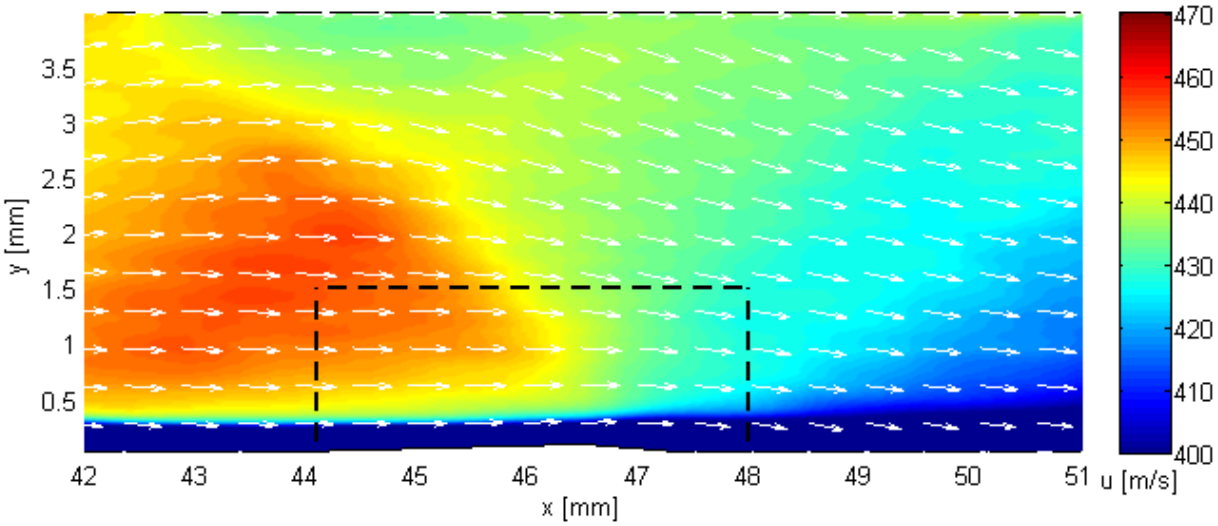

Figure 5.31: Flow field downstream of the step, $x_{sh} = 46$ mm

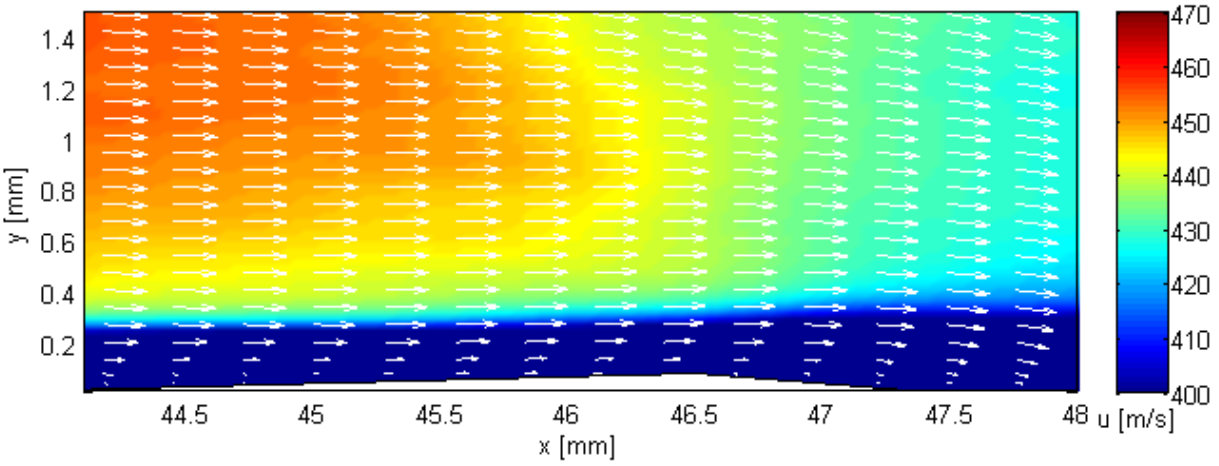

Figure 5.32: Flow field downstream of the step zoomed in on the interaction, $x_{sh} = 46$ mm

Chapter 6

Conclusions and recommendations

The purpose of this research was to determine how the two seemingly incompatible demands of a low friction drag on the one hand and maintaining an attached boundary layer over a SWBLI on the other hand can be combined by using passive flow control devices. The purpose of these devices is to force the transition of the laminar boundary layer upstream of the interaction. The effectiveness of three passive flow control devices (trips) on a SWBLI has been investigated: a 2D step, 3D distributed roughness and a zig zag strip. The accompanying research question was formulated as follows:

Which tripping device is the most effective in enhancing the ability of a boundary layer to withstand an adverse pressure gradient which derives from an incident shock wave in a Mach 1.7 flow?

To answer this question it has first been determined by which parameters the effectiveness of a trip can be described. From these parameters a set of sub-questions was derived. The answers to these sub-questions are discussed in the first section of this chapter, which concludes with the answer to the research question. Subsequently, several recommendations for future research are presented.

Conclusions

Sub-question 1: Which trip can ensure that the boundary layer does not separate?
The main case that has been investigated considers a flow deflection angle of 3°, resulting in a shock angle of 38.9°, and a shock impingement location $x_{sh} = 51$ mm. Measurements with a clean configuration showed that under these conditions the shock interaction induces

separation of a laminar incoming boundary layer. The trips were placed at x = 40 mm. On the basis of Schlieren visualisations, oil flow measurements and PIV measurements, it was ascertained that the boundary layer remained attached for all three tripping devices.

Since all trips were found to be effective in eliminating separation under these conditions, a second case was investigated. The difference with the first case is the upstream shift in the location of the incident shock wave: now $x_{sh} = 46$ mm. This brings the interaction location closer to the location of the trips. For this additional case it was only determined whether there is separation; the integral boundary layer parameters have not been determined.
Only the step and the distributed roughness have been considered for this second case. On the basis of oil flow measurements and PIV measurements, it was concluded that while the distributed roughness can ensure an attached boundary layer, the step cannot. Apparently, the boundary layer downstream of the step needs a longer distance before a sufficiently turbulent state is reached.

Sub-question 2: Which trip is the most effective in forcing transition?
To determine the effectiveness of the trip, the development of the incompressible shape factor H_i downstream of the trips has been investigated. It was found that the zig zag strip led to H_i = 1.4 at x = 45 mm, indicating a turbulent boundary layer. The boundary layer downstream of the distributed roughness had a $H_i = 1.6$ at x = 45 mm, which rapidly decreased to H_i = 1.4 at x = 47 mm. The results of the step indicated that this trip was the least effective: a sharp decrease in H_i was still observed at x = 47 mm, and $H_i = 1.4$ was not reached until $x \approx 50$ mm.

Sub-question 3: Which trip results in a boundary layer that can maintain the fullest profile over the interaction?
To answer this question, the development of H_i in the interaction region was investigated. The peak value of H_i downstream of the zig zag strip was $H_i = 1.60$, downstream of the distributed roughness $H_i = 1.71$, and downstream of the step $H_i = 1.80$. This order was to be expected on the basis of the values of H_i of the different trips a short distance upstream of the interaction. These values indicate that the zig zag strip results in the boundary layer that maintains the fullest profile over the interaction.

Sub-question 4: Which trip results in a boundary layer that can recover the fastest after an interaction?
The answer to this sub-question has been based on the development of H_i downstream of the interaction region. It was found that the rate of decrease of H_i in this region is comparable for the zig zag strip and the distributed roughness. However, since the peak value of H_i is lower when the zig zag strip is used, the recovery of this boundary layer needs the shortest distance: $l_r = 3.4$ mm. For the distributed roughness, a recovery length of $l_r = 7.6$ mm was found.
Surprisingly, it was found that even though the highest peak value in H_i was encountered if the step is used, the H_i for x > 57 mm is smaller downstream of the step than downstream of the distributed roughness. The recovery length of the step was $l_r = 6.2$ mm.
The difference between the recovery lengths of the zig zag strip and the other trips is substantial enough to conclude that the zig zag strip results in the fastest recovery of the boundary

layer. The difference between the recovery lengths of the step and the distributed roughness, however, was not deemed substantial enough to draw the conclusion that the boundary layer downstream of the step recovers faster.

Sub-question 5: Which trip results in the shortest interaction length?
The zig zag strip resulted in the largest decrease in interaction length: L dropped from approximately 10 mm for the clean case to 1.3 mm. The step and the distributed roughness led to an interaction length of 2.0 mm and 1.7 mm, respectively. Also on the basis of the non-dimensional interaction length, which is an indicator of how close to separation a certain flow is, the zig zag would be preferred

Based on the answers to these questions for $x_{sh} = 51$ mm, it is concluded that the zig zag strip is the most effective trip. This trip showed the lowest H_i for both the incoming boundary layer as well as for the interaction, which indicates that it is the furthest from separation.
For an incident shock at $x_{sh} = 51$ mm, both the step and distributed roughness show advantages as well as disadvantages. However, since for $x_{sh} = 46$ mm the step does not prevent separation while the distributed roughness does, it is decided that the distributed roughness is more effective than the step.

Recommendations

Over the course of this research project, there were several moments at which it was realized that improvements could be made in order to increase the accuracy of the results. It is recommended to improve the following when further experiments on this subject are performed:

- **The seeding**. As was discussed in Section 4.1, the particle response time of the TiO_2 that was used for this research is 2.12 μs. If this response time is decreased, it will be possible to better resolve the flow around the shock wave. A lower response time would also facilitate the measurements in the laminar boundary layer, since the lower response time can result in a higher seeding density in this region.
  A possibility could be to use dehydrated TiO_2 with a grain size of 50 nm instead of 30 mm, in combination with a cyclone seeder with a 1 μm filter [35]. According to Ragni et al., this would lead to a relaxation time of 0.56 μs, while for the currently used seeding they had found a relaxation time of 2.20μs. A major disadvantage, however, would be the decrease in the amount of seeding particles in the flow.

- **The FOV**. At the moment, the FOV is limited to 12.5 mm in the streamwise direction if the spatial resolution is set at 130 pix/mm. To increase the FOV while maintaining the same resolution, different cameras (with a minimum separation time comparable to, or lower than, the minimum separation time of the currently used cameras) are required. The first benefit of a larger FOV is the decrease in the required wind tunnel time. The second is that the results of less runs will have to be 'stitched'. This is beneficial, since the stitching can possibly introduce additional inaccuracies.

- **The pressure**. For this research, no pressure measurements were conducted. As a result, the theoretical pressure was used in the momentum balance (see Equation 4.11). However, the pressure downstream of the shock system actually depends on the properties of the reflected shock, which will probably not be identical in all cases. The lack of information on the true pressure made it again harder (if not impossible) to accurately determine the drag. Information on the true pressure downstream of the shock system would also be interesting if the effect of the SWBLI on the engine performance is studied more extensively.
  It would be possible to determine the pressure on the basis of the velocity field that is obtained with the PIV measurements [45]. The lack of valid PIV data in close proximity of the wall would, however, impede the pressure determination. Pressure measurements could be used to validate the pressures found from the PIV measurements.

- **The trips**. Since it was found that the boundary layer downstream of all trips remained attached over the interaction region, it is interesting to see if the trips are still effective at a smaller height and/or placed a shorter distance from the interaction. It is expected that especially the distributed roughness and zig zag strip will still be effective at a smaller roughness height and/or when placed closer to the interaction.
  A second recommendation regarding the trips applies to the distributed roughness only. The distributed roughness was randomly applied, and it is possible that some particles were eroded off during a wind tunnel run. To ensure that the distribution of the particles over time is constant and to facilitate the comparison with a possible CFD simulation of this trip, a 3D printed roughness patch could be used. The additional advantage of a 3D printed roughness patch would the absence of a reaction between the paint and the glue/particles. In this research project, this reaction led to a lower roughness height than was initially intended.

Bibliography

[1] R.J. Adrian and J. Westerweel. *Particle image velocimetry.* ISBN 978-0-521-44008-0, Cambridge University Press, New York, 2011.

[2] D. Arnal and J. Délery. Laminar-Turbulent Transition and Shock Wave/Boundary Layer Interaction. In *RTO AVT Lecture Series on Critical Technologies for Hypersonic Vehicle Development*, Rhode-St-Genese, Belgium, 2004. Von Karman Institute, The Von Karman Institute.

[3] T. Astarita. Analysis of weighting windows for image deformation methods in PIV. *Experiments in Fluids*, 43:859–872, September 2007.

[4] J.K. Babinsky. *Shock Wave Boundary Layer Interaction.* ISBN 978-0-521-84852-7, Cambridge University Press, 2011.

[5] S.J. Beresh, N.T. Clemens, and D.S. Dolling. Relationship Between Upstream Turbulent Boundary-Layer Velocity Fluctuations and Separation Shock Unsteadiness. *AIAA Journal*, 40(12):2412–2422, December 2002.

[6] A.L. Braslow. Review of the effect of distributed surface roughness on boundary-layer transition. Technical report, Report 254, NATO, Virginia, 1960.

[7] A.L. Braslow and E.C. Knox. Simplified method for determination of critical height of distributed roughness particles for boundary-layer transition at Mach numbers from 0 to 5. Technical report, Technical note 4363, NACA, Washington, 1958.

[8] P.F. Brinich. Boundary-Layer Transition at Mach 3.12 With and Without Single Roughness Elements. Technical report, Technical note 3267, NACA, Cleveland, USA, 1954.

[9] D.R. Chapman, D.M. Kuehn, and H.K. Larson. Investigation of separated flows in supersonic and subsonic streams with emphasis on the effect of transition. Technical report, Report 1356, NACA, 1958.

[10] J Délery and R Bur. The physics of shock wave/boundary layer interaction control: last lessons learned. *European Congres on Computational Methods in Applied Sciences and Engineering*, Barcelona, 2000.

[11] J. Delery and J.G. Marvin. Shock-Wave Boundary Layer Interactions. Technical report, Report 280, AGARD, 1986.

[12] P. Doerffer, C. Hirsch, J.P. Dussauge, H. Babinsky, and G.N. Barakos. *unsteady effects of shock wave induced separation.* ISBN 978-3-642-03003-1, Springer, 2010.

[13] D.S. Dolling. Fifty Years of Shock-Wave/Boundary-Layer Interaction Research: What Next? *AIAA Journal*, 39(8):1517–1531, August 2001.

[14] H.L. Dryden. Review of Published Data on the Effect of Roughness on Transition from Laminar to Turbulent Flow. *Journal of the Aeronautical Sciences*, 20(7):477–482, July 1953.

[15] J.P. Dussauge, P. Dupont, and J.F. Debiève. Unsteadiness in shock wave boundary layer interactions with separation. *Aerospace Science and Technology*, 10:85–91, March 2006.

[16] G. E. Elsinga, B. W. Oudheusden, and F. Scarano. Evaluation of aero-optical distortion effects in PIV. *Experiments in Fluids*, 39:246–256, July 2005.

[17] G.E. Elsinga and J. Westerweel. Tomographic-PIV measurement of the flow around a zigzag boundary layer trip. *Experiments in Fluids*, 52(4):865–876, 2012.

[18] FP7. Transiton location effect on shock wave boundary layer interaction. *Project proposal*, 2010.

[19] G.E. Gadd. Interactions between wholly laminar or wholly turbulent boundary layers and shock waves strong enough to cause separation. *Journal of the Aeronautical Sciences*, 20(11):729–739, 1953.

[20] J.C. Gibbings. On boundary-layer transition wires. Technical report, Current paper No. 462, Aeronautical Research Council, 1958.

[21] R.H.M. Giepman, K. Lynch, F.F.J. Schrijer, and B.W. Van Oudheusden. Investigation of a transitional oblique shock wave reflection using PIV. *17th International symposium on applications of laser techniques to fluid mechanics*, Lisbon, 2014.

[22] R.H.M. Giepman, F.F.J. Schrijer, and B.W. Van Oudheusden. 18 month Work Progress report. Technical report, Technical University of Delft, Delft, 2013.

[23] R.H.M. Giepman, F.F.J. Schrijer, and B.W. Van Oudheusden. 24 month Work Progress Report. Technical report, Technical University of Delft, Delft, 2014.

[24] R.H.M. Giepman, F.F.J. Schrijer, and B.W. Van Oudheusden. Oblique shock reflection at Mach 1.7 - 30 Month update. *6th TFAST meeting*, Liverpool, 2014.

[25] J.E. Green. Interactions between shock waves and turbulent boundary layers. *Progress in Aerospace Sciences*, 11:235–340, January 1970.

[26] R.J. Hakkinen, I. Greber, L. Trilling, and S.S. Abarbanel. The interaction of an oblique shock wave with a laminar boundary layer. Technical report, Memorandum 2-18-59W, NASA, Washington, USA, 1959.

[27] Y.X. Hou, N.T. Clemens, and D.S. Dolling. Wide-Field PIV Study of Shock-Induced Turbulent Boundary Layer Separation. *41st Aerospace Sciences Meeting and Exhibit*, Reno, 2003.

[28] R.A. Humble. *Unsteady Flow Organization of a Shock Wave/Boundary Layer Interaction*. Phd dissertation, TU Delft, 2008.

[29] P.S. Klebanoff and K.D. Tidstrom. Mechanism by Which a Two-Dimensional Roughness Element Induces Boundary-Layer Transition. *Physics of Fluids*, 15(7):1173–1188, 1972.

[30] L. Lees and B.L. Reeves. Supersonic Separated and Reattaching Laminar Flows: I. General Theory and Application to Adiabatic Boundary-Layer/Shock-Wave Interactions. *AIAA Journal*, 2(11):1907–1920, 1964.

[31] A. Melling. Tracer particles and seeding for particle image velocimetry. *Measurement Science and Technology*, 8:1406–1416, 1997.

[32] P. Meunier and T. Leweke. Analysis and treatment of errors due to high velocity gradients in particle image velocimetry. *Experiments in Fluids*, 35:408–421, November 2003.

[33] B. W. Oudheusden, A. J. P. Jöbsis, F. Scarano, and L. J. Souverein. Investigation of the unsteadiness of a shock-reflection interaction with time-resolved particle image velocimetry. *Shock Waves*, 21:397–409, February 2011.

[34] S.B. Pope. *Turbulent flows*. ISBN 978-0-521-59886-6, Cambridge University Press, 2011.

[35] D. Ragni, F. Schrijer, B. W. van Oudheusden, and F. Scarano. Particle tracer response across shocks measured by PIV. *Experiments in Fluids*, 50:53–64, May 2010.

[36] E. Reshotko and A. Tumin. Role of Transient Growth in Roughness-Induced Transition. *AIAA Journal*, 42(4):766–770, April 2004.

[37] R. Narasimha S. Dhawan. Some properties of boundary layer flow during the transition from laminar to turbulent motion. *Journal of Fluid Mechanics*, 3(4):418–436, 1958.

[38] F. Scarano. Iterative image deformation methods in PIV. *Measurement Science and Technology*, 13, 2002.

[39] H. Schlichting and J. Kestin. *Boundary-layer theory*. ISBN 0-07-055334-3, Mc Graw HIll, seventh edition, 1979.

[40] F F J Schrijer and F Scarano. Particle slip compensation in steady compressible flows. *7th International symposium on Particle Image Velocimetry*, Rome, 2007.

[41] E. Schulein. Effects of Laminar-Turbulent Transition on the Shock-Wave / Boundary-Layer Interaction. In *44th AIAA Fluid dynamics conference*, volume 16-20 June, Atlanta, 2014.

[42] L.J. Souverein, P.G. Bakker, and P. Dupont. A scaling analysis for turbulent shock-wave/boundary-layer interactions. *Journal of Fluid Mechanics*, 714:505–535, January 2013.

[43] L.J. Souverein, P. Dupont, J.F. Debiève, B.W. Van Oudheusden, and F. Scarano. Effect of Interaction Strength on Unsteadiness in Shock-Wave-Induced Separations. *AIAA Journal*, 48(7):1480–1493, July 2010.

[44] W.D. Urban and M.G. Mungal. Planar velocity measurements in compressible mixing layers. *Journal of Fluid Mechanics*, 431:189–222, 2001.

[45] B.W. van Oudheusden. Principles and application of velocimetry-based planar pressure imaging in compressible flows with shocks. *Experiments in Fluids*, 45:657–674, August 2008.

[46] R.P.J.O.M. van Rooij and W.A. Timmer. Roughness Sensitivity Considerations for Thick Rotor Blade Airfoils. *Journal of Solar Energy Engineering*, 125:468–478, 2003.

[47] S.T. Wereley and C.D. Meinhart. Micron-resolution particle image velocimetry. *Microscale Diagnostic Techniques*, 2005.

[48] F.M. White. *Viscous fluid flow*. ISBN 007-124493-X, Mc Graw Hill, 3rd edition, 2006.

Appendix A

Experimental set-up: FOV and test matrix

As was discussed in Chapter 4, multiple runs are needed in order to map the flow from $x \approx 45$ mm up to $x \approx 65$ mm. The results of these runs are then stitched together. In order to allow for this stitching, an overlap of approximately 4 mm between subsequent FOVs is required. A graphical overview of the FOVs relative to the set-up is presented in Figure A.1. The yellow square represents the trip (not on scale), while the grey lines are the incoming and reflective shock waves. The solid red line represents a small FOV of camera 1 that is centred on the interaction. The dashed red lines represent the FOV previous to and following the aforementioned FOV. The blue line shows the large FOV, that was used for the overview measurements. The FOV of camera 2, which is always positioned such that its FOV covers the region just upstream of the interaction, is represented by the green lines.

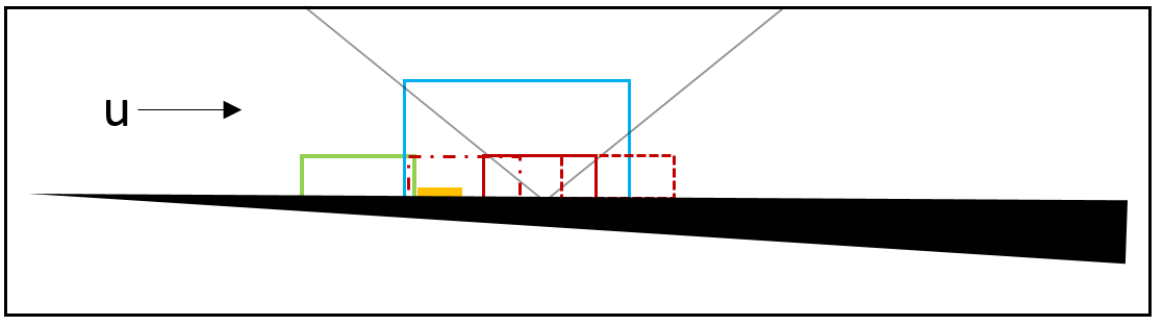

Figure A.1: Overview of the FOVs

The experimental test matrix is presented in Table A.1. In this table, the following abbreviations are used: *zz* (zig zag strip), *dr* (distributed roughness), *# im.* (number of images) and *res.* (spatial resolution). The angle as presented in this table is the angle of the camera in the horizontal plane; *u* and *d* indicate whether the camera is directed upstream or downstream, respectively.

Table A.1: Experimental test matrix

				FOV [mm]		res. [pix/mm]		angle [deg]		
run	trip	x_{sh}	# im.	cam 1	cam 2	cam 1	cam 2	cam 1	cam 2	Δt [ns]
1	zz	-	200	55.7-68.2	30.3-42.6	130	133	2.5d	4.0d	430
2	zz	-	200	67.1-79.6	30.3-42.6	130	133	2.5d	4.0d	430
3	zz	-	400	43.5-56.1	30.7-43.0	130	132	2.5d	4.0d	430
4	zz	51	500	43.4-56.0	29.6-41.8	129	133	4.0d	4.0d	430
5	zz	51	300	52.2-64.3	29.6-41.8	130	133	4.0d	4.0d	430
6	zz	51	150	35.0-60.1	-	62	-	1.0d	-	800
7	step	-	200	53.2-66.4	29.8-42.7	123	129	1.0u	4.0d	430
8	step	-	200	61.2-74.4	29.8-42.8	123	129	1.0u	4.0d	430
9	step	-	300	37.5-51	29.8-41.9	121	129	1.0u	4.0d	430
10	step	51	250	44.2-57.5	29.8-42.9	122	129	3.0u	4.0d	430
11	step	51	300	52.9-65.9	29.8-42.9	124	129	3.0u	4.0d	430
12	step	51	200	34.6-59.8	-	64	-	3.0u	-	800
13	step	46	300	39.7-51.9	29.3-41.9	133	129	6.0d	4.0d	430
14	dr	-	300	44.7-57.0	30.0-42.5	133	130	2.0u	4.0d	430
15	dr	-	200	52.9-64.9	30.0-42.5	135	130	2.0u	4.0d	430
16	dr	-	200	61.8-74.1	30.0-42.5	133	130	2.0u	4.0d	430
17	dr	51	500	44.6-56.8	30.0-42.5	132	130	2.5u	4.0d	430
18	dr	51	450	53.0-65.1	30.0-42.5	134	130	2.5u	4.0d	430
19	dr	51	200	34.3-60.2	-	63	-	2.0d	-	800
20	dr	46	500	41.0-53.6	30.0-42.5	129	130	3.0u	4.d	430

Appendix B

Shock location

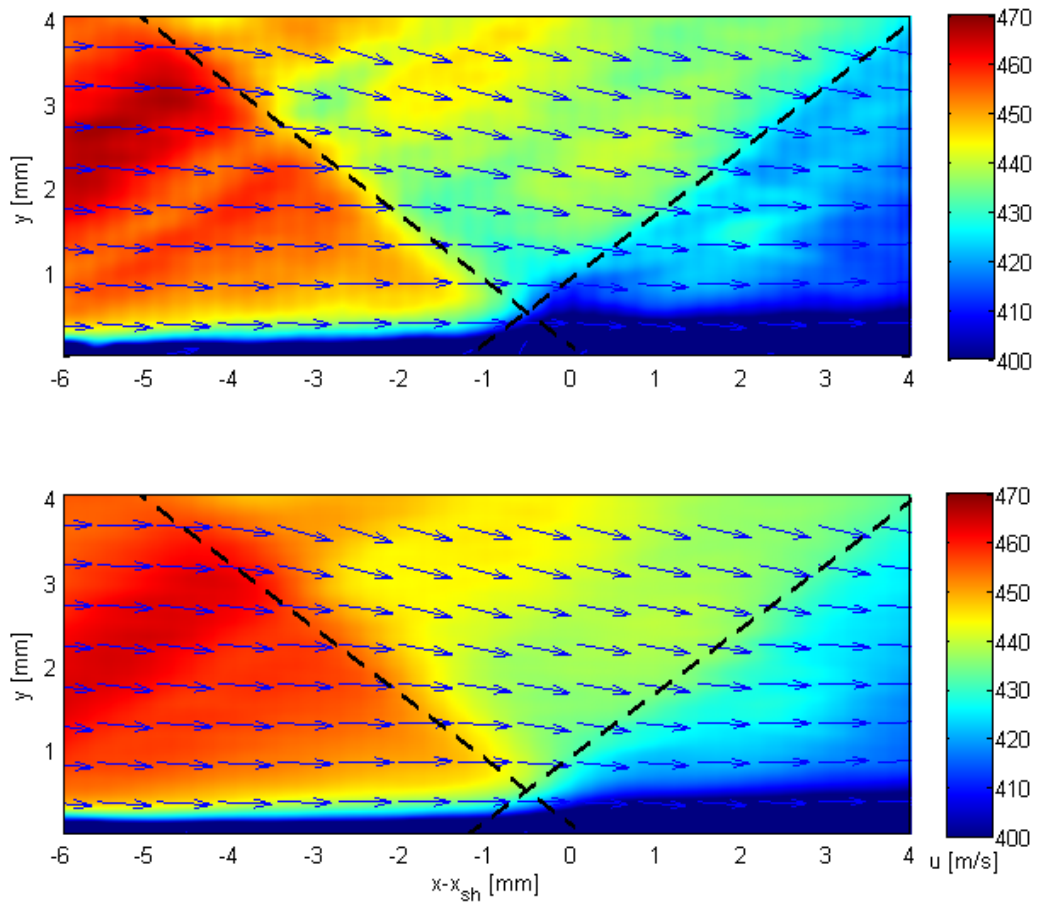

Figure B.1: Determined shock location positioned on velocity field, trip = zig zag. Upper image is corrected for slip velocity, lower is uncorrected data

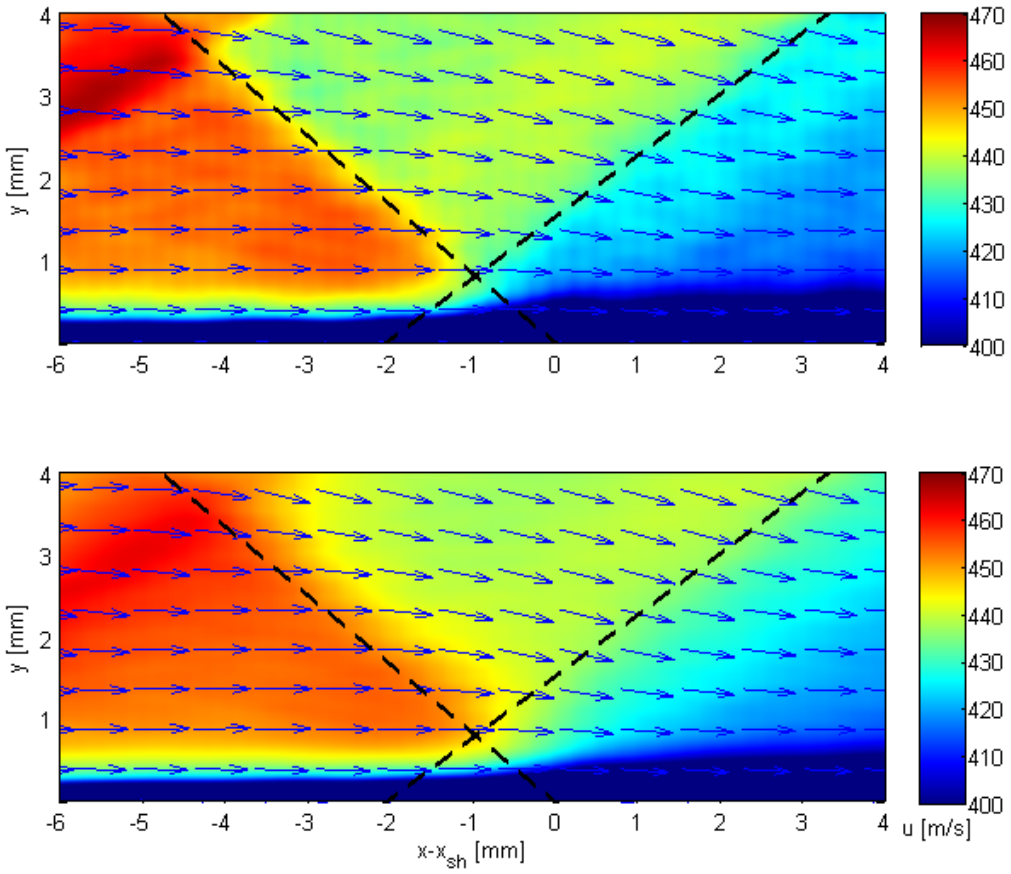

Figure B.2: Determined shock location positioned on velocity field, trip = step. Upper image is corrected for slip velocity, lower is uncorrected data